

**Near Infrared Spectroscopy: Novel Signal Processing
Methods and Applications**

by

Behnam Molavi

B.Sc. Electrical Engineering , Iran University of Science and Technology, 2004

M.Sc. Electrical Engineering , Iran University of Science and Technology, 2007

A THESIS SUBMITTED IN PARTIAL FULFILLMENT
OF THE REQUIREMENTS FOR THE DEGREE OF

Doctor of Philosophy

in

THE FACULTY OF GRADUATE AND POSTDOCTORAL
STUDIES

(Electrical and Computer Engineering)

The University Of British Columbia
(Vancouver)

October 2013

© Behnam Molavi, 2013

Abstract

Oxygen is a critical component in living organisms and its concentration in tissue is an important parameter indicative of tissue metabolism, level of activity and health condition. As a result, measuring oxygen concentration in the tissue is essential in many clinical and research applications. Near Infrared Spectroscopy (NIRS) is a non invasive method of measuring tissue oxygenation using diffusion of light in the tissue. NIRS as a safe, non invasive and low cost monitoring technology has been used in a wide range of applications including monitoring muscle and brain oxygenation, brain computer interface and rehabilitation. The motivation for this thesis has been to develop new signal processing methods and to investigate potential new applications for NIRS.

One major characteristic of NIRS is its sensitivity to movement of the target tissue during the measurement. The effects of movements, known as motion artifacts, have limited clinical applications of NIRS in ambulant patients as well as experimental applications of NIRS monitoring in areas such as exercise science and sports medicine. In this thesis, we present a new method of reducing the effect of motion artifacts on NIRS signal using Discrete Wavelet Transform (DWT).

One of the areas of application which can significantly benefit from reduction of motion artifacts is NIRS-based wearable sensors. In particular, a potential and unexplored application of NIRS is providing a monitoring method for people with bladder control problems, which occurs in a variety of conditions including spinal cord injury and stroke. We investigate the application of NIRS for detection of bladder filling to capacity using a wearable wireless monitoring sensor which can be used to warn the subject once the bladder content reaches a predefined percentage of the full capacity.

NIRS can be used as a functional neuroimaging method to identify brain activations during practice of a motor/cognitive task. One important question in this field is how the activated brain areas are interconnected. We thus investigate the use of phase information in NIRS channels to identify cortical connections and in particular, show the applicability of this approach in identifying language network in human infants.

Preface

Some of the methods and results presented in this thesis have been published or have been submitted for consideration for publication as journal or conference proceedings articles. The list of the publications can be found below.

The material in Chapter 3 was published with preliminary results and at different stages of development using different data types in *Canadian Conference on Electrical and Computer Engineering* in 2010 [1], the Proceedings of the *International IEEE EMBS Conference* in 2010 [2] and *proceedings of SPIE* in 2011 [3]. A more complete version was published in the *IOP Journal of Physiological Measurement* [4]. This article was featured in the "Highlights of 2012" of the *Journal of Physiological Measurement*. The material in Chapter 4 was accepted for publication in the *IEEE Transactions on Biomedical Circuits and Systems* and is also under review by University of British Columbia University-Industry Liaison Office (UILO) for potential intellectual property (IP) protection and licensing. A preliminary version of the method and results presented in Chapter 5 was published in the Proceedings of the *International IEEE EMBS Conferences* in 2011 [5] and 2012 [6]. A modified and more detailed version of this work was submitted and is currently under review for consideration for publication.

The research in this thesis was conducted with approval of the Research Ethics Board (CREB) of the University of British Columbia (approval number H02-80575). The publications resulting from this thesis are as follows:

Journal Articles

- B. Molavi and G. A. Dumont. Wavelet-based motion artifact removal for functional near-infrared spectroscopy. *Physiological measurement*, 33(2):

259-270, 2012. ([4])

- B. Molavi, B. Shadgan, A. Macnab, G. A. Dumont. Non-invasive optical monitoring of bladder filling to capacity using a wireless NIRS device. *IEEE Transactions on Biomedical Circuits and Systems*, 2013, In press.
- B. Molavi, L. May, J. Gervain, J. F. Werker, G. A. Dumont. Analyzing resting state functional connectivity in the language system using near infrared spectroscopy. Submitted, 2013

Refereed Conference Papers

- B. Molavi, J. Gervain, G. A. Dumont, H. A. Noubari. Functional connectivity analysis of cortical networks in Functional Near Infrared Spectroscopy using phase synchronization. *34th Annual International Conference of the IEEE Engineering in Medicine and Biology Society (EMBS)*, pp. 5182–5185, 2012. ([6])
- B. Molavi, J. Gervain, and G. A. Dumont. Estimating cortical connectivity in functional near infrared spectroscopy using multivariate autoregressive modeling. *33rd Annual International Conference of the IEEE Engineering in Medicine and Biology Society (EMBS)*, pp. 2334–2337, 2011. ([5])
- B. Molavi, G. A. Dumont, B. Shadgan, and A. J. Macnab. Attenuation of Motion Artifact in Near Infrared Spectroscopy Signals Using a Wavelet Based Method. *Proceedings of SPIE 7890*, 2011. ([3])
- B. Molavi and G. A. Dumont. Wavelet based motion artifact removal for Functional Near Infrared Spectroscopy. *32nd Annual International Conference of the IEEE Engineering in Medicine and Biology Society (EMBS)*, pp. 5-8, 2010. ([2])
- B. Molavi, G. A. Dumont, and B. Shadgan, "Motion artifact removal from muscle NIR Spectroscopy measurements," in *IEEE Canadian Conference on Electrical and Computer Engineering*, pp. 1-4, 2010. ([1])

Table of Contents

| | |
|--|-------------|
| Abstract | ii |
| Preface | iv |
| Table of Contents | vi |
| List of Tables | x |
| List of Figures | xi |
| List of Abbreviations | xiii |
| Acknowledgments | xvi |
| 1 Background | 1 |
| 1.1 Introduction to Near Infrared Spectroscopy | 1 |
| 1.2 Theory of NIRS | 4 |
| 1.2.1 Modified Beer-Lambert Law | 4 |
| 1.2.2 Photon Diffusion in Tissue | 6 |
| 1.3 Applications of NIRS | 7 |
| 1.4 NIRS Instrumentation | 9 |
| 1.5 Safety Considerations | 11 |
| 1.6 Limitations of NIRS | 12 |
| 1.6.1 Penetration Depth and Spatial Resolution | 12 |
| 1.6.2 Light Coupling | 12 |
| 1.6.3 Interferences | 13 |

| | | |
|----------|---|-----------|
| 1.7 | Motivation for this Thesis | 15 |
| 1.8 | Thesis Contributions | 18 |
| 1.9 | Thesis Outline | 19 |
| 2 | Literature Review | 20 |
| 2.1 | Interference Reduction in NIRS | 20 |
| 2.2 | NIRS in Urology | 23 |
| 2.3 | Functional Brain Connectivity Using functional Near Infrared Spectroscopy (fNIRS) | 25 |
| 2.4 | NIRS for Monitoring TMS | 27 |
| 2.5 | Summary and Conclusion | 29 |
| 3 | Motion Artifact Removal | 32 |
| 3.1 | Artifact Removal Using Discrete Wavelet Transform | 33 |
| 3.2 | Simulation | 36 |
| 3.2.1 | Performance Evaluation | 38 |
| 3.2.2 | Results | 39 |
| 3.3 | Experiment | 40 |
| 3.3.1 | Performance Evaluation | 42 |
| 3.3.2 | Results | 43 |
| 3.4 | Discussion and Conclusion | 46 |
| 4 | Bladder Filling Monitoring with NIRS | 52 |
| 4.1 | Introduction | 52 |
| 4.2 | Detection of Bladder Filling to Capacity Using NIRS | 53 |
| 4.2.1 | Electronics | 55 |
| 4.2.2 | Firmware | 58 |
| 4.2.3 | PC Interface | 60 |
| 4.3 | Performance Evaluation | 61 |
| 4.4 | In Vitro Evaluation | 62 |
| 4.4.1 | In Vitro Setup | 62 |
| 4.4.2 | Results | 63 |
| 4.5 | In Vivo Evaluation | 64 |
| 4.5.1 | Materials and Method | 64 |

| | | |
|----------|--|------------|
| 4.5.2 | Results | 64 |
| 4.6 | Discussion | 68 |
| 4.7 | Conclusion | 71 |
| 5 | Cortical Connectivity Analysis | 72 |
| 5.1 | Functional Connectivity Using Multivariate Autoregressive Mod- eling | 73 |
| 5.1.1 | Materials and Method | 73 |
| 5.1.2 | Results | 78 |
| 5.2 | Analyzing Resting State Functional Connectivity in The Human Language System Using Near Infrared Spectroscopy | 80 |
| 5.2.1 | Material and Methods | 82 |
| 5.2.2 | Results | 87 |
| 5.3 | Discussion and Conclusion | 91 |
| 6 | Custom fNIRS System Design | 95 |
| 6.1 | Background and Motivation | 95 |
| 6.2 | Instrument Design | 96 |
| 6.2.1 | Light Sources | 97 |
| 6.2.2 | Source Modulation | 97 |
| 6.2.3 | Light Detection | 98 |
| 6.2.4 | Digital Lock-in Amplification | 98 |
| 6.2.5 | User Interface | 101 |
| 6.3 | Performance Evaluation | 101 |
| 6.4 | Validation | 102 |
| 6.4.1 | Methods | 102 |
| 6.4.2 | Results | 103 |
| 6.5 | Discussion and Conclusion | 106 |
| 7 | Conclusion and Future Work | 108 |
| 7.1 | Motion Artifact Removal from fNIRS | 108 |
| 7.2 | Wireless NIRS for Monitoring Bladder Contents | 110 |
| 7.3 | fNIRS Connectivity | 113 |
| 7.4 | Custom-made fNIRS Device for TMS Monitoring | 115 |

Bibliography 117

List of Tables

| | | |
|-----------|--|----|
| Table 3.1 | Normalized Mean Squared Error between processed signal and original artifact-free signal | 40 |
| Table 3.2 | Median of Normalized Mean Squared Error (NMSE) and Attenuation in artifacts energy (in dB) for proposed method . . . | 45 |
| Table 4.1 | System level parameters of the sensor | 67 |
| Table 5.1 | Pairwise comparison between selected ROIs inside and outside language network (Tukey's test). | 89 |

List of Figures

| | | |
|-------------|---|----|
| Figure 1.1 | Absorption spectra for human tissue | 3 |
| Figure 1.2 | Typical fNIRS data power spectrum | 14 |
| Figure 3.1 | Simulated comparison of artifact removal methods | 37 |
| Figure 3.2 | Comparison of power spectra after artifact removal | 38 |
| Figure 3.3 | Coherence between original and processed signal | 39 |
| Figure 3.4 | Experiment setup | 41 |
| Figure 3.5 | Optodes placement | 42 |
| Figure 3.6 | Artifact removal example | 43 |
| Figure 3.7 | Artifact attenuation | 44 |
| Figure 3.8 | Comparison with wavelet denoising | 46 |
| Figure 3.9 | Comparison with adaptive wavelet denoising | 47 |
| Figure 3.10 | Artifact power attenuation versus NMSE for 3 subjects | 48 |
| Figure 3.11 | Correlation with artifact intensity | 49 |
| Figure 3.12 | Performance comparison with common NIRS artifact removal methods | 50 |
| Figure 4.1 | Sensor block diagram. | 55 |
| Figure 4.2 | Sensor components | 56 |
| Figure 4.3 | Timing of sampling. | 58 |
| Figure 4.4 | Snapshot of the LED driving current. | 59 |
| Figure 4.5 | Detector's signal | 60 |
| Figure 4.6 | PC user interface screen shot. | 61 |
| Figure 4.7 | In vitro setup. | 63 |

| | | |
|-------------|--|-----|
| Figure 4.8 | In vitro data. | 64 |
| Figure 4.9 | Sensor placement for in vivo device test. | 65 |
| Figure 4.10 | Voiding result. | 65 |
| Figure 4.11 | Comparison of detected light attenuation in full and empty bladders. | 66 |
| Figure 4.12 | Voiding (reference NIRS). | 67 |
| Figure 5.1 | Experimental design. | 76 |
| Figure 5.2 | fNIRS optode locations | 77 |
| Figure 5.3 | Connectivity matrices. | 79 |
| Figure 5.4 | Temporal evolution of connections. | 80 |
| Figure 5.5 | fNIRS experiment setup. | 82 |
| Figure 5.6 | Optode placement on the head. | 83 |
| Figure 5.7 | Signal recorded from two channels with high degree of connection. | 88 |
| Figure 5.8 | Group level RSFC maps | 89 |
| Figure 5.9 | The connectivity map for the 2 subgroups | 90 |
| Figure 5.10 | Correlation between connection strengths in the two subgroups. | 90 |
| Figure 5.11 | ROI connections comparison. | 91 |
| Figure 5.12 | Lateralization index for the language network. | 91 |
| Figure 6.1 | Block diagram of the overall fNIRS system. | 96 |
| Figure 6.2 | Block diagram of the laser diode driver module. | 97 |
| Figure 6.3 | Direct digital synthesizer block diagram. | 98 |
| Figure 6.4 | In phase-quadrature demodulation scheme. | 99 |
| Figure 6.5 | Arterial occlusion test. | 104 |
| Figure 6.6 | Isometric contraction results. | 105 |
| Figure 6.7 | Total hemoglobin changes in response to motor activity | 105 |
| Figure 6.8 | Block averaged hemodynamic response. | 106 |

List of Abbreviations

| | |
|-------------|--------------------------------------|
| ADC | Analog to Digital Converter |
| AMT | Active Motor Threshold |
| APD | Avalanche Photodiode |
| AR | Autoregressive |
| AUC | Area Under the Curve |
| BOLD | Blood Oxygen-Level Dependent |
| CBSI | Correlation-based Signal Improvement |
| CW | Continuous Wave |
| DAC | Digital to Analog Converter |
| DAQ | Data Acquisition |
| DC | Directed Coherence |
| DDS | Direct Digital Synthesis |
| DPF | Differential Pathlength Factor |
| DWT | Discrete Wavelet Transform |
| EEG | Electroencephalography |
| FD | Frequency Domain |

| | |
|--------------|---|
| fMRI | functional Magnetic Resonance Imaging |
| fNIRS | functional Near Infrared Spectroscopy |
| FWT | Fast Wavelet Transform |
| GLM | Generalized Linear Model |
| GUI | Graphical User Interface |
| HRF | Hemodynamic Response Function |
| LD | Laser Diode |
| LED | Light Emitting Diode |
| LUTS | Lower Urinary Tract Symptoms |
| MAD | Median Absolute Deviation |
| MBLL | Modified Beer-Lambert Law |
| MCU | Microcontroller Unit |
| MEG | Magnetoencephalography |
| MEP | Motor Evoked Potential |
| MRI | Magnetic Resonance Imaging |
| MS | Multiple Sclerosis |
| MVAR | Multivariate Autoregressive |
| NCDF | Normal Cumulative Distribution Function |
| NEP | Noise Equivalent Power |
| NIRS | Near Infrared Spectroscopy |
| NMSE | Normalized Mean Squared Error |
| OD | Optical Density |

| | |
|-------------|--|
| PC | Personal Computer |
| PCA | Principal Component Analysis |
| PCB | Printed Circuit Board |
| PET | Positron Emission Tomography |
| PFS | Pressure Flow Study |
| PM | Premotor area |
| PPG | Photoplethysmography |
| RMS | Root Mean Square |
| ROI | Regions Of Interest |
| RSFC | Resting State Functional Connectivity |
| rTMS | repetitive Transcranial Magnetic Stimulation |
| SNR | Signal to Noise Ratio |
| SAD | Sum of Absolute Differences |
| SPI | Serial Peripheral Interface |
| SURE | Stein's Unbiased Risk Estimator |
| TD | Time Domain |
| TIA | Transimpedance Amplifier |
| TIWT | Translation Invariant Wavelet Transform |
| TMS | Transcranial Magnetic Stimulation |
| TOI | Tissue Oxygenation Index |
| UTI | Urinary Tract Infection |

Acknowledgments

This dissertation could not have been completed without the support and encouragements I received from many people.

First and foremost, I would like to offer my sincere gratitude to my supervisor, Prof. Guy A. Dumont, for his continuous guidance, advice and patience throughout my PhD studies. He has not only been a caring and dedicated supervisor, but also a great supportive mentor allowing me to pursue my ideas and interests.

I am extremely grateful to my co-supervisor, Prof. Janet F. Werker for her wonderful support and guidance. I consider myself very fortunate for having the opportunity to work with her and benefit from her valuable experience and expertise. I admire her for being so dedicated, supportive and caring towards her students.

I would also like to thank my PhD supervisory and examining committee members, Prof. Matthew Yedlin, Prof. Darlene Reid, Prof. Edmond Cretu and Prof. Jane Wang for dedicating their valuable time and effort to reviewing this thesis and providing advice and feedback which has contributed significantly to the improvement of this thesis.

I would like to extend my gratitude to my external examiner, Prof. Martin Wolf for his invaluable feedback and comments on the thesis. His expert advice and suggestions had a significant role in improving this work.

Throughout this project, I had the opportunity to work with a number of groups and researchers. It was my great pleasure to collaborate with Prof. Andrew Macnab, who generously shared his experience and expertise in the field of biomedical optics with me. I would like to especially thank Dr. Babak Shadgan for offering his valuable clinical and technical expertise, advice and mentorship in all stages of my

studies. I would also like to thank Prof. Hossein A. Noubari and Prof. Lara Boyd for their support and guidance. I wish to thank Prof. Lukas Chrostowski and Prof. David Jones for offering their technical advice, support and fruitful discussions on development of the optical systems used in this dissertation.

I owe special thanks to Dr. Henny Yeung, Dr. Judit Gervain, Dr. Krista Byers-Heinlein, Lilian May and Alison Gruel for their help and support in collecting the experimental data, providing feedback and their contribution in developing methods and ideas presented in Chapter 3, Chapter 5 and the rest of the thesis.

Many thanks to my great friends and colleagues at the University of British Columbia, Ali Shahidi Zandi, Pedram Ataei, Christopher Brouse, Masoud Rahjoo, Mehrnoush Javadi, Sara Khosravi, Prasad Shrawan, Parastoo Dehkordi, Reza Tafreshi, Ping Yang, Mande Leung, Walter Karlen, Jin oh Hahn and Klaske van Heudsen who provided a friendly environment, kept me in good company and made my graduate studies such a wonderful and rewarding experience.

I would also like to express my sincere appreciation to my brother, Dr. Behzad Molavi for his encouragements, inspirations and support in pursuing my PhD.

My sincere gratitude to my parents, whose never-ending love has given me inspiration and hope in every step of my life.

Finally, I wish to express my deepest appreciation to my wife and my best friend, Zamzam Kordi without whom none of this would have been possible. Her unconditional love and support at times of despair and frustration gave me the courage, hope and motivation to continue this journey.

Dedication

To my parents, and my wife ...

Chapter 1

Background

1.1 Introduction to Near Infrared Spectroscopy

Oxygen is a critical component in living organisms and its concentration in tissue is an important parameter indicative of tissue metabolism, level of activity and health condition. As a result, measuring oxygen concentration in the tissue is essential in many clinical and research applications.

In 1977 Jobsis introduced the method of measuring local tissue oxygenation non-invasively using near infrared light [7]. Absorption of the light by living tissue is lower in this wavelength range (600-1000 nm) which results in maximum penetration depth. Below this wavelength range, hemoglobin strongly absorbs light and above this range, water is the major absorber. Figure 1.1 shows the absorption spectra of light energy as a function of wavelength in the vicinity of NIR wavelengths for important species in tissue. Within this range, light attenuation occurs as a result of scattering and absorption by chromophores such as oxygenated and deoxygenated hemoglobin (HbO_2 and HHb) which are important biological indicators, lipid, water and cytochrome oxidase. This method of using NIR light to measure chromophore concentration (or concentration changes) in the tissue is known as Near Infrared Spectroscopy (NIRS). In practice, a light point source is placed on the tissue surface to shine light into the tissue. A light detector, also located on the surface, but at a distance from the source detects diffusively reflected light from within the tissue and extracts information on the chromophore concen-

tration from the detected light intensity and phase. The intensity attenuation is due to absorption by blood chromophores as well as scattering and can be related to the changes in concentration of the chromophores.

The unique type of information provided by NIRS is quite different from that obtained with pulse oximetry or Photoplethysmography (PPG), even though the basic principles are similar. NIRS and PPG are based on the same principle that NIR light can penetrate in the tissue and is mostly absorbed by hemoglobin species. However, PPG measures arterial oxygen saturation which is the percentage of hemoglobin in arteries that is bound to oxygen:

$$SpO_2 = \frac{aHbO_2}{aHbO_2 + aHHb} \quad (1.1)$$

where SpO_2 is the peripheral oxygen saturation, and $aHbO_2$ and $aHHb$ are the arterial HbO₂ and HHb concentrations, respectively. This fraction which is normally close to 100%, is a centrally controlled parameter and only changes in response to critical conditions.

NIRS measures tissue oxygenation changes or in some cases, tissue oxygen saturation which is the percentage of hemoglobin bound with oxygen in the tissue. This parameter can change significantly in response to increase or decrease in oxygen demand in the tissues. For example, it has been shown that under an incremental inspiratory threshold loading study, the SpO_2 stayed relatively constant throughout the experiment ($\geq 96\%$), while NIRS showed decrease in tissue oxygenation of a non active muscle and increase in oxygenation of the active muscle [8].

In general, NIRS can be employed in any application where hemodynamics of a tissue is of importance. Because of its non-invasive nature and the unique type of information it provides about tissue hemodynamics, NIRS has become very popular and has found a wide range of applications such as monitoring muscle or brain oxygenation [9], brain computer interface [10], rehabilitation [11] and cancer detection [12].

Brain functional studies are among the application areas in which NIRS is promising. Due to neurovascular coupling, the neural activation which is accompanied by hemodynamic changes resulting from an increase in oxygen demand,

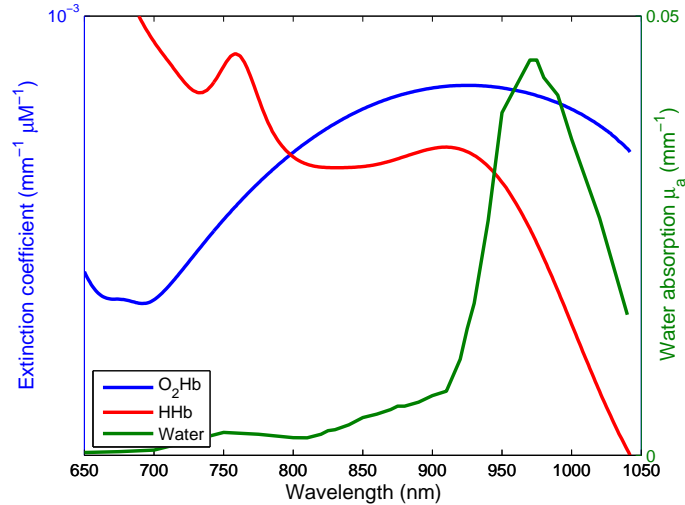


Figure 1.1: Absorption spectra of oxygenated and deoxygenated hemoglobin (HbO_2 and HHb) and water from 600nm to 1000nm. The absorption increases significantly below 600nm and above 1000nm.

can be detected using NIRS in superficial areas of the brain [13]. This method, known as fNIRS, is widely used to detect activations in brain cortex in response to different stimulations. The information recorded by functional Near Infrared Spectroscopy (fNIRS) is very similar to that obtained by functional Magnetic Resonance Imaging (fMRI) and Positron Emission Tomography (PET). However, fNIRS is less expensive, portable, non ionizing, non restraining and has higher temporal resolution. Also, the process of hemodynamic changes detection is different between fMRI and NIRS. In fMRI, magnetic properties of hemoglobin are used to detect changes in HHb [14]. Losing oxygen causes hemoglobin to demonstrate paramagnetic properties. In fNIRS, the difference in absorption spectra of HbO_2 and HHb is the principle of detection. As a result, NIRS is sensitive to both HbO_2 and HHb while fMRI is only sensitive to HHb . This is an important difference as the change in HbO_2 in response to stimulation is larger and more correlated with Blood Oxygen-Level Dependent (BOLD) response than HHb [15].

1.2 Theory of NIRS

1.2.1 Modified Beer-Lambert Law

In order to derive chromophore concentrations, raw light intensity readings need to be converted to concentrations or concentration changes. The Beer-Lambert law describes the attenuation of light when propagating in a non scattering, but absorbing medium:

$$I = I_0 e^{-\mu_a l} \quad (1.2)$$

where I_0 is the intensity of the light entering the medium, I is the light intensity at location $x = l$ with l in cm and μ_a is the attenuation coefficient in cm^{-1} . In presence of multiple absorbants, this coefficient is related to the absorbants' concentration as

$$\mu_a = \sum_i \varepsilon_i c_i \quad (1.3)$$

where c_i and ε_i are the concentration and extinction coefficient of the i th absorber in molL^{-1} and $\text{Lmol}^{-1}\text{cm}^{-1}$, respectively. In a highly scattering medium, such as human tissue, this equation is no longer valid as absorption is not the only mechanism resulting in light intensity attenuation. The modified form of this equation known as the Modified Beer-Lambert Law (MBLL) takes scattering into consideration and explains the relationship between chromophores' concentration and reflected optical density [16]:

$$OD = -\log \frac{I}{I_0} = \varepsilon c l B + G \quad (1.4)$$

where OD is the optical density, I_0 is the incident light intensity, I is the detected light intensity, ε and c are the same as described above, l is the distance between where the light enters the tissue and where the detected light exits the tissue, B is a pathlength factor that accounts for increases in the photon pathlength caused by tissue scattering, and G is a factor that accounts for the constant losses such as those caused by measurement geometry [16].

A change in the concentration of the chromophore will result in a change in the reflected light's intensity which is sensed at the detector. When concentration

changes, ε and distance l remain constant. Assuming B and G also remain constant, we can rewrite equation 1.4 as

$$\Delta OD = -\log \frac{I_{Final}}{I_{Initial}} = \varepsilon \Delta CLB \quad (1.5)$$

where $\Delta OD = OD_{Final} - OD_{Initial}$ is the change in the optical density, I_{Final} and $I_{Initial}$ are the measured intensities before and after the change in the chromophore concentration, and ΔC is the change in concentration. L is determined by the probes geometry, ε is the property of the chromophore and B is often referred to as the Differential Pathlength Factor (DPF) and can be determined with very short pulses of light and has been tabulated for various tissues.

In order to consider the contribution of two or more chromophores, we need to write equation 1.5 for 2 different chromophores and make measurements at more than 1 wavelength. In this way, OD changes at wavelength λ would be:

$$\Delta OD^\lambda = \left(\varepsilon_{HbO_2}^\lambda \Delta [HbO_2] + \varepsilon_{HHb}^\lambda \Delta [HHb] \right) B^\lambda L \quad (1.6)$$

by measuring the ΔOD in 2 wavelengths, one can solve for changes of concentration in HbO_2 and HHb using

$$\Delta HHb = \frac{\varepsilon_{HbO_2}^{\lambda_2} \frac{\Delta OD^{\lambda_1}}{B^{\lambda_1}} - \varepsilon_{HbO_2}^{\lambda_1} \frac{\Delta OD^{\lambda_2}}{B^{\lambda_2}}}{\left(\varepsilon_{HHb}^{\lambda_1} \varepsilon_{HbO_2}^{\lambda_2} - \varepsilon_{HHb}^{\lambda_2} \varepsilon_{HbO_2}^{\lambda_1} \right) L} \quad (1.7)$$

$$\Delta HbO_2 = \frac{\varepsilon_{HHb}^{\lambda_1} \frac{\Delta OD^{\lambda_2}}{B^{\lambda_2}} - \varepsilon_{HHb}^{\lambda_2} \frac{\Delta OD^{\lambda_1}}{B^{\lambda_1}}}{\left(\varepsilon_{HHb}^{\lambda_1} \varepsilon_{HbO_2}^{\lambda_2} - \varepsilon_{HHb}^{\lambda_2} \varepsilon_{HbO_2}^{\lambda_1} \right) L} \quad (1.8)$$

The MBL is sufficient in cases where only the measurement of changes from a baseline is desired. This baseline is dependent on different factors (source detector coupling with the tissue, tissue parameters etc.). As a result, removing an optode and replacing it in the exact same position on the tissue, will result in different baseline reading and therefore absolute reading values are not comparable. Therefore, if absolute values of chromophores or Tissue Oxygenation Index (TOI) measurements are required, this model will not be adequate.

1.2.2 Photon Diffusion in Tissue

A more robust model of light-tissue interaction is based on using diffusion equation to describe light propagation in highly scattering living tissue. Assuming an isotropic source, the light-tissue interaction can be described by the diffusion equation [17]:

$$\nabla \cdot (D(\mathbf{r})\nabla\Phi(\mathbf{r},t)) - v\mu_a(\mathbf{r})\Phi(\mathbf{r},t) - \frac{\partial\Phi(\mathbf{r},t)}{\partial t} = -vS(\mathbf{r},t) \quad (1.9)$$

where $\Phi(\mathbf{r},t)$ is the photon fluence rate at position \mathbf{r} and time t in Wcm^{-1} , $S(\mathbf{r},t)$ is the source power per volume emitted radially outward in Wcm^{-1} , $D(\mathbf{r}) = \frac{v}{3(\mu'_s(\mathbf{r})+\mu_a(\mathbf{r}))}$ is the photon diffusion coefficient, μ'_s is the reduced scattering coefficient, μ_a is the absorption coefficient and v is the speed of the light in the medium.

The reduced scattering coefficient is related to scattering coefficient as $\mu'_s = (1-g)\mu_s$ and characterizes the amount of scattering in the tissue.

In order to characterize the diffusion of light in the tissue, different source and boundary conditions can be assumed. Here, we briefly look at 2 simple cases which are relevant here.

For the case of a frequency modulated source

$$S(\mathbf{r},t) = S_{dc}(\mathbf{r}) + S_{ac}(\mathbf{r})e^{-i\omega t} \quad (1.10)$$

where S_{dc} and S_{ac} are the constant and time varying components of the source. In this case, the time varying part of the solution would also have the same frequency as the source and will have the form of

$$\Phi_{ac}(\mathbf{r},t) = U(\mathbf{r})e^{-i\omega t} \quad (1.11)$$

assuming a homogeneous medium, the diffusion equation reduces to

$$(\nabla^2 - k^2)U(r) = -\frac{v}{D}S_{ac}(r) \quad (1.12)$$

where $k^2 = \frac{v\mu_a - i\omega}{D}$. For a point source at position $\mathbf{r} = r$ in infinite space

$$S_{ac}(\mathbf{r}) = S_{ac}\delta(r) \quad (1.13)$$

The general solutions to Equation 1.12 are of the form Ce^{kr} and Ce^{-kr} . One can then solve Equation 1.12 to get [17]

$$U(r) = \frac{\nu S_{ac}}{4\pi D r} e^{-kr} \quad (1.14)$$

where k is a complex number with real part

$$k_r = \left(\frac{\nu\mu_a}{2D}\right)^{1/2} \left(\left(1 + \left(\frac{\omega}{\nu\mu_a}\right)^2\right)^{1/2} + 1 \right)^{1/2} \quad (1.15)$$

and imaginary part

$$k_i = -\left(\frac{\nu\mu_a}{2D}\right)^{1/2} \left(\left(1 + \left(\frac{\omega}{\nu\mu_a}\right)^2\right)^{1/2} - 1 \right)^{1/2} \quad (1.16)$$

Hence, at location r on tissue surface, the light intensity would be frequency modulated at the same frequency of the source with reduced amplitude and a phase shift which are both functions of μ_a and D .

A more realistic boundary condition is a semi-infinite homogeneous medium. In this case, an image source symmetric around the boundary can be used to satisfy the boundary condition. In the limit where we are far enough from the source, the solution can be written as

$$U(\rho, z = 0) \approx \frac{\nu S_0}{4\pi D} \frac{e^{-k\rho}}{\rho^2} (2k(l_{tr}z_b + z_b^2)) = \frac{A_0 e^{-k_r\rho}}{\rho^2} e^{i(-k_i\rho + \theta_0)} \quad (1.17)$$

which again indicates attenuation along with a phase shift at position r with respect to the source. In case of a non modulated source, one would get the exponential decrease in intensity only. The application of these formulations in deriving concentration values in different NIRS instruments will be discussed in Section 1.4.

1.3 Applications of NIRS

The unique advantages of NIRS has led to its use in a variety of applications. NIRS in general, is applicable in any situation where hemodynamic monitoring of a tissue

is required.

One of the areas in which NIRS is well suited for are brain studies which involve recording activities in different brain areas. In these studies, neurovascular coupling results in increase in hemodynamics that lags the neural activation. This change can be detected by fNIRS. The data is then converted to activation using mathematical models incorporating the hemodynamic response function. In fNIRS studies, one would only be interested in measuring changes in chromophore's concentration from a baseline and therefore, continuous wave fNIRS devices that measure concentration changes using MBLL are well suited for these applications.

fNIRS has been used for studying various brain disorders. Hock et al. have examined Alzheimer's patients during verbal fluency and other cognitive tasks, finding decreases in HbO₂ and total hemoglobin (tHb) relative to the baseline in the parietal lobe as compared to an increase in HbO₂ and tHb in healthy subjects [18, 19]. Schizophrenia patients have also been studied with fNIRS in several studies. In one study, for example, "dysregulated" patterns of HbO₂ and HHb change were found using fNIRS in frontal regions of schizophrenic patients as compared to healthy subjects during a mirror drawing task [20]. Also, it was shown that the typical pattern of right-lateralized activation during a continuous performance test was absent in schizophrenic patients [21]. Depression is another condition examined with NIRS. In a study by Matsuo, reduced frontal activation during a verbal fluency test in patients suffering from depression was found compared to controls [22]. These are only a few representative examples of applications of fNIRS in brain disease conditions. A more detailed review of such applications can be found elsewhere [23].

One of the attractive areas of application for NIRS is brain studies in infants where use of other modalities such as fMRI or PET is either impractical or very difficult. Also, the small head size and thin skull results in high quality and better penetration into brain tissue. For example, unique features of fNIRS has made it possible to assess newborn infant's brain response to different languages and language structures [24]. NIRS has also been used to study developmental changes in the cerebral hemodynamic response to different stimulation types [25, 26].

One of the more recent developments in applications of NIRS has been the study of bladder muscle hemodynamics during voiding to diagnose bladder ob-

struction/dysfunction non-invasively [27]. It has been shown that patterns of HbO₂ and HHb are different for normal and obstructed bladder reflecting variations in detrusor muscle hemodynamics and oxygen supply and demand. This can potentially replace invasive methods currently in practice for urodynamics tests.

New applications for NIRS are constantly being developed and tested. Validation of such data in different fields has turned NIRS into a promising diagnostic tool.

1.4 NIRS Instrumentation

There is a wide variety of NIRS instruments currently in use, both commercial ([28–33]) and custom-built ([34–38]). A detailed review of different NIRS devices and measurement techniques can be found elsewhere [23, 39, 40].

In terms of operation basis, the NIRS devices can be divided into 3 categories: Continuous Wave (CW), Time Domain (TD) and Frequency Domain (FD) devices [41].

TD systems use very short light pulses which are scattered and absorbed by the tissue layers. The temporal distribution of photons as they leave the tissue is detected by the system. The shape of this distribution gives information about the tissue scattering and absorption. TD systems provide very accurate estimations of tissue parameters (scattering coefficient μ_s and absorbing coefficient μ_a). However, they are usually expensive, bulky and require extensive knowledge of the system to work with and are not particularly suitable for practical clinical applications.

In FD systems, the light source is amplitude modulated at intermediate frequencies (around 100MHz). As discussed in Section 1.2, the amplitude and phase of the light at the detector is a function of reduced scattering coefficient μ'_s and absorption coefficient μ_a . Hence by measuring amplitude and phase of the modulated light at the detector, the chromophore concentrations can be calculated.

CW systems are the most widely used NIRS devices in practice. They radiate light continuously into the tissue and measure the amplitude decay of the reflected signal. In the simple basic form, these systems can not quantify baseline absorption and scattering. However, they can be made with inexpensive, widely available components. Even though CW systems are often used for measuring slow hemo-

dynamic signals [42], they can measure the fast neuronal signals under certain conditions [43–45]. These devices usually incorporate the MBLL model for estimating the absorption coefficient in the tissue. One of the major limitations of using CW NIRS devices with single source-detector pair based on MBLL is that they can only measure "changes" in tissue hemodynamics. In other words, the absolute values of chromophores can not be measured. This means a dynamic should be generated in order to observe the changes. This dynamic could be in different forms including stimulation (brain studies), muscle activity (sports medicine, bladder study), occlusion or drug administration. Even though some applications are still feasible using measurement of changes from baseline only, this will rule out possibility of using NIRS in many other areas. Therefore, several methods have been proposed to alleviate this problem in CW systems. Most of these techniques use a more realistic model for light-tissue interaction to estimate the tissue optical parameters and hence, the concentration.

A sub class of CW devices use the diffusion model to estimate parameters such as tissue oxygen saturation index. If we assume a non modulated source in Section 1.2, the detected amplitude at position ρ would be:

$$U(\rho, z = 0) = \frac{A_0 e^{-k_r \rho}}{\rho^2} \quad (1.18)$$

Therefore, if signals are recorded at multiple detectors with different ρ , one can estimate the slope of $\ln \rho^2 U(\rho)$ and derive μ_a , given some simplifying assumptions on μ_s (see [46] for example). Such devices are also known as spatially resolved NIRS and are capable of measuring absolute values of tissue oxygen saturation.

Laser Diodes (LDs) and Light Emitting Diodes (LEDs) are the two commonly used discrete wavelength light sources for NIRS. LDs have narrower spectral width than LEDs, however, LEDs are cheaper and do not have stability issues of laser diodes.

Common detectors used in NIRS instruments are silicon PIN photodiodes, Avalanche Photodiode (APD)s and **PM T! (PM T!)**. Silicon photodiodes are inexpensive detectors with high quantum efficiency, however, they are not very sensitive and are best for applications where detected light levels are high. APDs are more sensitive and they provide internal gain through internal avalanche multipli-

cation, but they are more expensive. PMTs have very high gain-bandwidth product and are used when very high sensitivity is required.

Selection of source wavelengths in a NIRS device is an issue that can affect the signal quality and is an important topic of interest [17]. Traditionally, for dual wavelength systems, wavelengths have been chosen in such a way that one is above and the other one is below the isosbestic point. Isosbestic point is the wavelength at which HbO₂ and HHb have equal absorption in the NIR window (around 800 nm). However, it has been shown that some specific combinations of wavelengths may result in better separation of HbO₂ and HHb and less cross talk between chromophores as a result of solving Equation 1.3 [47]. Optimal selection of wavelengths has been a subject of study with dual [48–50] and multi-wavelength NIRS configurations [51, 52].

1.5 Safety Considerations

NIRS is a relatively safe optical method as it uses non-ionizing radiation, is generally non-invasive and uses low power light radiation to examine the tissue. The major safety concerns for the NIRS light power are damage to the eye and skin tissue. In this particular wavelength range, tissue heating is the major process of concern that can potentially lead to tissue damage. This process is more of a concern for eye as the light is focused on the retina by the lens which can increase the potential hazards. There are many factors that affect the potential of light for causing damage to the tissue including the source type (e.g. coherent vs non-coherent), source power, exposure time, wavelength and the beam spot size. The safety power limits for laser light sources can be found in guidelines such as IEC 60825-1 and ANSI Z136 standards [53]. Similar guidelines for LED based devices are defined separately in IEC 62471 [54]. The safety of LED based NIRS devices that are in direct contact with the tissue have also been investigated in terms of tissue heating caused by the radiance as well as conducted heat from the semiconductor junction [55]. As a rough estimate, the average power level of the LED or laser of less than 10 mW in adults is normally considered safe [56]. Most commercial devices use power levels of 0.5-1.5 mW which is safe even for application on newborn infants [57].

1.6 Limitations of NIRS

Some limitations of NIRS that need to be considered in any application are reviewed in this section. More detailed review of the limitations of NIRS can be found elsewhere [39, 58, 59].

1.6.1 Penetration Depth and Spatial Resolution

High scattering in the living tissue causes light to go through a banana shape volume before reaching the receiving optode on the tissue surface. As a result, the signal detected at the detector reflects a combination of changes in hemodynamics in the entire sampled volume. The mean penetration depth depends on the source-detector separation as well as the tissue scattering and absorption properties and has been investigated using theoretical models for light propagation in tissue [60]. As a rough estimate, the mean penetration depth or the depth of maximum sensitivity of NIRS can be considered to be of order of half interoptode distance [17]. A more accurate equation for the penetration depth can be found in [60]. However, it should be noted that the signal still contains interferences from other layers. This also limits the spatial resolution of the NIRS. In some studies, such as sports medicine studies, this may not be an issue as the overall change in the muscle tissue, for instance, is of interest. However, in fNIRS this spatial resolution may be a limitation as one can not precisely localize activation to very specific small brain areas. However, more general and superficial areas such as dorsolateral prefrontal cortex, superior parietal cortex, and language and primary sensorimotor areas are within detectable limits [58].

1.6.2 Light Coupling

One of the challenges in NIRS is achieving good, stable optical contact between the tissue and the optodes to get sufficient light levels [58]. One of issues in achieving a good coupling is the optode placement on the tissue. In fNIRS in particular, this introduces a challenge and different types of holders have been proposed to address this issue as a properly secured optode plays an important role in achieving a good signal quality [61]. The specific requirements of an optode holder depend on the subject populations and therefore, the type of the holder used in a study on adults

for example, would be different from one used in infants' study [57]. In the case of fNIRS, the optode holder secures the optodes on the tissue to provide a good coupling past the hair and reducing the effect of subject's motion. A layer of hair can attenuate light and block the tissue from the source light [61]. Hair follicles also strongly absorb near infrared wavelengths [58]. In adults, care must be taken to move the hair aside before placement of the optodes. Also, it has been suggested that holding the optodes a few millimeters away from the tissue can reduce the effect of light obstruction by layers of hair and help in achieving a better coupling [61].

1.6.3 Interferences

In NIRS, the hemodynamic changes correlated with activity of the tissue under study are the parameters of interest. However, NIRS signal can be contaminated with interferences with other sources of origin.

One major source of unwanted interference is motion. Movements of various types result in distortion of the data stream broadly referred to as motion artifact. Motion can result in data distortion through different mechanisms. For example, movement can cause changes in the local blood circulation. Decoupling of source and detector from tissue due to subject's motion is another common source of artifact. Such artifact is evident as non-physiological signal changes, often of large magnitude, that commonly result from alterations in the apposition of the NIRS light source and photo detector to the tissue with resulting alteration in pathlength. The distortion of motion artifact obscures trends in the data that may be relevant, and can compromise meaningful analysis of NIRS monitoring data. Removal of such artifact is often an essential pre-processing step for accurate analysis of the signal. Motion artifact removal is especially of interest in fNIRS as the level of the signal of interest is already low and care must be taken to extract as much information as possible from the recorded data and exclude as few blocks as possible due to motion contamination. Common approaches along with the approach developed in this thesis for this purpose are presented in Chapter 2 and Chapter 3.

Another source of interference in NIRS is the systemic interference. Figure 1.2 shows the power spectrum of a typical fNIRS signal segment acquired from the

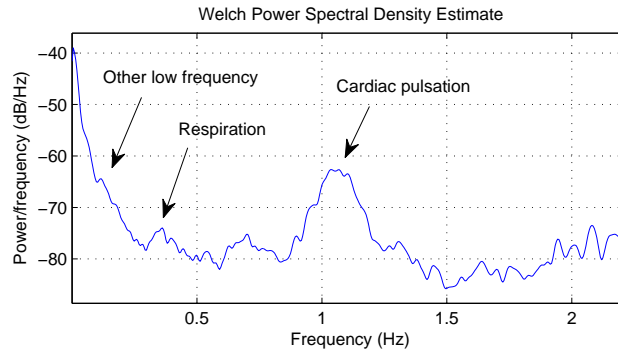


Figure 1.2: Power spectrum of fNIRS data collected from forehead at rest. The black arrows indicate systemic interferences at different frequencies in the fNIRS signal. The peaks around 1.1 Hz and 0.35 Hz are caused by cardiac pulsation and respiration, respectively. The peak at 0.1 Hz may be related to the heart rate variability and the Mayer waves.

forehead of a 30 year old healthy subject at rest condition using the instrument described in Chapter 6. Two most common interferences are cardiac pulsation and respiration (shown with arrows in the figure). Cardiac pulsation (the peak around 1.1 Hz in Figure 1.2) results in a small diameter change in the blood vessels as a result of expansion and contraction of the vessels. This will lead to fluctuations in absorption of light due to changes in blood volume within the sampling volume. This can be seen as a pulsation interference in the NIRS signal and is more evident in HbO_2 compared to HHb . Respiratory interference is related to the respiratory variations in arterial pulse pressure and is observed in frequencies between 0.1 and 0.4 Hz [62]. Heart rate variability component can also be observed at lower frequencies (0.01-0.1 Hz) for longer recorded signals. Mayer waves are also another source of interference around 0.1 Hz (see Figure 1.2). These interferences are in fact a rich source of information and contain valuable physiological information which can be relevant in many applications. However, in cases where the main interest is only the changes in tissue oxygenation, it would be essential to remove these interferences to avoid misinterpretation of the NIRS data.

A more detailed description of these systemic interferences can be found in [62].

1.7 Motivation for this Thesis

One factor that has limited experimental applications of NIRS is the sensitivity of this method to movement of the tissue of interest during the measurement. This can happen when, for example the subject moves spontaneously, with involuntary muscle contraction, with repositioning of area being monitored, or when the NIRS optodes are not attached optimally to the tissue surface [40]. The effects of movement have limited clinical applications of NIRS in ambulant patients as well as experimental applications of NIRS monitoring in exercise science and sports medicine. Movements of various types result in distortion of the data stream broadly referred to as motion artifact. Such artifact is evident as non-physiological signal changes, often of large magnitude, that commonly result from alterations in the apposition of the NIRS light source and photo detector to the tissue with resulting alteration in pathlength. The distortion of motion artifact obscures trends in the data that may be relevant, and can compromise meaningful analysis of NIRS monitoring data. Hence, removal of such artifact is potentially of value and is often an essential pre-processing step for accurate analysis of the signal. The importance of this pre-processing step has resulted in introduction and development of several motion artifact treatment methods in recent years [63–67]. Developing an effective and efficient algorithm for removing or reducing motion artifacts in order to improve the quality of NIRS signal has been one of the major motivations for this thesis.

One of the more recent applications of NIRS is in urology where the detrusor is being monitored by NIRS for hemodynamic changes. One potential and unexplored application of NIRS is providing a monitoring method for people with bladder control problems. Bladder control problem occurs in a variety of conditions including spinal cord injury, Multiple Sclerosis (MS) and stroke. For affected patients the problems that result range from accidental leakage of urine by day (incontinence) or bed wetting at night (enuresis), through to an inability to empty the bladder (urinary retention). Urinary retention has potentially serious consequences, particularly in patients with abnormal bladder function secondary to spinal cord injury. In such cases, not being aware that the bladder is full can lead to back pressure developing in the urinary tract that risks serious damage to the kidneys. In all these cases, a wearable non-invasive device that monitors the fullness of the bladder and

provides and alarm once the volume of urine in the bladder has reached a pre-set threshold, would be beneficial. Individual patients would then, depending on their pathology, be able to empty their bladder voluntarily to avoid incontinence. In children with nocturnal enuresis, a problem that affects 20% of children over four years of age[68] , a device that wakes the patient with an alarm once the bladder is full, but before incontinence occurs, has major advantages over current systems that only detect accidental voiding. Enabling the subject to wake, sense that his/her bladder is full, and void voluntarily before leakage occurs, would lead to conditioning over time to waking in response to the bladder being full, and resolve the enuresis. This is an example of an application area where motion artifact reduction is essential for long term monitoring purposes. Proper motion artifact reduction methods should be integrated into such a device to make it practical for clinical applications.

The interaction between spatially separated cortical regions in the human brain plays an important role in performing a particular task. Functional imaging methods such as fNIRS can identify different cortical regions involved in a task. However, possible functional connections and interactions among activated areas are not directly reflected in such images without further processing. These connections, in addition to providing insight into brain's architecture and function, may enable one to predict certain brain disorders. As discussed in Chapter 2, it has been shown that functional connectivity may be able to identify broken cortical networks in particular disease conditions. fNIRS appears to be a suitable tool for mapping brain functional connectivity specially in infants. This group of subjects were of special interest to us as our collaborators have been working on the development of language system in infants. This research has had major impact in both technical community [24, 69, 70] as well as general media [71]. One question that was left unanswered was how this language network and its connections form and develop with maturity. This question is of particular value as there is a growing body of evidence on the brain areas involved in language processing in neonates, but less on the underlying connectivity. As a result, exploring methods of mapping functional connectivity with fNIRS was another area of focus in this thesis. Treatment of motion artifacts is a required pre-processing step for reliable results from connectivity analysis.

One of the potential applications for NIRS is to monitor the effect of different types of stimulation on the brain. In particular, Transcranial Magnetic Stimulation (TMS) which magnetically stimulates the brain is one of the methods that has been a subject of study using fNIRS. Due to the strong magnetic pulse created by the TMS coil, monitoring the effect of TMS on brain is a challenging task for most of the common neuroimaging techniques. Being dependent on optical signal for its functionality, fNIRS is relatively immune to this problem and is therefore a good fit for monitoring the brain hemodynamics and neural activations during the stimulation. The most common approach in this case is to study the effect of TMS on the hemodynamics of the stimulation target area or the areas closely related to it. However, one interesting question is how TMS affects and modulates the brain networks. This can be investigated either with concurrent TMS-NIRS to look at network and connectivity changes in a shorter time scale, or by doing connectivity analysis following TMS to study the lasting effect of TMS on a particular cortical network. Resting State Functional Connectivity (RSFC) analysis using fNIRS provides a useful tool for monitoring this effect in a non expensive and easy to use manner. Because of the special needs and requirements of using NIRS with TMS, a customizable and preferably an in house made fNIRS device is highly desirable. In particular, a custom made NIRS instrument with high enough sensitivity and sampling rate can potentially measure the fast optical signal [72] which allows one to look at the network changes in a concurrent TMS-NIRS study and evaluate more "elastic" changes that occur in a shorter time scale [73].

Development of a motion artifact reduction method as a required pre-processing step was the initial focus of this thesis which forms a signal processing basis for the rest of the thesis. Development of a new approach for analyzing resting state functional connectivity for potential use in infants as well as in TMS studies and in particular for stroke patients to investigate changes in cortical networks in response to TMS was the next major area of interest. In order to look at both short and long time scale changes in connectivity, we aimed at developing and testing a custom made NIRS device appropriate for concurrent use with TMS. Our final objective was to use NIRS to develop a new wearable bladder monitoring sensor for patients with bladder control problem which is an example of a device that can significantly benefit from our artifact removal technique due to the inherent problem of motion

which is a result of engagement in routine daily activities by the subject wearing the sensor.

1.8 Thesis Contributions

The major contributions of this thesis are summarized in this section. This thesis

- Introduces a novel method for removal of motion artifacts from fNIRS data using the Discrete Wavelet Transform (DWT). This method was adopted as one of the fNIRS motion artifact removal methods in HOMER2 NIRS processing package¹, an open source Matlab toolbox for analyzing fNIRS data developed by MGH-Martinos Center for Biomedical Imaging and widely used by fNIRS community. This method has been subject to independent reviews and comparison with other methods using simulated [74] and experimental NIRS data [75]. The article describing this method appeared in the "Highlights of 2012" collection of the *IOP Journal of Physiological Measurement*. The articles featured in this collection "span some of the most cutting-edge areas of biomedical physics, and collectively are a reflection of the most influential research published in PMEA in 2012" ².
- Introduces a method for identification of wavelet levels for optimum artifact removal performance.
- Develops a novel method and apparatus for optically detecting changes in bladder contents non-invasively with potential application for patients with bladder control problem. This method is currently under review by the University of British Columbia University-Industry Liaison Office (UILO) for potential intellectual property (IP) protection and technology licensing.
- Introduces a method of analyzing time-varying connectivity between cortical regions in infants using fNIRS and Multivariate Autoregressive (MVAR) modeling.

¹www.nmr.mgh.harvard.edu/optics

²Physiological Measurement Highlights of 2012 web page

- Develops a new method for detecting and mapping language network in infants using fNIRS and phase analysis on resting state hemodynamic changes in different cortical regions.
- Describes the design, test and validation of a custom made TMS-compatible fNIRS device for future use in TMS studies on stroke patients.

1.9 Thesis Outline

This chapter provided the background information on NIRS, its applications, potentials and limitations. In Chapter 2 the state of the art research on the four major parts of the thesis, namely, motion artifact removal, NIRS in urology, connectivity analysis with fNIRS and application of fNIRS with TMS is reviewed. In Chapter 3 we present a novel signal processing method to identify and remove motion artifacts from fNIRS data. We present simulation results and comparison with other common preprocessing methods used in fNIRS. Also, the method is applied to NIRS data collected from infants in an fNIRS study to evaluate its performance.

In Chapter 4, we introduce a novel application for NIRS in the form of a proof of concept for a wireless wearable sensor to help individuals with bladder dysfunction determine when their bladder is full.

Chapter 5 is dedicated to investigation of the concept of cortical connectivity using fNIRS. The first part of this chapter provides a preliminary study using MVAR while the latter provides a more elaborate method of connectivity analysis using phase information of the resting state hemodynamic signals.

In Chapter 6 we describe a TMS compatible fNIRS experimental setup for future use in evaluating the effect of TMS in stroke subjects. A custom made fNIRS device has several advantages for monitoring the TMS effect. In particular, due to special needs of NIRS devices used with TMS, being able to modify and adjust NIRS system parameters such as power and sampling rate would be desired. Additionally, a sensitive enough device with high sampling rate may be capable of detecting fast optical signal in response to TMS which is currently not feasible with commercially available NIRS devices.

Finally, Chapter 7 summarizes the methods, results and findings presented in this thesis and identifies some of the possible future directions.

Chapter 2

Literature Review

In this chapter we review the work related to the 4 main topics of this thesis, which are interference reduction in NIRS, applications of NIRS in urology, functional connectivity analysis using fNIRS and applications of NIRS with TMS.

2.1 Interference Reduction in NIRS

Even though artifact removal can in general be beneficial in any NIRS dataset and setup, it has received more attention in fNIRS. The fNIRS data usually contains the weak and noisy hemodynamic data and motion artifacts can have significant impact on detecting the hemodynamic response. As a result, the works reviewed here are mostly focused on applications of artifact and interference removal methods in fNIRS.

In general, there are 3 major approaches to identification and/or removal of interferences and motion artifacts from NIRS signal. One common method is to use an auxiliary input signal whose output is highly correlated with the motion artifacts. This could be from sources such as an accelerometer attached to the optodes or an optical channel sampling from superficial layers of the tissue. This signal is then used to remove the artifact caused by motion from the NIRS signal.

Adaptive filtering is one of the methods commonly utilized with this approach for fNIRS motion artifact removal. Izzetoglu et al. used adaptive filtering with a reference channel from an accelerometer attached to the subject's head to cancel

motion artifacts [76]. Accelerometer seems to be a good reference for adaptive filtering of motion artifact as it is highly correlated with the motion. Other studies have also employed accelerometer reference for baseline correction [77] and artifact removal [78].

Another common form of a reference signal is NIRS data from a reference channel. Robertson et al. applied adaptive filtering to fNIRS, using co-located sources and detectors in each optode to detect and remove motion artifacts [63]. Essentially, the reference channel is selected such that it does not penetrate deep into the tissue and hence, does not capture hemodynamic information from the target tissue. Instead, it will mostly capture changes from superficial layers which are correlated with motion.

Zhang et al. used a similar method with the scalp superficial optical measurement as the reference signal for removing global interferences (such as cardiac pulsation and respiration) from deeper brain functional signals [79]. Essentially, these interferences will appear stronger in the superficial layers and can act as a reference for removing them from the overall signal. Multidistance optode configuration for acquisition of a reference signal has also been used with empirical mode decomposition and adaptive filtering to remove physiological interferences from fNIRS signal [80].

This approach in general can be very effective as it incorporates a direct measure of motion timing and intensity. However, it requires an additional form of recording such as accelerometer signal or extra optical channel to provide a reference signal. Therefore, a modified hardware/experimental setup is required for this approach and is therefore not applicable to the large amount of NIRS data collected in past studies by many researchers in this field.

Another approach to motion artifacts removal is to identify motion contaminated blocks or segments of NIRS data and exclude them from calculation of the mean Hemodynamic Response Function (HRF). This is often used in fNIRS data processing to improve quality of hemodynamic response detection when averaging blocks in a block design study [81]. The motion event in this case has to be first identified with some criteria such as visual inspection of the NIRS signal or recording motion event times while conducting the experiment. For example identification of contaminated block by detecting rapid changes in total hemoglobin

concentration in time domain has been reported [82, 83]. This is based on the general assumption that hemodynamic changes are slow and any fast change in the signal is caused by motion. Even though this method is not uncommon in NIRS studies, simulation studies suggest that this approach has no significant improvement in recovering HRF compared to no correction for artifacts [74].

The last approach is using signal processing methods to identify and remove/reduce the effect of motion artifacts from previously recorded NIRS data. In other words, one uses the temporal or spectral features of the artifacts to identify them. A number of methods have been suggested in the literature based on this approach. Cui et al. suggested using the negative correlation between HbO_2 and HHb to detect motion artifacts [67]. Normally, the HbO_2 and HHb changes, especially during hemodynamic response to stimulation, are in opposite directions. In general, the changes of the two are not highly correlated. Therefore, if a highly correlated change between the two species is detected, it can be attributed to the motion.

Scholkmann et al. used a moving standard deviation scheme to detect motion artifacts and applied spline interpolation in the time interval of the motion to model the artifact and subtract it from the signal [66]. This method was reported to work well for several types of motion artifacts, however, parameters of the method need to be properly adjusted for the type of motion artifact to be removed.

This approach has also been employed for reduction of global interferences from fNIRS data. For example, Zhang et al. used eigenvector based spatial filtering to remove global interferences from NIRS signal to improve HRF detection [64]. In this method, global interferences are assumed to be responsible for the baseline period variations. Using the baseline information as a reference, the stimulation period data is processed such that the effect of global interference is minimized.

Application of Wiener filtering has also been suggested to reduce the effect of motion artifacts [76]. This method requires prior knowledge of the original fNIRS signal's power spectrum. Kalman filtering with appropriate model on noise and data has been applied to both fNIRS and PPG [65, 84]. Application of Kalman filtering requires prior assumption on distribution of noise which models the artifacts.

Wavelet decomposition is another promising approach for detection and removal of interferences from fNIRS signal. Continuous Wavelet transform for ex-

ample, has been used to detect blocks contaminated with motion artifacts using a hard threshold on the wavelet transform amplitudes [85]. The scales at which this thresholding occurs were identified through Monte Carlo simulation on a training data set. Robertson et al. proposed a method based on the DWT along with reference channels for source and detector optodes [63]. The wavelet coefficients were shrunk only if they exceeded a threshold in the data channel as well as the reference channels. Wavelet transform has also been applied for removal of global interferences in fNIRS signal [86].

A detailed review and comparison of some of these methods can be found in [74] and [75].

2.2 NIRS in Urology

The evolution of the NIRS as a means of monitoring the hemodynamics and oxygenation of the bladder is recent [87]. Important information can be derived with NIRS that contribute to the evaluation of patients with symptoms of bladder dysfunction, and understanding is growing of the distinct patterns of change in chromophore concentrations that occur in the context of disease. Wireless NIRS devices have been utilized to evaluate bladder function in health and disease [87, 88], and NIRS is proving to be uniquely applicable to the study of bladder pathophysiology because of the anatomic and vascular characteristics of the organ, how the bladder's microcirculation must function to maintain perfusion as it fills and contracts to empty, and because of the negative effect of disorders of detrusor muscle hemodynamics and oxygenation on normal voiding function [89].

The earliest clinical application of NIRS in urology was reported by Stothers et al. [27]. They observed that patterns of change in HbO₂ and HHb are different in health and disease during bladder contraction and concluded that abnormalities in detrusor muscle hemodynamics may be related to symptoms of voiding dysfunction.

This method was evaluated by other researchers and urologists. In a study by Yurt et al., NIRS performance in classifying male subjects with Lower Urinary Tract Symptoms (LUTS) as bladder outlet obstructed or unobstructed was compared with the gold standard uroflowmetry and urodynamic Pressure Flow

Study (PFS) [90]. The NIRS method correctly identified 25 out of 29 obstructed patients and 21 out of 24 unobstructed cases resulting in a sensitivity of 86.2% and specificity of 87.5%.

Amelink et al. studied the application of NIRS for in vivo monitoring of bladder wall microvascular blood oxygen saturation [91]. Deterioration of bladder microvasculature has been recognized as a cause of continuing bladder function loss and NIRS can be used as a tool to measure the oxygenation of the bladder wall to differentiate between bladders with loss of function and normal ones. In this case however, the NIRS probe needs to be placed in the working channel of a standard cystoscope [91]

Detrusor muscle oxygenation has also been monitored using NIRS during detrusor overactivity contractions [92]. In their study, Vijaya et al. examined 55 women with a mean age of 52 years. During involuntary contractions in the 23 subjects with detrusor overactivity, they observed a statistically significant increase in HHb at maximum detrusor pressure from the baseline [92] while no change was observed for voluntary detrusor contraction.

One bladder-related symptom of concern not addressed by current NIRS monitoring studies is the inability to sense when the bladder is full. This symptom occurs in a number of conditions and for affected patients the problems that result range from accidental leakage of urine by day (incontinence) or bed wetting at night (enuresis), through to an inability to empty the bladder (urinary retention). While incontinence and enuresis are troublesome, can be embarrassing, and negatively affect a patient's quality of life [93], urinary retention has potentially serious consequences, particularly in patients with abnormal bladder function secondary to spinal cord injury. In such cases, not being aware that the bladder is full can lead to back pressure developing in the urinary tract that risks serious damage to the kidneys. Unrecognized, this situation increases morbidity and contributes to a shortened life expectancy.

Monitoring bladder size, volume, and content non-invasively can be done using ultrasonic scanning, and is common in clinical practice. This technique uses ultrasonic imaging to differentiate the urinary bladder from surrounding tissues and organs, produce volume information, and estimate urine level. The method gives accurate results, but does not lend itself to monitoring in ambulant subjects or home

use as it requires powerful computational resources and a complex scanning control system. The requirements of gel application and control measurement also make most commercial ultrasonic scanners inappropriate for continuous wearable monitoring, although some portable and wearable ultrasonic sensors for bladder monitoring have been reported [68, 94].

Bioelectrical impedance analysis is another method proposed for determining the volume of urine in the bladder. This technique is principally used for determining extracellular and total body water, and several skin surface electrodes are required on the abdomen at the level of the bladder for the changes in electrical impedance used for detection of urine volume to be measured [95].

2.3 Functional Brain Connectivity Using fNIRS

The interaction between different cortical areas is responsible for coordination of complex tasks. Studying this cortical connectivity helps in achieving a better understanding and insight of the human's brain architecture and can potentially help in diagnosing certain diseases and conditions affecting the brain connectivity.

Cortical connectivity can be divided into two main categories. Functional connectivity is defined as temporal correlations between spatially remote neurophysiological events [96]. In functional connectivity, some measure of statistical interdependence is used as a measure of connectivity. Effective connectivity on the other hand, involves identifying causal influences between cortical regions. In other words, it shows how the information flows between different cortical areas. Cortical connectivity analysis is a recent subject of interest in functional imaging which studies how the activated cortical networks interconnect and coordinate to perform a particular sensorimotor/cognitive task.

Functional connections between cortical regions can reveal networks consisting of functionally connected cortical regions which are involved in task specific activities. In some situations, task based neuroimaging may not be an appropriate diagnostic tool as the subjects may be unable to perform a task at all [97]. Connectivity mapping can be beneficial in such circumstances. Functional connectivity using fNIRS is specially important and relevant in cases where subjects can not be transferred to scanner devices. Examples are patients in intensive care units or

mental/language development studies in infants. fNIRS provides a good substitute for fMRI based connectivity mapping and allows researchers or clinicians to perform same studies as the ones with fMRI on subjects with limited mobility.

Functional connectivity has been a subject of study in Electroencephalography (EEG) [98], fMRI [99] and more recently in fNIRS [97, 100] and different methods have been proposed for analyzing it. Cross correlation and cross coherence are two widely used methods for detecting functional connectivity in fMRI [101, 102]. In these methods a seed region is selected and the cross correlation/coherence is calculated between the seed region and time course from all other brain areas. To determine the direction of influence, Directed Coherence (DC) method has been proposed [103]. It decomposes coherence into components that represent feedforward and feedback components of the interaction between two time series. Partial directed coherence and directed transfer function are also proposed for neural structure determination [104]. In practice, these methods rely on modeling the signal with an MVAR model.

Another measure for analyzing cortical connectivity is the mutual information between signals from different brain areas [105]. This method has the advantage that it is model free and is thus not limited to linear models.

In functional neuroimaging methods such as fMRI and fNIRS, one could examine the task-specific functional connectivity which studies how connections differ in response to a task. Sun et al. for example, used coherence and partial coherence to evaluate task-specific connectivity in subjects performing two different tasks where one of the tasks required more bimanual coordination [102]. Their results showed that even though there was no significant difference in mean activity between the two tasks, there was an increase in interhemispheric connectivity between primary motor (M1) and Premotor area (PM) for the bimanual task which required higher degree of coordination.

A different type of connectivity from task-specific connectivity is the RSFC. RSFC is based on the synchronization between spatially remote and different cortical areas at rest which is an indication of functional connection between different brain networks. It was first demonstrated by Biswal et al. using BOLD-fMRI by detecting low frequency oscillations in the motor cortex at rest [101].

White et al. originally used fNIRS based RSFC analysis in five subjects to

demonstrate the feasibility of using fNIRS as an alternative to fMRI for this type of connectivity analysis [97]. Through simultaneous imaging over motor and visual cortices, they were able to derive robust correlation maps which were in agreement with expected functional neural architecture.

fNIRS based connectivity has since been employed to study RSFC in different brain networks. In a study by Zhang et al., 30 young adults were studied in a resting state followed by localizer task measurement [106]. The localizer task was used to identify the seed channel for connectivity analysis. Using the Generalized Linear Model (GLM) with seed channel as the independent variable, they showed a significant RSFC between left inferior frontal cortex and superior temporal regions which are associated with language.

Lu et al. investigated a similar approach to study sensorimotor and auditory cortices [107]. They studied 29 adult subjects and computed the RSFC using seed based correlation analysis and showed that the resulting networks were consistent with previous fMRI findings.

Duan et al. compared the results of RSFC with fNIRS using correlation with seed Regions Of Interest (ROI) with those obtained from fMRI to evaluate validity of fNIRS based RSFC [108]. They used simultaneous fNIRS-fMRI data from 21 subjects in resting state. There was high similarity in connectivity between the bilateral primary motor ROI using the two methods, specially for HbO₂ and BOLD for all subjects. Also, group level sensorimotor connectivity maps showed similarity between the two methods and this similarity in group level was higher than in individual level.

2.4 NIRS for Monitoring TMS

As described in Chapter 1, TMS is the method of magnetically stimulating the brain. This method has found clinical and research applications such as treatment of psychiatric diseases and stroke rehabilitation. Using neuroimaging techniques, one can directly monitor the effect of the stimulation on brain activity and the interaction among brain regions. The strong electromagnetic pulse produced by the TMS coil strongly interferes with other sensitive electronic devices in the vicinity of the coil. This introduces a severe problem for other monitoring devices such

as EEG or Magnetoencephalography (MEG). Such modalities rely on very small electric activities for their performance which are swamped by the induced currents from TMS pulse. Optical methods such as NIRS, however, are based on the changes in parameters of diffusive light and therefore are not affected by the TMS electromagnetic pulse. Thus, NIRS seems to be an appropriate choice for studying the effects of TMS on human brain. The short penetration depth of the NIRS in this case seems to match the focal depth of the TMS coil which normally does not exceed 3-4cm.

In simultaneous NIRS-TMS studies, the changes in cortical hemodynamics either at the location targeted by TMS pulses or in other areas of the brain are monitored during or after the stimulation. Hada et al. used a two channel device beneath the stimulation coil during a repetitive TMS recording [109]. They observed decrements in tHb and HbO₂ concentrations and increment of HHb during and after repetitive Transcranial Magnetic Stimulation (rTMS) at different stimulation rates and intensities. They also observed that concentration changes continued for up to 10s after stimulation.

Hanaoka et al. investigated the effects of low frequency rTMS over the right frontal lobe on the function of the left frontal lobe by NIRS [110]. They observed significant changes on hemodynamics during the poststimulation baseline period which was interpreted as demonstrating the activation and deactivation of the left frontal cortex during and after rTMS of the right frontal cortex.

In a similar study, Mochizuki et al. studied interhemispheric interactions between bilateral motor and sensory cortices using NIRS and rTMS [111]. They recorded hemoglobin concentration changes at the right prefrontal cortex, PM, primary hand motor area (M1) and primary sensory area (S1) during and after stimulation over the left PM, M1, and S1. They also recorded Motor Evoked Potential (MEP) to TMS over the right M1 from the left first dorsal interosseous muscle after the conditioning TMS over left S1. They reported that TMS over PM induced a significant HbO₂ decrease at the contralateral PM and stimulation over M1 elicited a significant HbO₂ decrease at the contralateral S1, and TMS over S1 significant HbO₂ decreases at the contralateral M1 and S1. They suggested that all these indicate a mainly inhibitory interaction between bilateral PMs and bilateral sensorimotor cortices in humans.

Mochizuki et al. also used NIRS recordings in a separate study along with TMS in 4 different conditions (3 intensities and sham stimulation) and similar to other cases, detected significant changes in HbO₂ and HHb in all intensities [112]. They suggested that the increase of HbO₂ concentration at 100% Active Motor Threshold (AMT) under the active condition reflects an add-on effect by TMS to the active baseline and that the decrease of HHb and tHb concentrations at 120 and 140% AMT under the resting condition are due to reduced baseline firings of the corticospinal tract neurons induced by a lasting inhibition provoked by a higher intensity TMS [112].

Eschweiler et al. utilized NIRS with rTMS on the left dorsolateral prefrontal cortex of patients suffering from major depression [113]. They observed that absence of a task-related increase of total hemoglobin concentration at the stimulation site before the first active rTMS significantly predicted the clinical response to active rTMS [113]. They reported that clinical benefits of rTMS are predicted by low local hemodynamic responses and support the idea of activation-dependent targeting of rTMS location.

Chiang et al. have also followed similar procedure to investigate the effect of TMS using NIRS [114]. However, they mostly concentrated on finding out how long the TMS effect lasts. More specifically, the aim of their study was to measure the change of HbO₂ and HHb levels in the left motor cortex after 20 min of 1 Hz TMS over the right motor cortex. Subjects carried out a finger to thumb tapping task sequentially with six blocks of ten cycles (30 s on and 60 s off). One block was performed before TMS and five after TMS. The results showed that the level of HbO₂ in the unstimulated cortex increased after TMS over the contralateral hemisphere and that the increase lasted 40 min after 1 Hz stimulation. HHb was slightly decreased during the first 15 min after stimulation.

2.5 Summary and Conclusion

Artifact removal is a crucial pre-processing step for almost any NIRS application due to the high sensitivity of this method to motion. When a NIRS based sensor is used for continuous monitoring, the issue of motion artifacts becomes a more serious problem. This specifically applies to NIRS instruments for continuous moni-

toring of the bladder function which need to be worn by the subject at all times and are hence affected by the subject's day to day activities.

The problem of motion artifacts is not unique to wearable NIRS systems. When NIRS is used for monitoring brain function, which is one of the most appealing applications of this technology, motion artifacts can appear from a number of different sources. In monitoring the effect of TMS for example, which is a recent area of interest [115, 116], several mechanisms can result in motion artifacts. In particular, the TMS pulse can result in activation of superficial scalp muscles which can potentially cause motion artifacts in the NIRS signal [117]. Additionally, the motion and vibrations resulting from TMS coil activation can result in slight shifts in optodes location which is reflected in the signal [73, 117]. In addition to these sources, the head movements, specially in longer stimulation sessions can contribute to motion artifacts. This highlights the importance and necessity of developing proper artifact removal methods for use in combined TMS-NIRS studies.

Cortical connectivity analysis, another potential field of application of NIRS, is also susceptible to motion artifacts. Many of the connectivity analysis methods rely on similarities and relations between signals in spatially remote channels to detect connectivity [106, 107]. Spontaneous movements of the subject, which is a common issue specially in infants and young children, results in highly correlated changes across all or a large number of channels that can influence the measured connectivity. Being able to identify motion corrupted data segments allows the removal or treatment of these data blocks to avoid detection of false connectivity [108].

The advantages of NIRS over other neuroimaging methods has lead to a great interest in its use for monitoring and studying brain function. One area of interest for fNIRS in brain functional study is the influence of electrical and magnetic stimulation on brain hemodynamics. In particular, the intrinsic advantages of NIRS make it a desirable choice for use with TMS. The most common approach is to study the effect of TMS on the hemodynamics of the target area or the areas closely related to it. However, one interesting question is how TMS affects and modulates the brain networks. This can be investigated either with concurrent TMS-NIRS or in an "offline" approach [118] where the lasting effect of TMS on a particular cortical network is investigated. RSFC using fNIRS provides a useful tool for mon-

itoring this effect in a non-expensive and easy to use manner. Moreover, with the availability of a NIRS instrument capable of measuring the fast optical signal, one can also look at the network changes in a concurrent TMS-NIRS study and evaluate more "elastic" changes that occur in a shorter time scale and require instruments with higher temporal resolution and sensitivity to measure [73].

In summary, development of a motion artifact reduction methods as a required pre-processing step was the initial focus of this thesis which forms a signal processing basis for the rest of the thesis. Development of a new approach for analyzing resting state functional connectivity for potential use in infants as well as in TMS studies and in particular for stroke patients to investigate the changes in cortical networks was the next major area of interest. In order to look at short time scale changes in connectivity, a custom made NIRS device was developed and tested. Finally, a new NIRS based wearable bladder monitoring sensor was developed which is an example of a device that can significantly benefit from the artifact removal methods due to the inherent problem of motion as a result of constant wearing by the subject for bladder monitoring.

Chapter 3

Wavelet Based Motion Artifact Removal for Functional Near Infrared Spectroscopy

NIRS has found usage in a wide range of applications as a powerful tool for monitoring tissue hemodynamics. In particular, fNIRS as a subset of NIRS, has been a subject of interest for brain studies due to its non invasive, non restraining nature. However, for fNIRS to work well, it is important to reduce its sensitivity to motion artifacts. In this chapter, we introduce a new wavelet-based method for removing motion artifacts from fNIRS signals. Even though this method was originally designed and tested on brain fNIRS data, it can in general be applied to a wide range of NIRS data collected from different tissue types. The material presented in this chapter was published in the *proceedings of the international IEEE EMBS conference* in 2010 [2], *proceedings of SPIE* in 2011 [3] and the journal of *physiological measurement* [4]. The method presented here was independently compared with a number of other common methods of artifact removal using simulated and experimental data [74, 75]. This method has also been used in HOMER2 NIRS processing package¹, an open source MATLAB toolbox for analyzing fNIRS data developed by MGH-Martinos Center for Biomedical Imaging and widely used by

¹www.nmr.mgh.harvard.edu/optics

the fNIRS community.

3.1 Artifact Removal Using Discrete Wavelet Transform

A majority of motion artifacts appear in the form of abrupt changes in the amplitude of the signal. The DWT can provide good localization in time or frequency domain. Therefore, motion artifacts appear as isolated large coefficients in the discrete wavelet domain. This makes identification and removal of artifacts easier in the wavelet domain.

A signal $y(t)$ can be expanded using the DWT as

$$y(t) = \sum_k v_{j_0 k} \phi_{j_0 k}(t) + \sum_{j=j_0}^{\infty} \sum_k w_{jk} \psi_{jk}(t) \quad (3.1)$$

where $\phi_{jk}(t) = 2^{j/2} \phi(2^j t - k)$ is the scaling function and $\psi_{jk}(t) = 2^{j/2} \psi(2^j t - k)$ is the wavelet function [119]. j and k are the dilation and translation parameters respectively and j_0 is the coarsest scale in the decomposition. $v_{j_0 k}$ and w_{jk} are the approximation and detail coefficients and $\psi(t)$ and $\phi(t)$ are the mother wavelet and scaling functions, respectively.

We assume that the observed signal is composed of the physiological signal of interest, $f(t)$, plus an interference term, $\varepsilon(t)$

$$y(t) = f(t) + \varepsilon(t) \quad (3.2)$$

Using the Fast Wavelet Transform (FWT) algorithm [120], the wavelet transform of the observed signal can be written as

$$w_{jk} = \sum_l g(l - 2k) v_{j+1}(l) \quad j = j_0 \dots J - 1, k = 0 \dots 2^j - 1 \quad (3.3)$$

$$v_{jk} = \sum_l h(l - 2k) v_{j+1}(l) \quad (3.4)$$

where $g(n)$ and $h(n)$ are the wavelet filter bank highpass and lowpass filters respectively with $v_J(n) = y(n)$ and j_0 is the coarsest level [119]. $y(n)$ is the sampled version of $y(t)$ with $n = 0 \dots N - 1$ and $N = 2^J$. This can be written in matrix form

as

$$\mathbf{W} = W\mathbf{Y} \quad (3.5)$$

where $\mathbf{Y} = [y(0) \dots y(N-1)]^T$. $W = [W_{J-1} \ W_{J-2} \ \dots \ W_0 \ V_0]^T$ is the $N \times N$ DWT matrix and $\mathbf{W} = [\mathbf{W}_{J-1} \ \mathbf{W}_{J-2} \ \dots \ \mathbf{W}_0 \ \mathbf{V}_0]^T$ is the vector of wavelet coefficients [121]. \mathbf{W}_j is the vector of wavelet coefficients at level j i.e. $(\mathbf{W}_j)_k = w_{jk}$ and \mathbf{V}_0 is the scaling coefficient. $(\cdot)_k$ indicates the k th element in the vector. Writing Equation 3.2 in vector form and using discrete version of y , f and ε and applying the wavelet transform for one level we have

$$W_j\mathbf{Y} = W_j\mathbf{f} + W_j\varepsilon \quad (3.6)$$

which gives the relationship between wavelet coefficients of the observed signal, underlying physiological signal of interest and the noise term representing artifacts.

Distribution of wavelet coefficients can be described by a mixture of Gaussians [122, 123]. One Gaussian component describes coefficients centered around zero and one describes those spread out at larger values. Here we impose a single Gaussian distribution on wavelet coefficients. The hemodynamic signal is a smooth and slowly varying signal compared to motion artifacts. Therefore, most of wavelet coefficients of the fNIRS signal are spread around zero with smaller variance compared to motion artifact coefficients. Our model is similar to the one described by Antoniadis [122] with the assumption that only coefficients from normal distribution with smaller variance in the mixture model belong to original signal. Hence, the model is reduced to a single Gaussian distribution. The wavelet coefficients of the observed signal, $y(n)$, can be therefore written as

$$w_{jk} = \tilde{w}_{jk} + \varepsilon_{jk} \quad (3.7)$$

where $\tilde{w}_{jk} \sim N(0, \sigma^2)$. The mean of the distribution is zero because the wavelet coefficients w_{jk} are the outputs of a highpass filter. The ε_{jk} coefficients appear as a few large coefficients across the time course of each level. For any given coefficient, w_{jk} , if the probability of observing values larger than w_{jk} is less than

an arbitrary probability, α , we can conclude that the coefficient does not belong to the original signal and must have been due to artifacts and thus must be removed. This probability can be written as

$$p_{jk} = 2 \left(1 - \Phi \left(\frac{|w_{jk}|}{\hat{\sigma}} \right) \right) \quad (3.8)$$

where Φ is the Normal Cumulative Distribution Function (NCDF). We then propose to use the following thresholding scheme for the removal of the artifacts:

$$\hat{w}_{jk} = \begin{cases} w_{jk} & \text{if } p_{jk} > \alpha \\ 0 & \text{if } p_{jk} < \alpha \end{cases} \quad (3.9)$$

α is the probability threshold which can function as a tuning parameter. In this approach, we are basically treating artifacts as large outliers added to the desired coefficients $\tilde{w}_{jk} \sim N(0, \sigma^2)$. The parameter α indirectly determines how much the artifact power should be reduced. For the limiting case of $\alpha \rightarrow 0$, no thresholding is applied and the signal coefficients are left intact at level j .

The level selection for artifact removal is based on the degree of artifact contamination at each level which is defined as total number of coefficients exceeding threshold in that particular level. Define $\Psi = \{w_{jk} : p_{jk} < \alpha\}$ and $\eta_j = \sum_k \mathbf{I}_{\Psi}(w_{jk})$ where $\mathbf{I}_{\Psi}(x)$ is the indicator function. Then artifact removal is conducted in levels that fall in the 90th percentile of $\{\eta_j\}$.

The variance of the distribution of \tilde{w}_{jk} can be estimated using Median Absolute Deviation (MAD) [124]. MAD is a robust estimator of scale and is not sensitive to outliers. In our application, artifacts behave like outliers added to the original signal whose variance we would like to estimate. As a result, a limited number of artifacts does not cause a problem in estimating the variance of original signal coefficients, $W_j\mathbf{f}$. The estimate of standard deviation is related to MAD in each subband by [124]

$$\hat{\sigma}_j = \frac{\text{Median}(|\mathbf{W}_j|)}{0.6745} \quad (3.10)$$

where $\hat{\sigma}_j$ is the estimated standard deviation in scale j and \mathbf{W}_j is the set of wavelet transform coefficients in the same level.

Following thresholding, the signal can be reconstructed using

$$\hat{\mathbf{Y}} = \mathbf{W}^T \hat{\mathbf{W}} = [W_{J-1}^T, W_{J-2}^T \dots W_0^T, V_0^T] \begin{bmatrix} \hat{\mathbf{W}}_{J-1} \\ \hat{\mathbf{W}}_{J-2} \\ \vdots \\ \hat{\mathbf{W}}_0 \\ \hat{\mathbf{V}}_0 \end{bmatrix} \quad (3.11)$$

where $(\hat{\mathbf{W}}_j)_k = \hat{w}_{jk}$.

To avoid pseudo Gibbs phenomena near singularities or abrupt changes in the signal which is mostly attributed to the lack of shift invariance in traditional DWT, we performed artifact removal on all possible circularly shifted versions of the original signal and then undid the shifts and averaged the results [125]. This is known as Translation Invariant Wavelet Transform (TIWT) and will reduce the undesirable effects caused by shift-variance of DWT. This can be formally stated as

$$\tilde{y}(n) = \frac{1}{M} \sum_{h=1}^M S_{-h}(T(S_h(y(n)))) \quad (3.12)$$

where S_h is the shift operator and T is the operator representing DWT followed by artifact removal and M is the total number of shifts [125].

3.2 Simulation

We used simulated NIRS data for preliminary evaluation of this method. In simulation, we have access to the original artifact-free signal and can evaluate how well our method can reconstruct the original signal. This usually is not possible in experimental data as the artifact-free signal is not available. We first simulate the NIRS signal with an Autoregressive (AR) model of order 9 and then add the artifacts. It was observed that the AR model was sufficient to model the general behavior of a short duration fNIRS signal. The artifact was selected from an experimental fNIRS signal and superimposed on the simulated fNIRS signal. All simulations and Wavelet processings were performed in MATLAB (Mathworks,

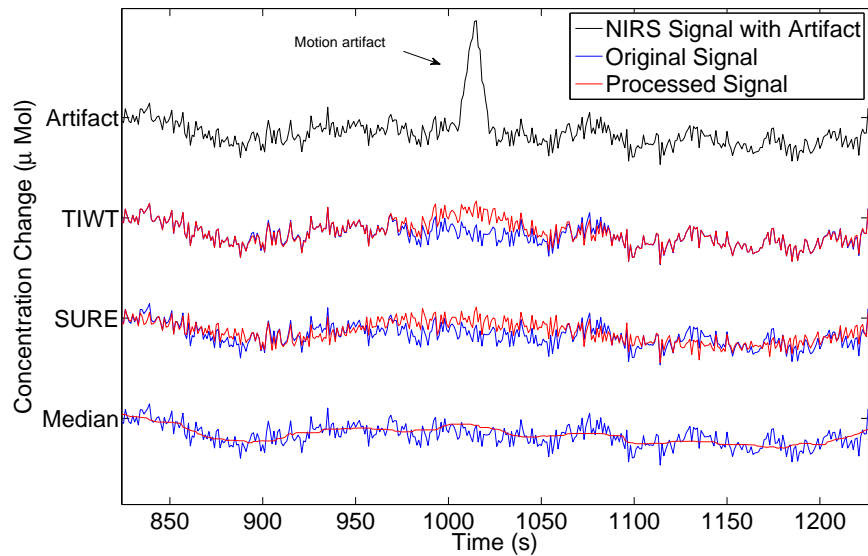


Figure 3.1: Comparison of methods: plots from the top show the simulated optical signal with artifact, the proposed method with TIWT, SURE threshold and Median filtering respectively. The original artifact-free signal is also shown for each method.

MA, USA) and using the Wavelab 850 toolbox ².

We evaluated the performance of our method using DWT and TIWT along with Median filtering and Stein’s Unbiased Risk Estimator (SURE) based wavelet denoising in removing the simulated artifact [126]. We wanted to verify if our method offers any significant improvement over regular wavelet denoising, therefore SURE based wavelet denoising is chosen for comparison. Median filtering is the procedure frequently used for removing impulsive noise from signals. The length of the median filter is selected to be twice the duration of the artifact to provide the best artifact suppression while having minimum filter length.

²www-stat.stanford.edu/wavelab

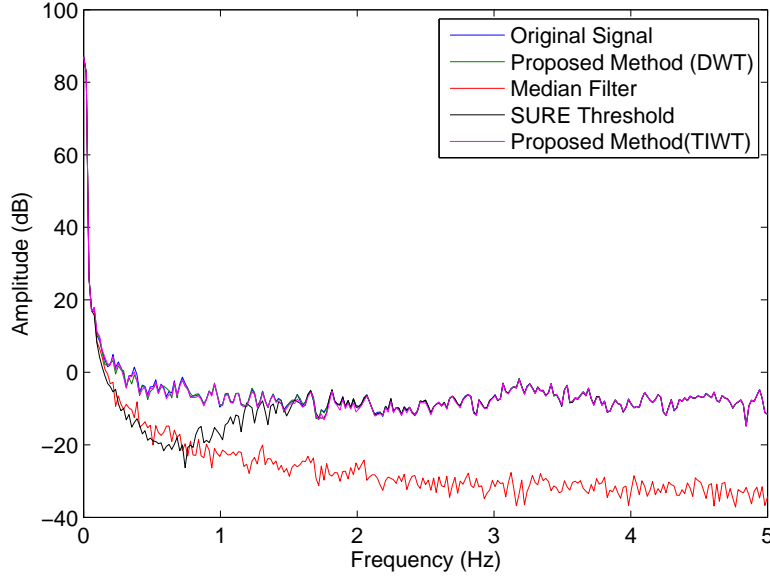


Figure 3.2: Comparison of the power spectrum of the original signal and the processed signal using 4 methods for a typical simulated fNIRS signal.

3.2.1 Performance Evaluation

We compared the methods using Normalized Mean Squared Error (NMSE). NMSE is defined as

$$NMSE_i = 10 \log_{10} \frac{\sum_{n=1}^N (y_i(n) - \tilde{y}_i(n))^2}{\sum_{n=1}^N y_i^2(n)} \quad (3.13)$$

where $y_i(n)$ is the original signal, $\tilde{y}_i(n)$ is the artifact removed signal and i is the channel index. In order to take into account the random effect of the fNIRS signal and the artifacts, we applied each artifact removal algorithm on 100 realizations of the AR signal with artifact and averaged the performance of each method. Parameter α is set to 0.05 for an average artifact removal.

We also use Magnitude Squared Coherence (MSC) as an additional measure which is defined as

$$MSC_{y\tilde{y}}(f) = \frac{|P_{y\tilde{y}}(f)|^2}{P_{\tilde{y}\tilde{y}}(f)P_{yy}(f)} \quad (3.14)$$

where $P_{y\tilde{y}}(f)$ is the cross power spectrum of signals \tilde{y} and y , and $P_{\tilde{y}\tilde{y}}(f)$ and $P_{yy}(f)$ are the power spectrum densities of \tilde{y} and y as a function of frequency, respectively.

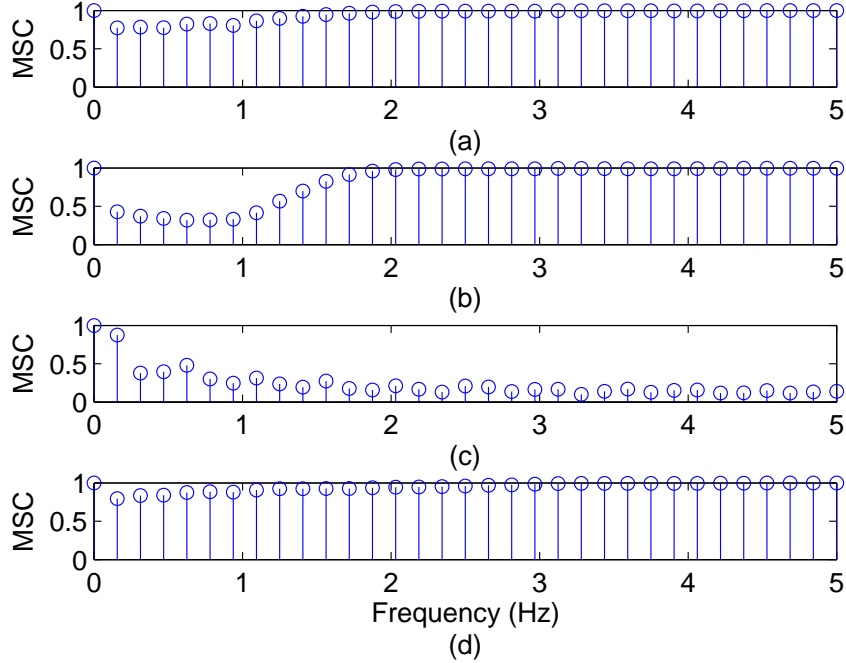


Figure 3.3: Coherence between original signal and a) output of our method with DWT, b) SURE method, c) Median filtering and d) our method with TIWT

The coherence has a value between 0 and 1 and measures how much \tilde{y} corresponds to y at each frequency. In other words, it indicates how well the signals spectra are matched in each frequency band. The frequency bands selected for analysis are 0.15 Hz wide. The power spectrum densities are calculated in each window and then the window is shifted towards the next band. There is a 50% overlap between adjacent windows. The results are averaged over 100 trials.

3.2.2 Results

The results of NMSE analysis for simulated fNIRS are summarized in table 3.1. Lower NMSE in the table indicates higher similarity to the original artifact-free signal and hence, better performance in artifact removal. We used two sample t-test to verify if the differences in the table are significant. The data is tested for

Table 3.1: Normalized Mean Squared Error between processed signal and original artifact-free signal

| Method | Median Filter | SURE Threshold | DWT | TIWT |
|-------------------------|---------------|----------------|-------|--------|
| Average NMSE (dB) | -8.95 | -8.71 | -9.97 | -10.98 |
| Standard Deviation (dB) | 1.36 | 1.65 | 2.38 | 1.97 |

normality prior to the test. The difference between TIWT and other methods is statistically significant ($p < 0.01$). The difference between DWT and SURE is also significant ($p < 0.05$), however, difference between DWT and median filter is not significant. Visual comparison of the results for median filter and DWT reveals that DWT better preserves the shape of the signal in regions away from artifact. Fig. 3.1 demonstrates the result of applying median filter, wavelet SURE denoising, and the proposed method using TIWT to a sample of simulated fNIRS signal.

Fig. 3.2 shows the power spectrum of the signals in Fig. 3.1. The figure suggests that median filtering significantly alters the power spectrum of the signal, while the 3 wavelet based methods selectively reduce the power in frequency ranges where the energy of artifact is mostly concentrated. The results of MSC are shown in Fig. 3.3. The figure shows high coherency between the original signal and the artifact removed signal using our method with DWT and TIWT. It is evident that the coherency for median filtering results is very low for higher frequencies which is due to smoothing effect of Median filter.

3.3 Experiment

fNIRS is widely used in infant studies as the small skull size leads to a larger volume being investigated by fNIRS and also because other functional imaging methods may not be readily applicable to infants. Functional studies in infants have many applications in areas such as brain development in infants [127], speech perception [83], premature infant studies [128] and cognitive studies [82]. However, motion artifact is a serious problem in infant fNIRS studies as the subjects may move spontaneously.

To evaluate the performance of the method, we applied it to fNIRS data col-

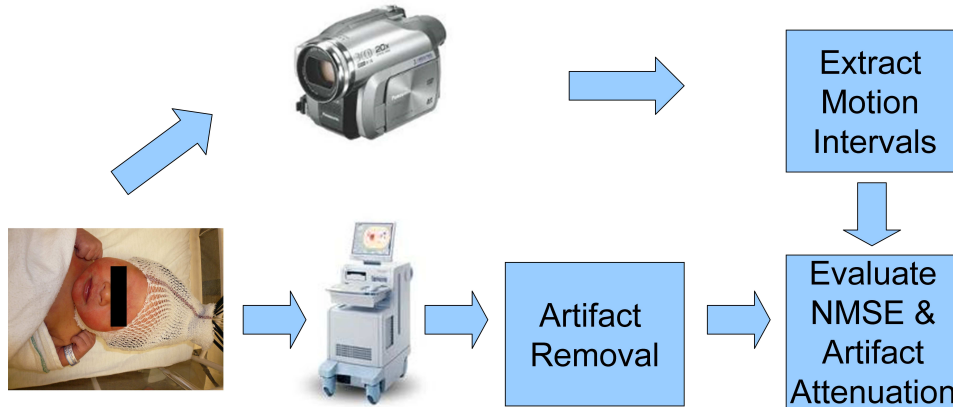


Figure 3.4: Experiment setup

lected from 3 infants (two 1 day old and one 2 day old infants, 1 male). The experiment was approved by the University of British Columbia board of ethics and consent form was signed by the infants' parents. A 24 channel ETG-4000 fNIRS device (Hitachi Medical Corporation, Tokyo, Japan) with 700nm and 830nm lasers and sampling rate of 10Hz was used for data collection. Artifact removal was performed on raw optical density data. Motion artifacts are a form of interference in optical signal rather than a physiological interference. We attempt to remove them in the optical attenuation signal to avoid using artifact contaminated data in calculation of HbO_2 and HHb .

During the study, fNIRS optodes placed on left and right temporal regions were fixed by a gauze bandage. Optode placement is shown in Figure 3.5. The total duration of the processed fNIRS recording was 819.2 seconds and the first 20 channels from each subject were included in the analysis. The infants were videotaped during the experiment to determine the time instant of movements. The video signal was then processed using Sum of Absolute Differences (SAD) between each 2 consecutive frames to acquire a reference signal from which motion intervals were extracted for evaluation purposes [129].

A total of 29 motion events were recorded for 3 subjects (16, 7 and 6 for subjects 1 to 3). Motion artifacts that take place at different time instants are independent and may have different shape, duration or amplitude. Therefore, overall

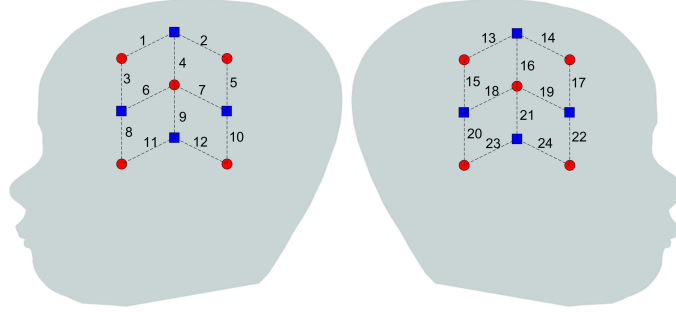


Figure 3.5: Optodes placement. The red circles and blue squares indicate the source lasers and detectors, respectively. The numbers between the dots indicate channel numbers.

artifact attenuation was calculated for the entire set of motion events. The value of artifact attenuation for each artifact is the median of attenuation across all channels.

3.3.1 Performance Evaluation

We used artifact power attenuation and NMSE as criteria to evaluate the performance of our method. Artifact power attenuation is defined as

$$\delta_m^i = 10 \log_{10} \frac{\sum_{n \in A_m} [y_i^{HP}(n)]^2}{\sum_{n \in A_m} [\tilde{y}_i^{HP}(n)]^2} \quad (3.15)$$

where A_m is the artifact time interval for the m th artifact in channel i and $y_i(n)$ is the original signal and is highpass filtered to yield $y_i^{HP}(n)$. $\tilde{y}_i^{HP}(n)$ is the highpass filtered version of the processed signal. The purpose of highpass filtering is to remove the effect of low-frequency physiological variations to ensure the calculated energies only reflect the energy of the artifact and not that of the physiological signal. This measure is basically the ratio of artifact energy before and after removal in dB. The artifact interval is identified using the video reference signal and is selected such that it begins at the time instant the reference signal deviates from baseline and ends when it reaches the baseline following the perturbations caused by motion. The baseline is assumed to be the stable signal level before and after artifact.

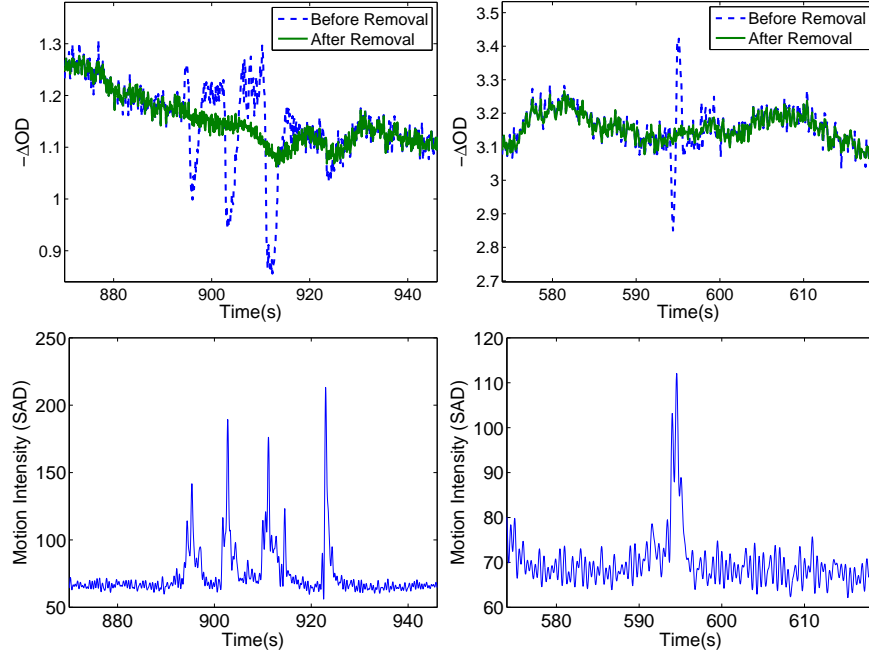


Figure 3.6: Two typical motion artifacts and results of applying the proposed method (top) with the motion reference signal extracted from videotape (bottom).

NMSE is defined as

$$NMSE_i = 10 \log_{10} \frac{\sum_{n \notin A_m} [y_i(n) - \tilde{y}_i(n)]^2}{\sum_{n \notin A_m} [y_i(n) - \bar{y}_i]^2} \quad (3.16)$$

where i is the channel index and \bar{y}_i is the mean value of $y_i(n)$. The NMSE is calculated for the artifact-free segments of each channel. NMSE shows how much distortion has been introduced and complements the first criterion, which indicates how much of the artifact power has been removed.

3.3.2 Results

To evaluate the performance of the method, we first applied it to an artifact-free fNIRS signal of length 512 samples (corresponding to 51.2 seconds) in the absence of motion artifacts which resulted in an NMSE of -13.80 dB, -17.54 dB and

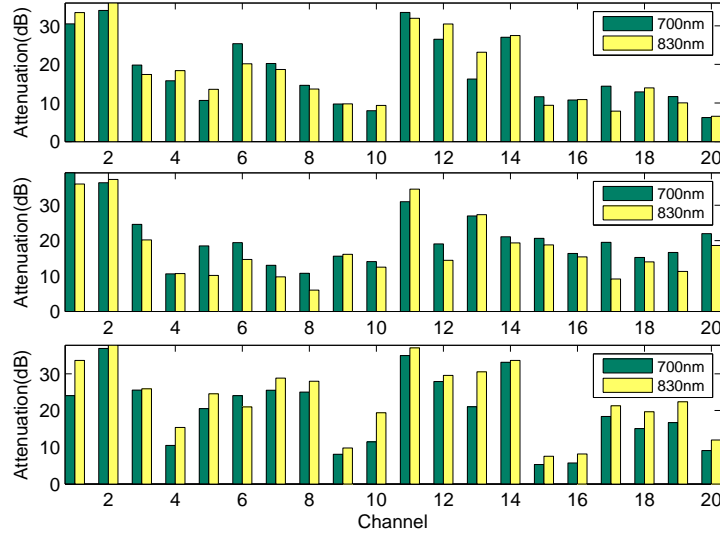


Figure 3.7: Artifact attenuation in 20 channels for 2 wavelengths for subjects 1 to 3 (top to bottom).

-14.84 dB for 3 subjects, respectively. We used Daubechies 5 (db5) wavelet for all experiments and the value of α was set to 0.1. This is equivalent to treating coefficients whose probability of belonging to hemodynamic signal is less than %10 as artifacts. Next, we evaluate the performance of the method in presence of motion artifacts. Figure 3.6 shows two typical head motion artifacts in the fNIRS signal, one in the form of a short abrupt impulsive noise and one in the form of a series of slower variations in the signal and the filtered signal along with the motion reference signal. The median of δ_m^i and $NMSE_i$ across all channels for each subject and for the 2 wavelengths are presented in Table 3.2. We consider the error to be acceptable if it is within 5% of the signal's energy which translates to less than -13dB in NMSE. The value of the NMSE in the table is calculated by excluding the first and last 300 samples in each channel in calculating Equation 3.16. This is to ensure the error represented in NMSE does not include errors due to edge effect. Different channels in our fNIRS setup are affected differently by motion and therefore, the artifact attenuation is not the same for all channels. This is shown in Figure 3.7 where the performance of the method in terms of artifact attenuation across different channels is shown for 2 wavelengths. The artifact attenuation

Table 3.2: Median of NMSE and Attenuation in artifacts energy (in dB) for proposed method

| | Subject 1 | | Subject 2 | | Subject 3 | |
|-------------|-----------|--------|-----------|--------|-----------|--------|
| | 700nm | 830nm | 700nm | 830nm | 700nm | 830nm |
| NMSE | -20.84 | -21.23 | -16.70 | -16.97 | -18.05 | -17.62 |
| Attenuation | 15.65 | 15.40 | 18.77 | 15.03 | 18.66 | 22.81 |

ranges from 7.3 dB to 37.3 dB in subject 1, 6.0 dB to 39.2 dB for subject 2 and 3.48 dB to 41.28 dB for subject 3 for both wavelengths combined. The median of overall artifact attenuation over the total of 29 motion events is 18.29 dB and 16.42 for 700nm and 830 nm channels.

As a comparison with regular wavelet denoising, we applied adaptive wavelet denoising based on SURE (Stein’s Unbiased Risk Estimator) risk to the same test data [126]. We chose wavelet denoising levels in such a way that similarity between processed and original signal is the same for SURE based denoising and our method. We then compare the artifact attenuation. The comparison is made across all artifacts for the three subjects. The intensity and duration of each artifact is different and it is fair to assume that the results of attenuation for each artifact is independent of other artifacts for the same subject. In this way, the performance of 2 methods on 29 different artifacts are compared.

We chose the following metric for the similarity of the original and processed signal [130]:

$$d(f_1, f_2) = \sqrt{\int_{-\pi}^{\pi} \left(\log \frac{f_1(\theta)}{f_2(\theta)} \right)^2 \frac{d\theta}{2\pi} - \left(\int_{-\pi}^{\pi} \log \frac{f_1(\theta)}{f_2(\theta)} \frac{d\theta}{2\pi} \right)^2} \quad (3.17)$$

This metric indicates how far apart the power spectra of 2 signals are. We evaluated the similarity in every artifact-free segment of original and processed signal for the two methods and averaged across each subject to derive 1 value for each subject.

Two typical artifacts were chosen to qualitatively demonstrate the difference between proposed method and regular wavelet denoising as shown in Figure 3.8. The top two right panels show a case in which both proposed method and wavelet shrinkage perform equally well in removing the artifact. The top two left panels

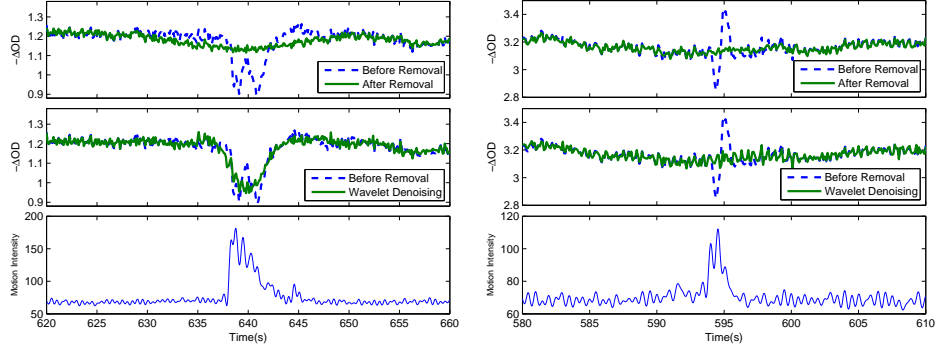


Figure 3.8: Comparison of proposed method with wavelet denoising for 2 typical motion artifacts. Top 2 panels show the artifacts and results of applying proposed method. Middle panels show the results of wavelet denoising and the bottom panels are the motion reference signals extracted from videotape.

show the case where wavelet denoising is not capable of detecting and removing the artifact while the proposed method has been able to attenuate the artifact. This is shown quantitatively in Figure 3.9. The attenuation is significantly different for the 2 methods (2 sample t-test $p < 0.01$). The results suggest that the proposed technique yields higher artifact attenuation for a given level of distortion in the signal.

The effect of varying α from 0.01 to 0.15 on NMSE and artifact power attenuation for 3 subjects is shown in Figure 3.10. α can be used as a tuning parameter to achieve desired artifact attenuation in trade off with signal distortion. The performance of the method is not the same for all subjects with similar α . However, changing α has the same effect on all subjects.

3.4 Discussion and Conclusion

In this chapter, we proposed a method for reducing motion artifacts in fNIRS signals using the discrete wavelet transform. The method is based on the assumption that motion artifacts have different characteristics in terms of amplitude and duration from the original signal. This difference is better highlighted in wavelet domain due to the good localization property of the DWT.

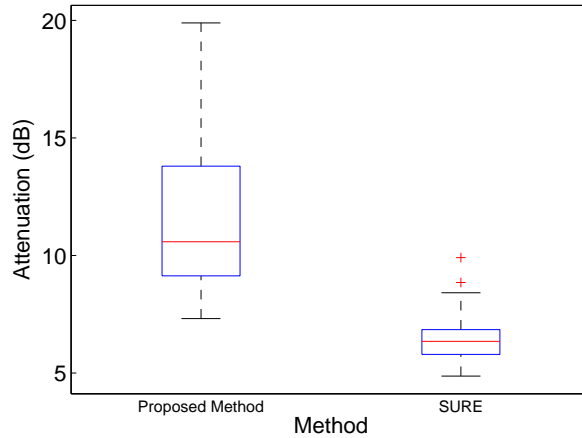


Figure 3.9: Comparison of proposed method with adaptive wavelet denoising method (SURE based)

To estimate the fNIRS signal coefficient’s distribution with the proposed method, the entire time span of the signal should be available. Therefore, our method in its current form is not suitable for real time processing. A possible workaround for online processing is to estimate the variance based on available data and update the estimate as more data becomes available. The effectiveness of this motion artifact removal method on improving accuracy of fNIRS activation maps is yet to be examined.

Artifact reduction can potentially distort the signal. It is important to be able to control the level of signal distortion in practical applications. The value of the parameter α in the proposed method can be set by the user to control NMSE in trade off with the intensity of artifact attenuation to reach a balance between NMSE and artifact attenuation.

Evaluation of a motion artifact reduction method requires knowledge of motion event times. Use of deliberate artifacts [76] or human observers [85] has been proposed for this purpose. Our method of extracting motion reference signal from video signal provides a non-subjective measure of motion for further evaluation of the artifact attenuation method.

The capability of the method to reduce the artifacts in a clinical data set was

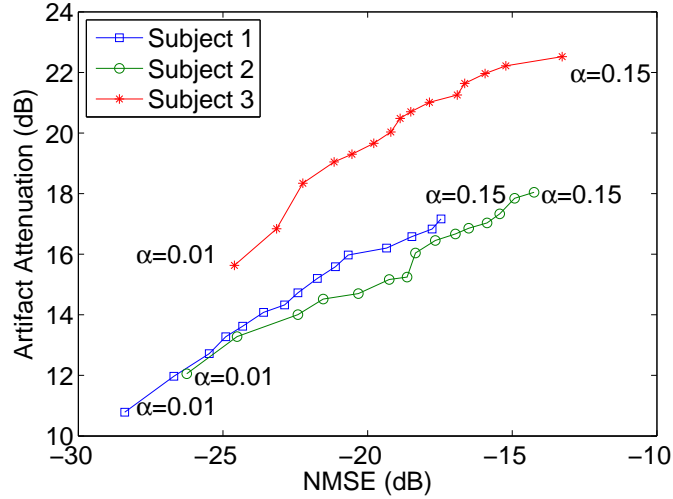


Figure 3.10: Artifact power attenuation versus NMSE for 3 subjects

demonstrated. The method was also compared with regular wavelet denoising and it was shown that for a given level of distortion, the proposed method yields higher artifact attenuation.

Our method was based on an additive model for interference caused by motion. Assumption of additive noise model for motion artifact is not uncommon in the literature. The Kalman filtering method used by Lee and Izzetoglu models motion artifact as additive observation noise [65, 84]. Some methods based on adaptive filtering are also based on the assumption that motion artifact noise is additive and can therefore be removed by subtracting the estimated noise from the signal [63, 76].

The attenuation in artifact power achieved by this method may change from one subject to another due to differences in total number of motion events and their intensity. This has also been reported in the form of variability in Signal to Noise Ratio (SNR) across subjects in earlier works [63, 76]. There is also variability in artifact attenuation in different channels. This can be explained by noting that due to the nature of the method, stronger artifacts are better isolated by wavelet transform and also can be better separated from the background fNIRS signal. Therefore, this method works best for spike-like artifacts and artifacts with significantly larger amplitudes and shorter duration compared to physiological changes in the

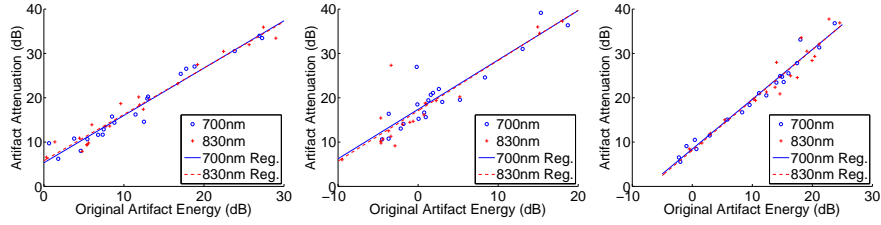


Figure 3.11: Correlation between original artifact intensity and artifact attenuation in different channels for 3 subjects.

fNIRS signal. This can explain the variability of artifact attenuation in Figure 3.7. Channels 1 and 2 for example, are located on the edge of the chevron shape optode holder and are more likely to lose contact with the tissue due to head's motion and therefore yield higher attenuation in all subjects. Figure 3.11 shows the plots of artifact attenuation versus original artifact energy for all channels in 3 test subjects. Original artifact energy was normalized to the energy in a reference segment of the signal. The reference segment for each subject was manually selected such that it represents the baseline state of the signal. There is a significant correlation between artifact attenuation and original artifact energy ($R^2=0.9584$ and $R^2=0.9636$ for 700nm and 830nm channels in subject 1, $R^2=0.8337$ and $R^2=0.8327$ for 700nm and 830nm channels in subject 2 and $R^2=0.9741$ and $R^2=0.9380$ Subject 3). This confirms that original artifact energy explains the variability in artifact attenuation.

Despite the fact that this method is designed and works best for spike-like artifacts, it has been shown that the method could work well on more subtle types of artifacts as well and in particular that it can be effective in reducing motion artifacts that are correlated with the evoked cerebral response [75].

The differences between our method and two other wavelet based methods for NIRS motion artifact removal should be emphasized here. Sato et al [85] used a continuous wavelet transform based approach to detect blocks contaminated with motion artifacts using a hard threshold on the wavelet transform amplitude in a subset of scales without attempting to remove them. These scales were identified through Monte Carlo simulation on a training data set. In the method of Robertson et al., filtering is based on fixed threshold for each level as well as availability of optical motion reference signal [63]. Thresholding takes place only if the signal

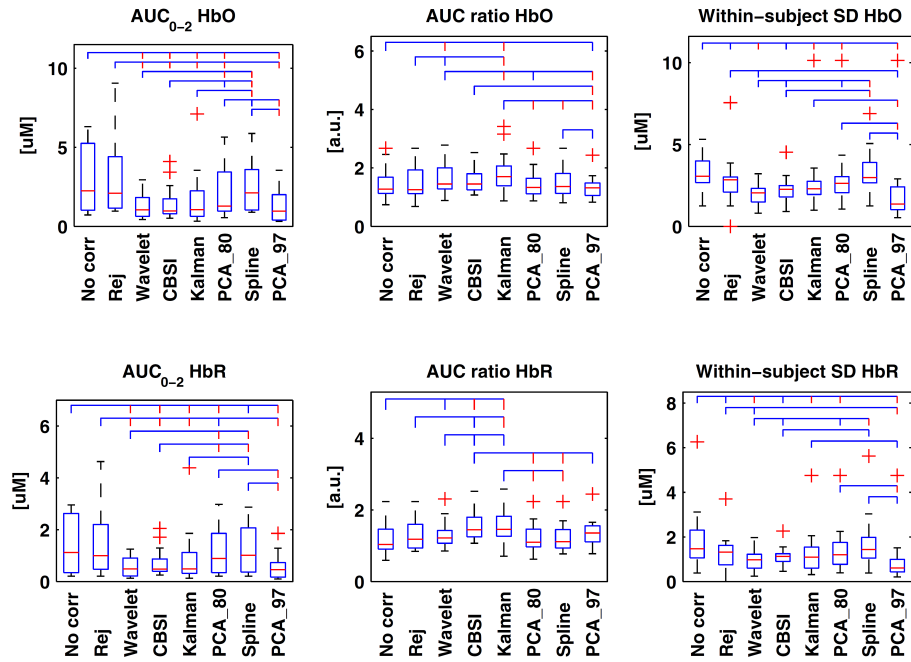


Figure 3.12: "Box plots of the AUC_{0-2} , AUC ratio and within-subject SD computed for all techniques and for both HbO (upper row) and HbR (bottom row). The red line in the box plot indicates the median, while the two extremities of the box plot represent the first and third quartile. Red crosses indicate outliers. The lines above linking the different techniques represent the significant statistical difference ($p < .05$ if the line is blue, $p < .01$ if the line is red)." [75] (Reprinted from NeuroImage, Brigadoi S. et al., Motion artifacts in functional near-infrared spectroscopy: A comparison of motion correction techniques applied to real cognitive data. Page 6, Copyright 2013, with permission from Elsevier Academic Press).

amplitude is larger than the threshold in its source or detector reference signals. This is different from our method in that we do not have any reference signal and wavelet coefficient shrinking is only based on the probability of having an artifact. The wavelet level selection in our method is adaptive and changes with the degree of contamination in the signal.

The performance of some common fNIRS motion artifact removal methods,

including the one introduced in this chapter, were compared using simulated and experimental data in two recent studies [74, 75]. Using experimental NIRS data collected from 22 subjects, Brigadoi et al. compared the performance of different motion artifact reduction methods [75]. The methods compared in this study included Kalman filtering [65], Correlation-based Signal Improvement (CBSI) [67], Principal Component Analysis (PCA) [131], spline interpolation [66], trial rejection and the wavelet based method introduced in this chapter and also described in [4]. In this study, subjects participated in a color-naming of a non-color word task during which the participants were asked to say aloud the name of the color of the word that appeared on a computer screen [75]. In this particular task, a motion artifact is caused by the jaw motion as the subject performs the task. Using 5 criteria, the performances of the methods in recovering the hemodynamic response were compared. The criteria used in this study were AUC for the mean HRF during the first 2 seconds of stimulation (AUC_{0-2}), the ratio of the AUC between 2 to 4s to that during the first 2 seconds (AUC_{2-4}), mean of the standard deviation of the hemodynamic response in each trial, between-subject standard deviation of the hemodynamic response and the number of trials averaged for every subject to compute HRF.

The summary of the results for three of the metrics in this study is reproduced in Figure 3.12 [75]³. According to this study, the proposed Wavelet method, CBSI, Kalman and PCA_97 showed lower values of AUC_{0-2} with less variability. The proposed method was found to be most effective in reducing AUC_{0-2} . As for the AUC ratio, CBSI and Kalman techniques had the highest AUC followed by Wavelet. The proposed method along with PCA_97 outperformed other methods in reducing the within-subject standard deviation with the Wavelet technique reducing standard deviation in 100% of the cases (see Figure 3.12). In this study, the proposed Wavelet method was also shown to be the only method to be able to recover all trials [75].

³Reprinted from NeuroImage, Brigadoi S. et al., Motion artifacts in functional near-infrared spectroscopy: A comparison of motion correction techniques applied to real cognitive data. Page 6, Copyright 2013, with permission from Elsevier Academic Press

Chapter 4

Non-Invasive Optical Monitoring of Bladder Filling to Capacity Using a Wireless NIRS Device

Lack of bladder fullness sensation is an issue that arises in different neurogenic conditions and in addition to influencing patients' quality of life, can result in serious kidney damage. We describe a wireless wearable sensor prototype and method for detecting bladder fullness using NIRS. The sensor has been tested in vitro and in vivo to verify its feasibility and is shown to be capable of detecting changes in bladder content non-invasively. The work in this chapter was accepted for publication in the *IEEE transactions in biomedical circuits and systems* and is also under review by the University of British Columbia University-Industry Liaison Office (UILO) for potential IP protection and licensing.

4.1 Introduction

The importance of a wearable wireless device capable of monitoring bladder content to help individuals with bladder control problem was discussed in Chapter 1. In this chapter, we describe the development, evaluation and pilot testing of a NIRS prototype for noninvasive optical monitoring of bladder filling to capacity using a compact wearable wireless system. We propose using this small, low-weight,

inexpensive, wireless and easy to use device as a noninvasive method for monitoring the point in time when the bladder becomes full, with lower computational requirements and complexity compared to ultrasonic continuous measurement systems. Our method employs the properties of NIR light absorption of human tissue and water to measure changes in water content in the field beneath a NIRS device. Because the bladder rises out of the pelvis below the anterior abdominal wall as urine accumulates within the organ, this device can detect when a bladder capacity previously defined by ultrasound is reached. When the bladder rises into the NIR light field as it fills, the water in the urine it contains results in high light absorption that generates an abrupt decrease in the light intensity sensed returning to the NIRS device. This event can be set to activate an alarm; potentially benefiting patients with any of the problems related to an inability to sense when their bladder is full.

4.2 Detection of Bladder Filling to Capacity Using NIRS

The major absorbing chromophores of physiologic interest in NIR wavelength window, as described in Chapter 1 are HbO₂ and HHb, as indicated in Figure 1.1. Water which is the main compound in urine (95% [132]), also has an absorption peak at 975nm and this peak can be used to detect urine content in the bladder and differentiate between an empty bladder, one with low volume, and a full bladder.

In NIRS, light in the NIR window is used to interrogate the tissue. A light source (emitter optode) is placed on the skin surface, with a detector (receiver optode) placed a few centimeters away. Changes in the light attenuation due to absorption of the transmitted light by chromophores in the tissue (HbO₂, HHb and water) are detected by the receiver optode. The resulting changes in raw optical data are then converted to changes in chromophore concentration. A common model used for this purpose, as described in Chapter 1 is the MBLL [16]:

$$A_\lambda = -\log \frac{I}{I_0} = (\sum_i \varepsilon_i(\lambda) c_i) BL + G \quad (4.1)$$

Where A_λ is the light intensity attenuation at wavelength λ , I_0 is the source intensity, I is detected light intensity, $\varepsilon_i(\lambda)$ is the extinction coefficient of chromophore i at wavelength λ in $\text{Lmol}^{-1}\text{cm}^{-1}$, c_i is the i th chromophore concentration in

molL^{-1} , L is the interoptode distance in cm, B is the differential pathlength factor and G is an additive term to take fixed scattering losses into consideration. This model is usually used in differential form to measure concentration changes in the tissue. The effective depth of penetration in this method is approximately half the inter-optode distance (see Section 1.6.1 for a discussion).

Self contained wireless NIRS devices have been utilized for a wide range of studies involving brain, muscle, and the bladder [87]. Such devices have the advantages of imposing less motion restriction, which means subjects can engage in relatively more active physical pursuits, and suitability for longer term monitoring in ambulant patients [87]. Wireless NIRS devices often use LED as the light source. Although LED based NIRS systems have a broader spectrum compared to laser-based NIRS devices, they have the advantages of being small, low weight, inexpensive, compact and self-contained and can be applied directly on the skin surface without need for the fiber-optic cables required for laser systems.

The hypothesis for our NIRS-based method for monitoring the level of urine in the bladder and to detect bladder filling to capacity was that with an LED light source using a wavelength close to the absorption peak of water at 975 nm, a self-contained NIRS device placed on the abdominal skin would detect water (urine) when the bladder enlarged into the NIR field. Ultrasound data indicates that as the bladder fills naturally the dome of the organ rises within the abdominal cavity bringing the bladder and the urine it contains into the NIR light field [133]. The water contained in the bladder then absorbs light causing a decrease in detected light intensity. Here, we describe a prototype of such a device as a proof of principle.

While this method is similar in concept to the method presented for continuous bladder monitoring using ultrasound [68], in our method it is the urine in the bladder (rather than the anterior wall of the bladder) which triggers the alarm. The level of bladder fullness that corresponds to the urine capacity that needs to be detected will depend upon the patients symptoms, and his/her underlying medical condition. In later development phases, this capacity value can be defined for individual patients, and the fullness and position of the bladder beneath the abdominal skin that this volume corresponds to can be assessed by ultrasound. The NIRS device is then positioned on the abdominal skin so that it alarms when the bladder reaches the size that corresponds to the capacity required for that patient.

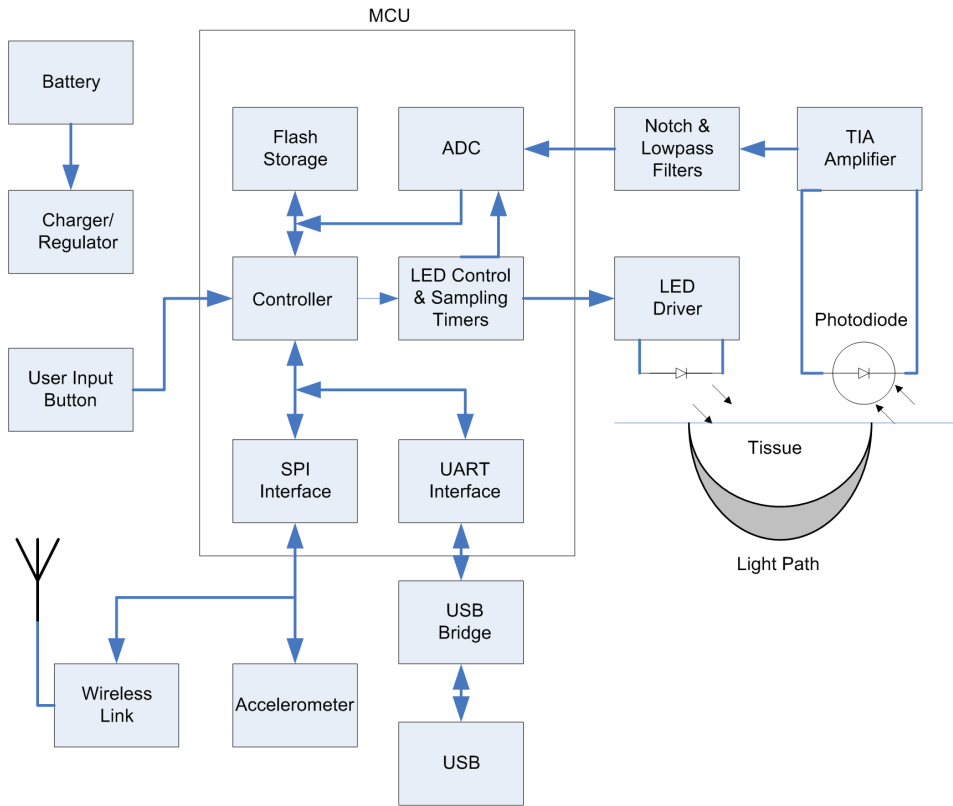


Figure 4.1: Sensor block diagram.

4.2.1 Electronics

The hardware consists of a $60 \times 70 \times 20$ mm wireless NIRS device, that is worn by the subject on the abdominal skin. The sensor can either operate offline by storing the data on board or in real time via a link to a base Personal Computer (PC) through a wireless USB dongle. The block diagram of the sensor is shown in Figure 4.1. The sensor is made using commercially available components on a 2-layer Printed Circuit Board (PCB) and is enclosed in a custom made 3-dimensionally (3D) printed enclosure as shown in Figure 4.2. The device weighs 55 grams. All components except the source LED and the detector are mounted using standard surface mounting technology. The source and detector are mounted on the front side of the enclosure using adhesive glue and are wired to the main PCB.

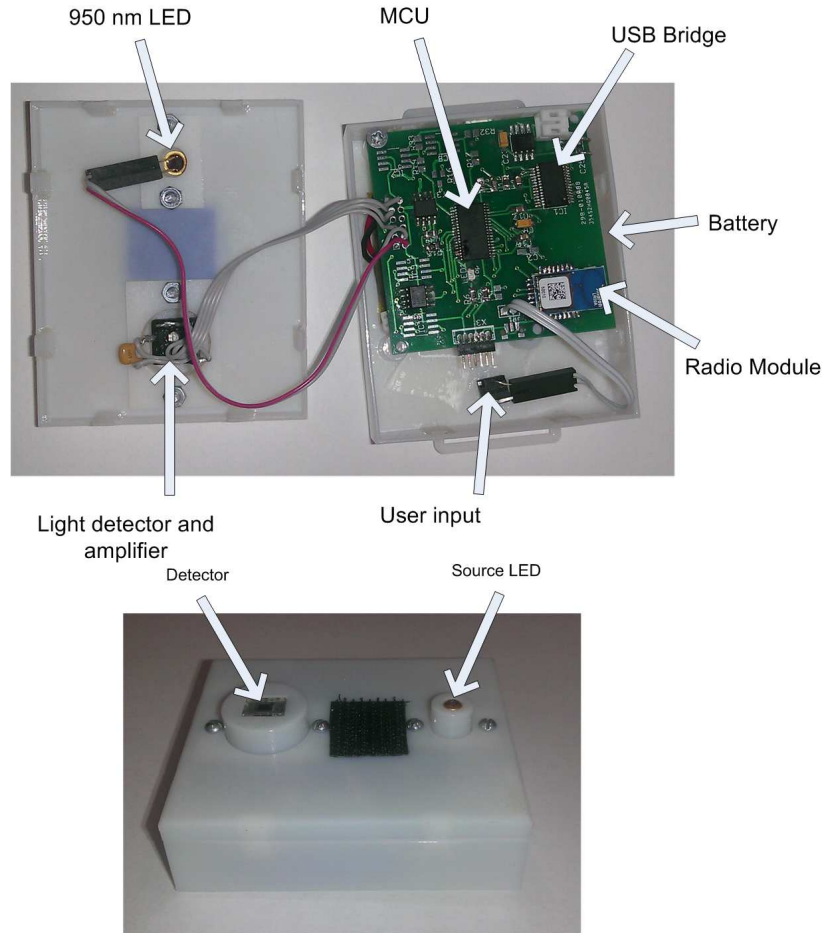


Figure 4.2: Sensor components (top) and device exterior view with extruded source and detector (bottom)

All the signal controls, sampling and processing are performed by a 16-bit low power microcontroller (MCU)(MSP430F2274 Texas Instruments, TX, USA) running at 16 MHz.

The source LED is a 950 nm LED (OSRAM Opto Semiconductors, 55 nm spectral half width, 16 mw nominal power) driven by a constant current driver, that in turn is controlled by a hardware timer. Even though the absorption peak of water is at 975 nm, the 950 nm source output is still highly absorbed by water as the spectral bandwidth of the source covers 975nm wavelength. The light detector is

a 5.22 mm² silicon photodiode integrated with a Transimpedance Amplifier (TIA) (OPT101, Texas Instruments). The responsivity of the detector is 0.45 A/W at 950 nm and the TIA is set to provide a gain of 6×10^6 V/A and a bandwidth of 2.5 kHz. The amplifier's output is filtered and sampled by 10 bit Analog to Digital Converter (ADC) integrated on the MCU. Prior to sampling by ADC, the output of the amplifier is filtered by an active twin T notch filter with center frequency at 60Hz to remove interferences from AC power line coupling and ambient lighting followed by a first order lowpass filter with $f_c=5$ kHz.

The sensor is powered by a 3.7 v, 850 mAh lithium-ion polymer rechargeable battery that provides up to 20 hours of continuous monitoring. The battery voltage is regulated down to 3.3 v through a low dropout linear regulator. The battery is recharged through a mini-USB connection.

In case of offline standalone operation the sensor can log data on the 16 kB onboard flash memory storage. The data can be later downloaded into a PC for further analysis.

Two communication interfaces are supported: wired using USB 2.0 connection and wireless using wireless link and a wireless dongle connected to a PC.

The wireless link uses 868-915 MHz band for communication and transfers data at 250 kbps. A wireless module based on Texas Instruments CC110L radio transceiver is used (A110L, Anaren Microwave Inc, NY, USA). The MCU communicates with the module over the Serial Peripheral Interface (SPI) bus at 250 kHz. The wireless link allows remote start and stop of data collection through PC, download of the logged data and real-time data streaming to the PC with a range of up to 20m.

A triple axis accelerometer (ADXL345, Analog Devices Inc., MA, USA) is used to detect motion to remove motion corrupted data segments. The accelerometer shares the SPI bus with the wireless module.

The sensor is encapsulated in a custom made 3D printed enclosure (Verowhite polyjet resin). An extruded feature that houses source and detector provides higher coupling with the tissue and also reduces the ambient light interference (see Figure 4.2).

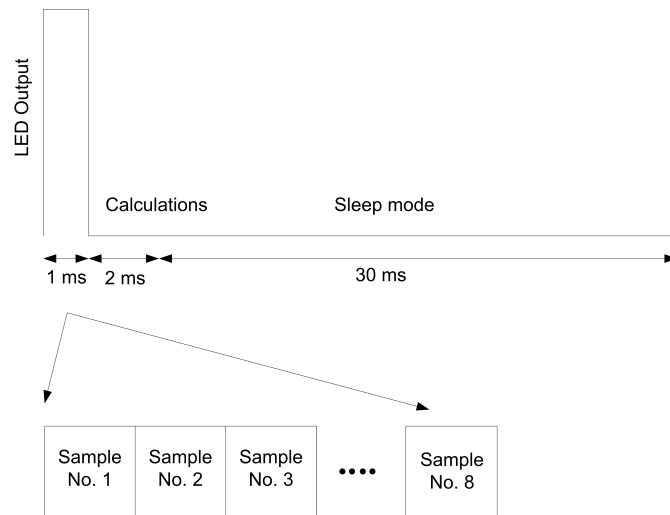


Figure 4.3: Timing of sampling.

4.2.2 Firmware

The firmware controls the source LED timing, data sampling process, logs data and communicates with a PC for command reception or data transmission.

The scattering and attenuation of light in the tissue result in 6-7 orders of magnitude decrease in signal power. As a result, to have better SNR at the detector output, higher source optical power is desired to increase the number of photons that can reach the detector. However, to limit the total tissue exposure and minimize the possibility of tissue thermal overheating, the power has to be kept within a safe range. An average power limit of 2 mW can be considered safe and has been used as the limit for similar NIRS devices [57, 134]. This power level also falls within the safe radiation levels defined in IEC 62471. To achieve this power level while having high instantaneous power, a source-switching scheme is employed as shown in Figure 4.3. We chose a 30 ms delay between the LED activation times. We also empirically found 60 mW of instantaneous power to result in well detectable light levels as the light exits the tissue for our interoptode distance of 3 cm. As a result, the source LED needs to be activated for a maximum of 800 μ s with instantaneous power of 60 mW which corresponds to a driving current of 370 mA (Figure 4.4) in order to keep the average power below 2 mW. This scheme also

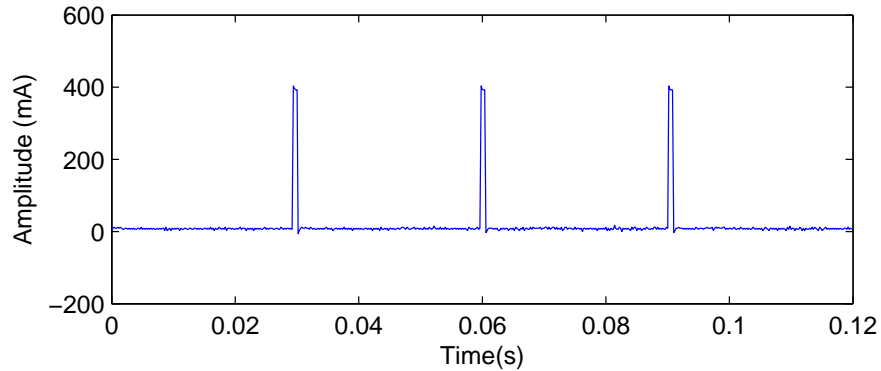


Figure 4.4: Snapshot of the LED driving current.

reduces the total power consumption.

To ensure accurate timing of LED driving pulses and ADC conversion triggers, the LED is driven directly by a hardware timer which is programmed to produce pulses every 30 ms. A separate timer triggers ADC conversion for sampling the LED light level. The TIA bandwidth of 2.5 kHz results in an approximate rise time of 140 μ s for the LED pulses. Therefore, sufficient delay before sampling is necessary to allow the transients at the detector output to settle. We used a delay of 600 μ s as shown in Figure 4.5, which shows the signal at the detector output along with the sampling trigger signal.

The detector's output signal is initially sampled at 83 kS/s and a total of 8 samples are recorded. These samples are then averaged and stored in a buffer. This sampling rate allows use of a low order antialiasing filter and collection of sufficient samples during the LED activation time. The next sampling cycle occurs in 30 ms and follows the same pattern. This is equivalent to sampling the continuous optical signal at 83 KS/s, low pass filtering it with a moving average filter of length 8 and then down-sampling the result to approximately 33 Hz. The digital averaging helps reduce the high frequency noise.

To prevent potential interference from ambient lighting, background light level is sampled as the baseline and subtracted from the detected light level. The firmware therefore takes a sample from background light level 800 μ s after turning the source LED off in each sampling cycle. This delay ensures all transients have

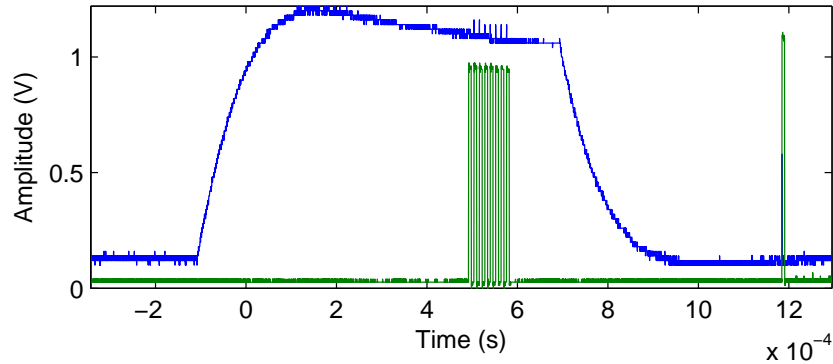


Figure 4.5: Detected signal at the detector for a source-detector separation of 3 cm (blue) with the sampling trigger signal (green). Eight samples are recorded with the source active and One sample is taken with source off which reflects the background lighting level.

settled and the background light level is being sampled properly.

The baseline corrected value is placed in a data packet along with a time stamp and transmitted wirelessly to the PC. In case of offline operation, it is logged onto the onboard flash memory.

The sensor operation can be controlled either by wireless commands through a PC or, for offline data collection, by user push button on the sensor.

4.2.3 PC Interface

A Graphical User Interface (GUI) based on MATLAB (Mathworks, MA, USA) is developed for remote controlling the sensor, streaming data from the sensor and saving it to a file for long term monitoring, downloading data stored on the sensor's memory and processing the signal in real time or offline (linear filtering, trend removal, etc.). A snapshot of the GUI with a sample data set is shown in Figure 4.6. The top panel shows the real time trace of the signal or the loaded data. The bottom panels contain controls for wireless operation and USB wired modes.

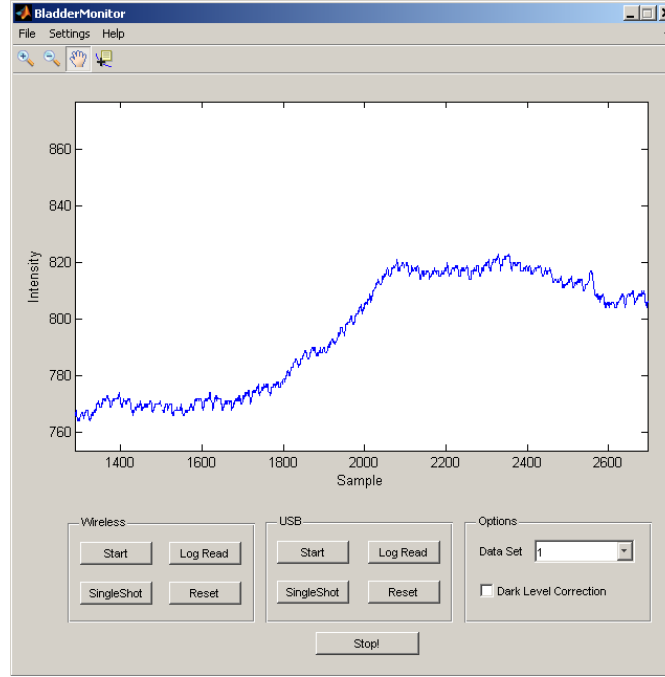


Figure 4.6: PC user interface screen shot.

4.3 Performance Evaluation

The sensor's dark noise was measured by readings obtained by placing the sensor in a dark room with no light incident on the detector for one hour. The Root Mean Square (RMS) value of the noise in this setup was calculated as:

$$V_n = \sqrt{\frac{1}{N} \sum (x[n] - \bar{x})^2} \quad (4.2)$$

where $x[n]$ is the signal read by the device in analog-digital conversion units. This process was repeated for a couple of measurements to obtain an estimate of the prototype's noise voltage. This value was calculated to be less than $470 \mu V$. The Noise Equivalent Power (NEP) was then calculated from dark noise measurements using

$$P_i = \frac{V_n}{R(\lambda)G} \quad (4.3)$$

where P_i is the incident light equivalent power in W, $R(\lambda)$ is the responsivity of

the detector at $\lambda = 950$ nm an A/W, G is the TIA gain in V/A and V_n is the noise voltage. The NEP is calculated to be approximately 180 pW. This defines the detection sensitivity for a signal to noise ratio of unity and is the minimum light level detectable by the sensor.

The long-term stability of the sensor was evaluated by continuous recording of data from a phantom using the sensor for 30 minutes after a warm up period of 1 minute. The aqueous phantom was prepared using method described in [135]. The phantom scattering and attenuation parameters are chosen to be close to those of abdominal tissue (in particular, abdominal fat with attenuation coefficient $\mu_a = 3$ cm^{-1} and reduced scattering coefficient $\mu'_s = 3.3$ cm^{-1} [136], see Section 4.6 for a discussion). The phantom was made with 20% intra-lipid mixed with ink to obtain desired optical parameters. The difference between the initial and final reading normalized to the initial signal value was recorded as the drift. The device shows 1.5% drift over the period of 30 minutes.

4.4 In Vitro Evaluation

4.4.1 In Vitro Setup

To verify the capability of the sensor in detecting bladder level changes in vitro, a simple setup as shown in Figure 4.7 was employed. The setup was made to simulate the bladder, urine and the abdominal tissue during bladder filling and voiding. A latex balloon was submerged in a phantom prepared as described in the previous section in such a way that the balloon neck is attached to the top of the container. The balloon can be filled with water from the top using a syringe. The distance of balloon from the side-walls was 1.5 cm when full and 6 cm when empty. The sensor was placed on the side-wall of the cylindrical container and secured with medical adhesive tape (3M, MN, USA). The data was recorded wirelessly.

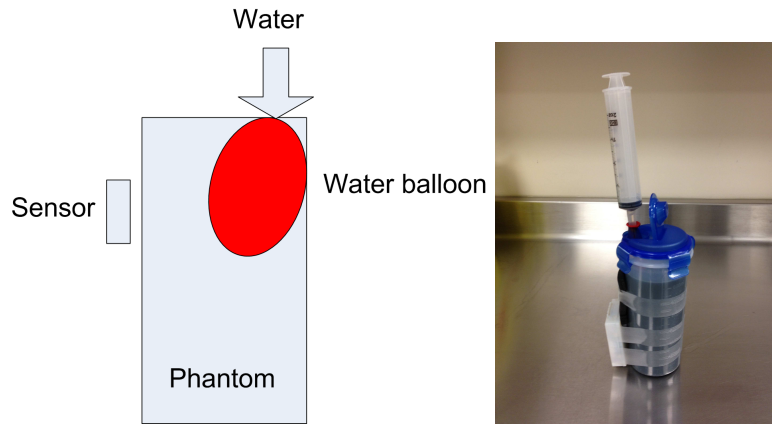


Figure 4.7: Schematic diagram of the in vitro setup for simulating bladder filling and voiding (left) with a picture of the setup (right).

4.4.2 Results

Figure 4.8 shows a sample recorded data when the balloon is filled and emptied. The intensity readings from the sensor were converted to attenuation as

$$A = -\log \frac{I}{I_0} \quad (4.4)$$

An increase in the amount of water in the optical path results in decrease in light intensity and therefore an increase in attenuation (A). As the balloon filling begins around $t = 9s$, the absorbance increases up to the point where the balloon is filled around $t = 10s$. Similarly, when voiding starts, the absorption reduces until the balloon is emptied.

The drop in the signal level between the end of the filling and the beginning of voiding is caused by motion of the balloon at the end of filling cycle as the result of ending water flow. The same occurs at the beginning of the voiding.

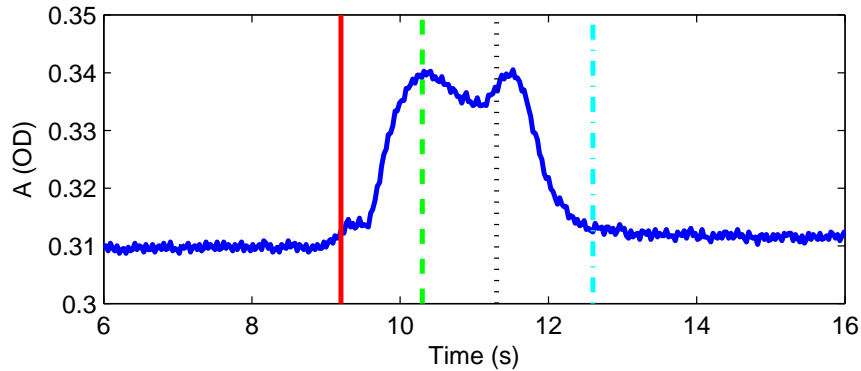


Figure 4.8: In vitro recorded data when the balloon is filled and emptied. Red, green, black and cyan lines indicate beginning of filling, end of filling, beginning of voiding and end of voiding, respectively.

4.5 In Vivo Evaluation

4.5.1 Materials and Method

Pilot data on 1 subject has been collected in 6 independent trials with the device during voiding to verify if the sensor is capable of differentiating between full and empty bladder. The sensor is placed 2 cm above the symphysis pubis across the midline during voiding as shown in 4.9 and is secured using medical adhesive tape. The absolute intensity reading from the detector is then converted to attenuation according to Equation 4.4 and used for comparison between full and empty bladder. Data was transmitted wirelessly to a PC for recording. For this proof of principle test, the motion rejection feature of the sensor using the accelerometer was not used.

4.5.2 Results

Figure 4.10 shows a typical attenuation signal recorded at source-detector separation of 3 cm. The red (solid), green (dashed) and black (dotted) vertical lines indicate permission to void, beginning of voiding and end of voiding, respectively. The signal shows a fall at the start of voiding and then plateaus around 15 s after beginning of voiding. This is possibly due to the fact that as the voiding begins,

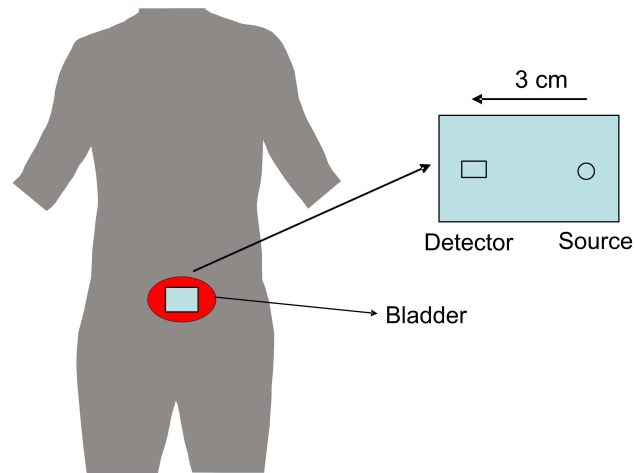


Figure 4.9: Sensor placement for in vivo device test.

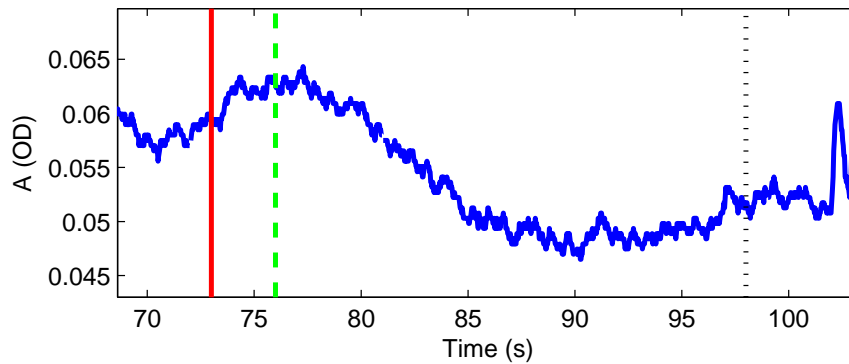


Figure 4.10: Attenuation detected during voiding with source-detector separation of 3 cm. The red (solid), green (dashed) and black (dotted) vertical lines indicate permission to void, beginning and end of voiding, respectively.

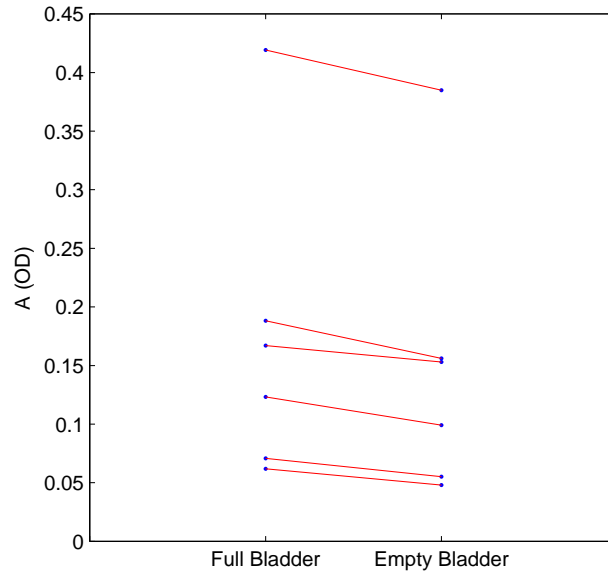


Figure 4.11: Comparison of detected light attenuation in full and empty bladders.

the bladder dome is in the light path between the source and the detector. As the bladder shrinks, the urine level in the light path reduces and light intensity at the detector increases (decrease in attenuation). At a certain point (in this case around 15 s after voiding begins), even though the voiding continues, the bladder is no longer visible to the sensor's light and therefore no further change in detected light intensity is observed.

Figure 4.11 shows the light attenuation changes between full and empty bladder for 6 independent trials with urine volume ranging from 300 ml to 700 ml. A significant difference in light absorbance is observed between pre- and post voiding states as shown in the figure (paired t-test $p < 0.01$). The starting point or baseline is variable among trials as a result of differences in light coupling, geometry, etc. However, there is a consistent difference between pre- and post voiding in the trials as a result of the change in bladder content (mean of the differences: 0.022 with standard error of mean of 0.0096).

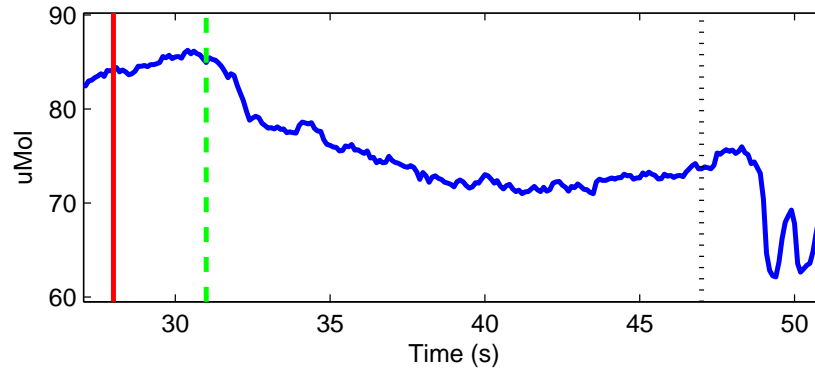


Figure 4.12: Water concentration in tissue changes during voiding using Oxymon MK III (Artinis BV, The Netherlands) as a general purpose desktop reference spectrophotometer with an interoptode distance of 3 cm. The red (solid), green (dashed) and black (dotted) lines indicate permission to void, beginning and end of of voiding, respectively.

Table 4.1: System level parameters of the sensor

| | |
|---|------------------------|
| Power consumption in standby | 63 mW (19 mA @ 3.3 V) |
| Active power consumption with radio transmission | 182 mW (55 mA @ 3.3 V) |
| Active power consumption without radio transmission | 122 mW (37 mA @ 3.3 V) |
| Range | 20 m |
| Light output power | < 2 mW |
| Cost | < 40 \$ |

For comparison Figure 4.12 shows the concentration changes detected during a separate voiding session when using a general purpose desktop laser-powered reference spectrophotometer (Oxymon MK III, Artinis BV, The Netherlands) with 971 nm laser for detection of water. The pattern of change in absorption is similar to those obtained with our prototype, even though the 971 nm signal is more sensitive to changes in water content.

Table 4.1 shows the overall system level parameters for the designed prototype. Active power consumption with and without radio refer to the cases when the device is linked to a PC and when the device is operating independently.

4.6 Discussion

We have developed a novel optical method for non-invasive monitoring of bladder capacity using a compact wireless NIRS prototype incorporating an LED with a wavelength of 950 nm and demonstrated the feasibility of using this device placed on the abdominal skin to detect a signal change that indicates when the bladder and the urine it contains have left the monitoring field of the device. Our data support our hypothesis that when the bladder fills and enlarges, the urine within the bladder can be detected using NIRS with a light source close to the absorption peak of water at 975 nm. Further validation of our NIRS-based method to detect when an individual's bladder capacity reaches a pre-defined limit is required, along with development of appropriate decision making process for activating filling alarm and comparison of the data obtained to results from 'gold standard' ultrasonic bladder scanning. Definition of the limit of bladder capacity will vary for each patient depending on their clinical condition, but once defined and the landmarks of the bladder with this capacity established by ultrasound, the device alone should suffice for monitoring when the patient's desired capacity is reached. Currently, there is no alternative method and device for continuous bladder filling detection, a very important clinical issue especially in patients with different types of urinary incontinence and patients with spinal cord injury.

Variations in fat layer thickness are a potential limitation during NIRS measurements [137]. However, since the thickness of the fat layer remains constant as the bladder fills and empties, no effect on light attenuation relevant to the monitoring of bladder capacity is generated. In obese subjects light absorption by a significantly thicker fat layer can be anticipated. This would result in an overall decrease in signal level and also increase the distance of the sensor from the bladder. This problem can be addressed to some extent by increasing the interoptode separation which effectively increases penetration depth along with shorter and higher power LED pulses. However, if the fat layer is too thick, it could prevent sufficient NIR light from reaching the bladder for our system to function.

The output of the system has a drift as described in Section 4.3 . This drift can mostly be attributed to slight temperature changes that result in a drift in the LED's output intensity. Even though this drift is negligible in short term compared

to changes during bladder voiding for example, it can add up in long term monitoring. To avoid this, the device can be set to restart filling monitoring after each alarm to prevent the error from accumulating over time. This process of resetting the device may also be required to account for the wide range of changes in absolute optical signal values read by the device. As shown in Figure 4.11 and discussed in Section 4.5.2, the parameter of interest is the change in signal attenuation. However, the large variations in the initial values may be a potentially serious limitation in using the device as a continuous monitoring system. The reason is that the device needs to register the initial value in order to measure the changes and if the initial value is dependent on parameters such as coupling, determination of a fixed threshold will be very hard. One approach to address this problem is restarting the measurement every time the device is placed on the bladder, or when the device is repositioned. A better and more robust alternative approach is to use methods that can take into account the changes in coupling such as the multidistance methods described in [138, 139].

Even though water has a high absorption peak at 975 nm, HbO₂ and HHb still contribute to absorption at this wavelength. This can be seen in Figure 4.6 and Figure 4.10 where absorption of light by HHb and HbO₂ result in heart beat and respiration systemic interference patterns appearing as small oscillations on the signal. However, the contribution of the change in these chromophores concentrations to the total signal attenuation during natural bladder filling compared to that of water is relatively small [27]. Also the similarity in the data obtained from our prototype and the reference spectrophotometer with wavelengths of 971 nm and 906 nm suggests that 950 nm wavelength is sufficiently sensitive for the monitoring function intended. However, if required, another pair of LEDs detecting changes in HbO₂ and HHb could be added to the device and software incorporated to remove the effect of hemoglobin from the total attenuation signal.

Similarly while motion induced artifact can be partially removed by the accelerometer on the sensor, incorporation of a dual source monitoring scheme would detect the coupling change or slow drifts caused by the small variations in the position of the device which can occur during continuous monitoring. In such a scheme the first channel would be placed over the bladder, with the second channel located further from the bladder so as to differentiate motion/coupling-induced changes in

the detected intensity from those caused by bladder water content changes. The changes caused by motion or changes in optical coupling will be highly correlated between the two channels, while changes caused by alterations in bladder capacity will only affect the channel located on the bladder.

The enclosure of our prototype was produced using a stereolithography based 3D printer and due to limitations we had for the material, it was made using a white color resin. This is not a recommendable option for a NIRS device. The white color of the enclosure results in a dominantly scattering with low absorption medium for the light exiting the tissue while ideally, the enclosure should absorb all photons leaving the tissue to closely simulate a semi-infinite boundary condition. For this reason, it is desirable to have a dark enclosure. Therefore, even though our results indicate the feasibility of this method and approach, this limitation needs to be addressed in the future.

The performance of our prototype was initially evaluated using a liquid phantom as described in Section 4.3 and Section 4.4. The values used for μ_a and μ'_s were from data measured at 1064 nm [136]. The value of μ_a at this wavelength may be too high compared to that of the prototype's source LED wavelength at 950 nm. This implies that the sensor's performance is likely to be better than the results of the in vitro test. Additionally, the use of a solid phantom is preferable to a liquid phantom as it provides more stable properties and does not require a container which may affect the results as the light passes through it to reach the phantom [140].

The PC connectivity, in addition to providing an alternative method for device control as well as data processing and storing, can potentially be beneficial in cases where remote monitoring of a subject's bladder activity is of interest. In Urinary Tract Infection (UTI), for example, which is a common condition in spinal cord injury patients, the frequency of voiding increases and access to this information collected in normal daily life conditions by the clinician is important in treatment of patients. In this case, the limited range of connection might limit the usage of wireless link to indoors only. However, the same benefits could potentially be offered by replacing the PC with a smart phone in the future.

For our device to reliably monitor ambulant subjects consistently and with the level of accuracy required for detection of bladder capacity in selected patient

groups, additional trials and development are required. In particular the potential effect of different body postures, positions and clinical conditions needs to be evaluated. Some MRI studies have suggested that body position in young subjects does not affect the shape and position of the bladder significantly [141]. This needs to be verified on our population of interest whose physiological conditions may differ from young subjects. Data will also need to be collected in cohorts where the age range and diagnostic criteria match those of the patients for whom monitoring with a device such as ours is considered of potential benefit.

4.7 Conclusion

We have designed and developed a compact wireless optical sensor prototype for continuous non-invasive monitoring of the bladder in patients who are unable to sense when their bladder is full. This is a significant clinical problem in individuals with abnormal (neurogenic) bladder function, such as patients affected by MS, stroke and/or spinal cord injury, elderly patients with incontinence, and children with persistent enuresis. The device is capable of differentiating between when the bladder is empty or contains a small volume of urine and when it becomes full, by using the absorption properties of water at a wavelength of 950 nm . With such a device used as a sensor with an alarm, it is hence feasible to warn the subject when the volume of urine in his/her bladder reaches a pre-determined threshold of the bladder capacity. This would potentially enable patients at risk for urinary retention to protect themselves from renal damage, elderly subjects prone to incontinence to retain the ability to void voluntarily, and children with problematic enuresis to become conditioned to when they need to wake to void. Further clinical studies with this device are required to validate this method.

Chapter 5

Cortical Connectivity Analysis

Using fNIRS

The interaction between spatially separated cortical regions plays an important role in performing a cognitive task. Functional imaging methods such as fNIRS are capable of detecting activated areas of the brain based on hemodynamic changes associated with increased neural activity. fNIRS as an inexpensive and portable equivalent to fMRI can help identify functional or effective connections and interactions among cortical areas in a particular task. In this chapter, we first present our preliminary method and results on detecting connections between brain regions in a speech study using fNIRS and MVAR modeling. We then describe an analysis method for mapping resting state cortical networks using phase synchronization and present results of applying this analysis method to fNIRS data from neonates to map the language network. The preliminary material in the first part of this chapter was published in *International IEEE EMBS Conference* in 2011 [5]. The material in the second part of this chapter has been submitted and is currently under review for consideration for publication.

5.1 Functional Connectivity Using Multivariate Autoregressive Modeling

MVAR modeling is a common approach to studying the interaction between brain regions in fMRI [142] and EEG [143]. MVAR can establish a direct measure of functional relation between brain regions.

We used MVAR modeling to measure time varying connectivity between temporal and frontal areas of neonates brain during a neurocognitive study using fNIRS. Higher temporal resolution along with non-confining nature of fNIRS makes it a natural choice for study of functional connectivity and its temporal evolution in infants. Study of connectivity and its changes on infant can contribute to a better understanding of the early learning process.

5.1.1 Materials and Method

MVAR Modeling for Time Varying Connectivity

An AR model for multichannel fNIRS signal can be written as [144]

$$Y(n) = \sum_{i=1}^p A(i)Y(n-i) + \varepsilon(n) \quad n = p \dots N \quad (5.1)$$

where $Y(n) = [y_1(n) \ y_2(n) \ \dots \ y_L(n)]^T$ is the L channel fNIRS measurement at time point n , p is the maximum lag and N is the total number of available samples. $A(i) = [a_{jk}(i)]$ is an $L \times L$ matrix in which $a_{jk}(i)$'s are the AR coefficients describing $y_j(n)$ in terms of $y_k(n-i)$. $a_{jk}(i)$ can give a measure of connection in terms of causality between signals in different channels and shows how much of the energy of signal in channel j can be represented by signal in channel k . $\varepsilon(n)$ is a normal identically and independently distributed noise with zero mean. Equation 5.1 can be rewritten as

$$\mathbf{Y} = \mathbf{XA} + \mathbf{E} \quad (5.2)$$

where $\mathbf{A} = [A^T(1) \ A^T(2) \ \dots \ A^T(p)]^T$ is a $(p \times L) \times L$ matrix of MVAR coefficients at lags 1 to p , $\mathbf{Y} = [Y^T(n) \ Y^T(n-1) \ \dots \ Y^T(p+1)]^T$ is an $(N-p) \times L$ matrix,

and \mathbf{X} defined as

$$\mathbf{X} = \begin{pmatrix} Y(n-1) & Y(n-2) & \cdots & Y(n-p) \\ Y(n-2) & Y(n-3) & \cdots & Y(n-p-1) \\ \vdots & \vdots & \ddots & \vdots \\ Y(p) & Y(n-p-1) & \cdots & Y(1) \end{pmatrix} \quad (5.3)$$

is an $(N-p) \times (L \times p)$ matrix.

The maximum likelihood estimator of \mathbf{A} is [144]

$$\mathbf{A} = (\mathbf{X}^T \mathbf{X})^{-1} \mathbf{X}^T \mathbf{Y} \quad (5.4)$$

In order to track possible changes in a_{jk} in the time course of the signal, one can divide the signal into smaller segments and estimate \mathbf{A} in each segment:

$$\mathbf{A}^m = (\mathbf{X}_{s_m}^T \mathbf{X}_{s_m})^{-1} \mathbf{X}_{s_m}^T \mathbf{Y}_{s_m} \quad (5.5)$$

in which \mathbf{X}_{s_m} and \mathbf{Y}_{s_m} are formed by replacing $Y(n)$ with $Y_{s_m}(n)$:

$$Y_{s_m}(n) = \begin{cases} Y(n), & mW \leq n < (m+1)W \\ 0, & \text{else} \end{cases} \quad (5.6)$$

in which W is the sliding window width. In other words, we fit the AR model to a small window of the signals. The window is then shifted one sample in the forward direction and the model is fitted again to the data in the new window.

In order to summarize the effect of AR coefficients at different time lags between 2 channels, we define a connectivity index as

$$c_{jk}(n) = \frac{\sum_{i=1}^p \tilde{a}_{jk}(i)^2}{\sum_{k=1}^L \sum_{i=1}^p \tilde{a}_{jk}(i)^2} \quad (5.7)$$

where $\tilde{a}_{jk}(i)$'s are the elements of \mathbf{A}^m . $\sum_{i=1}^p \tilde{a}_{jk}(i)^2$ represent the contribution of signal in channel k in minimizing the prediction error of AR model in channel j . Larger value for this parameter means information in channel k can be used to better predict values in channel j given the past values of both channels. This pa-

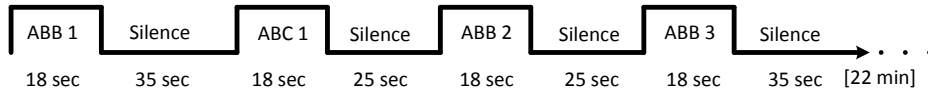
parameter has also been referred to as Direct Causality (DC) in the literature [145]. The denominator in Equation 5.7 is the sum of such effects from all other channels. Normalization ensures comparable values over different subjects. $c_{jk}(n)$ is evaluated for every time window as defined in Equation 5.6. We now define the connectivity matrix as $C(n) = [c_{jk}(n)]$. Each element of connectivity matrix $C(n)$ shows the causal effect of channel k on channel j at time point n .

fNIRS Experiment and Data

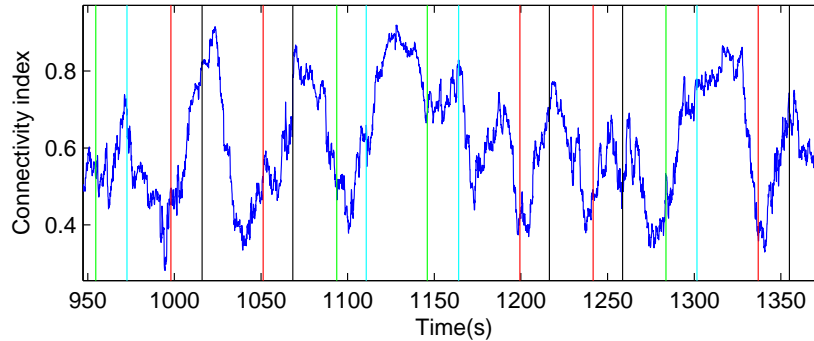
The purpose of this experiment is to study the changes in functional connectivity in neonates brain when exposed to two different types of audio stimuli. The experiment was originally designed to study the ability of neonates to learn simple underlying structures in speech [24]. To establish the feasibility of our method, we applied it to 3 representative cases from the original study [24]. The selected subjects were all female with ages 2,3 and 4 days, respectively. Informed consent was acquired from parents when the experiment was being conducted. The study design was approved by the ethics committee of the Azienda Ospedaliera Universitaria di Udine, Italy where the experiments were conducted [24]. During the 22-25 minute long testing session, audio stimulus was administered to subjects while the subjects were in the state of quiet rest or sleep. The audio stimuli consisted of consonant-vowel syllables organized into syllable pairs and were divided into 2 major "grammar" groups named "ABB" and "ABC" based on their syllables repetition order. Each grammar was presented in blocks of 18 seconds long followed by a silence of randomly varying duration (25-35 seconds). A total of 14 blocks for each stimulus was presented. Figure 5.1-a shows the experiment design.

The hemodynamic changes associated with increased neural activity in response to the 2 types of stimuli were monitored by an fNIRS device (24 channel Hitachi ETG-4000 machine with 695 and 830 nm lasers, interoptode distance of 3 cm and sampling rate of 10 Hz). The optode placement and the location of channels is shown in Figure 5.2. The tragus and the vertex were used as landmarks for optode positioning to ensure data is recorded from perisylvian and anterior brain regions.

Earlier study using the same dataset indicated that neonates were capable of



(a) Experiment's design



(b) Representative connectivity index

Figure 5.1: Experiment design and a representative connectivity index (between channels 2 and 5 for subject 3). Red and green lines denote the beginning of the ABB and ABC blocks, while cyan and black indicate the end of blocks.

discriminating between the grammars [24]. The discrimination was indicated by significant increase in HbO_2 in response to one type of stimulus in temporal and frontal regions of neonates brain. The temporal region is known to be responsible for auditory processing in infants [146] while the frontal areas are responsible for computation of structure and higher order representations in infants and adults [146]. Since the process of learning the grammar types involves 2 spatially separate areas of the brain, it is natural to assume a functional connectivity network should be involved. The purpose of current pilot study was to use the data collected in the same experiment and detect possible changes in such connections as a result of exposure to stimuli using the proposed method.

Before applying functional connectivity analysis, raw optical data collected by fNIRS device was converted to changes in HbO_2 and HHb concentration using MBL [29]. The signals were highpass filtered to remove any overall trend in the signals. A window of length 200 samples (20 seconds) was used to estimate AR

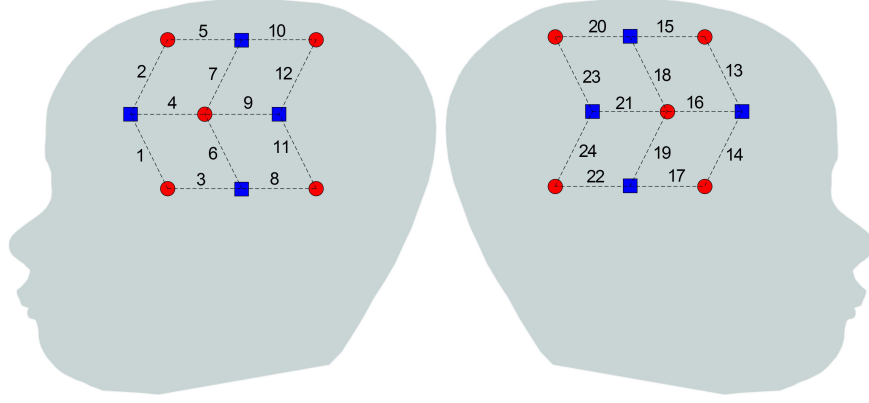


Figure 5.2: Side view of fNIRS optode holder overlaid on schematic representation of neonates head. The red and blue dots indicate the source lasers and detectors, respectively. The numbers between the dots are the channel numbers. The optodes are placed such that they sample data from perisylvian and anterior brain regions.

coefficients in each step according to Equation 5.6.

Channels 1 to 6 on the left hemisphere were chosen to study the functional connectivity. This choice is based on the fact that the temporal region (represented by channels 3 and 6) and frontal region (represented by channels 2,5 and possibly 1) are the major areas involved in processing audio stimuli and processing structures, respectively. Earlier studies have also shown that language function is left hemispheric dominant [24, 147]. Therefore, we limited our study to the left hemisphere only. Also, only HbO_2 changes were analyzed for this study. It has been shown that HbO_2 is more sensitive to regional cerebral blood flow changes [24, 148].

MVAR model is estimated for channels 1-6. We are interested in overall connectivity difference between conditions (grammars), which means a function of $C(n)$ must be employed to summarize the connectivity matrix in each block for the conditions. We use simple averaging as

$$\bar{c}_{jk}^{B_i} = \frac{1}{M} \sum_{n \in B_i} c_{jk}(n) \quad (5.8)$$

to form $\bar{C}^{B_i} = [\bar{c}_{jk}^{B_i}]$ where B_i is the i th block of condition B, where B is either

type "ABB" or "ABC". M is the total number of calculated matrices in the block.

The resulting connectivity matrices \bar{C}^{B_i} are grand averaged to yield overall connectivity matrix for each condition in every subject. Blocks involving motion artifacts are excluded from this procedure. Motion artifacts are identified by changes larger than 0.5 mMol.mm/s in the concentration changes.

5.1.2 Results

Figure 5.1-b shows a representative connectivity index between channels 2 and 5 ($c_{52}(n)$). The duration of each stimulus is indicated by vertical lines. The figure suggests that the connection between the 2 channels becomes stronger when the stimulus is being presented.

Figure 5.3 shows the connectivity matrix for the 3 test subjects. Self connections are not shown in the figure. Connections with strength of less than 15% of maximum strength in each subject are not shown in the connectivity network in the right panels of Figure 5.3. In order to differentiate conditions, overall connectivity matrix for condition "ABC" is subtracted from that of condition "ABB" to yield the difference in average connectivity between the 2 conditions. This difference matrix shows channels whose connectivity is stronger in one condition compared to the other. This is important as there may be larger and more complicated networks involved in accomplishing a particular task while we are only interested in connections which are stronger for the "ABB" grammar.

All three subjects demonstrate strong connectivity between temporal and frontal areas. This is indicated by connection from channel 6 to 2 and 5 in subject 1, 6 to 2 in subject 2 and 2 to 6 in subject 3.

Also in subject 1, channel 6 shows strong connection with channels 3 which in turn has connection with channel 5 in temporal region. Possible explanation can be that channel 6 is the lowest/first level of auditory processing, its output feeds into channel 3. The next level of auditory processing, channel 3 then connects with the frontal area, channel 5 for higher level structural processing. This can also be observed in subject 3.

The connectivity matrices provide an overall comparison of functional connections between temporal and frontal areas. Another interesting analysis would be to

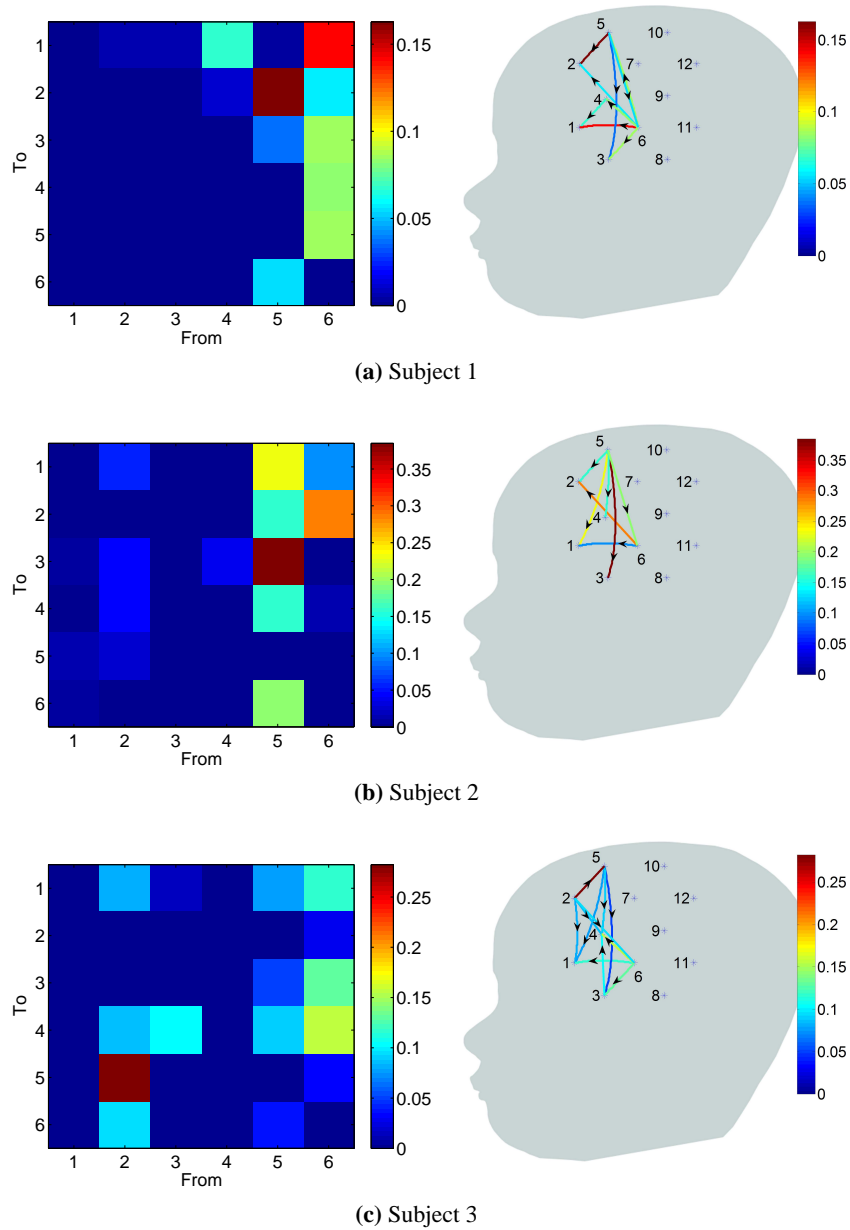


Figure 5.3: Connectivity matrices and networks for 3 test subjects. Connection strength is color coded. Only connection paths which are stronger in condition "ABB" compared to condition "ABC" are shown. The rest are set to zero. Figures on the right show a graphical representation of the connectivity network overlaid on a head model (lateral view).

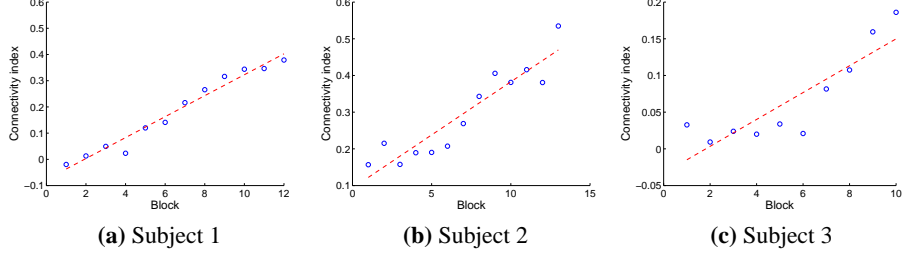


Figure 5.4: Temporal evolution of connection strength between temporal region and frontal region. For subjects 1 and 2, plots represent connection from channel 6 to 2. For subjects 3, plot represents connection from channel 2 to 6. $r^2=0.97$, $r^2=0.87$, $r^2=0.76$ for subjects 1 to 3, respectively.

investigate the temporal evolution of connectivity matrices \bar{C}^{B_i} across the blocks. The hypothesis is that this evolution should be associated with learning in infants and should therefore change as the subjects are exposed further to the stimuli. We studied this by investigating temporal evolution of connection strength between representative temporal and frontal channels. Channels 6 and 2 are selected as they have strong temporal-frontal connection in all 3 subjects. Figure 5.4 shows the plots of connection strength vs block number. Each point corresponds to average connectivity strength within a stimulus block. All three subjects show an increase in connection strength in the time course of the experiment.

5.2 Analyzing Resting State Functional Connectivity in The Human Language System Using Near Infrared Spectroscopy

As discussed in Chapter 1, fNIRS can measure the neuronal activity in response to a task or an environmental stimulation through neurovascular coupling in superficial areas of the brain. fNIRS has been used for functional studies as a portable, less expensive and less restraining alternative to fMRI in different task based brain functional studies. One of the more recent areas of interest in both fNIRS and fMRI is the study of interaction between different cortical areas through their in-

trinsic neuronal signaling [97, 101]. This intrinsic signaling appears in the form of slow varying spontaneous fluctuations in the BOLD signal in the absence of stimulation. These fluctuations are correlated between brain areas that are anatomically and functionally connected and have been used to map brain functional networks such as sensorimotor, visual, and auditory as well as higher networks such as language and attention [149, 150]. These networks are often mapped from the data collected at rest and are therefore referred to as Resting State Functional Connectivity (RSFC) maps.

The RSFC analysis can potentially identify changes in intrinsic neural activity as a result of disease in some neurological and psychiatric conditions. Changes in connectivity strength in different brain networks have been observed in conditions such as autism [151], depression [152], Alzheimer disease [153] and attention-deficit hyperactivity disorder [154].

Given the advantages of fNIRS, different brain networks have been investigated through RSFC using fNIRS. One of the most common methods for analyzing brain network connectivities using RSFC in fNIRS is cross correlation [149]. In cross correlation, an fNIRS channel is selected as the seed channel and the correlations of the signal in all other channels with the seed channel are calculated. The objective is to find the cortical areas whose resting state fluctuations are similar to that of the seed channel. Cross correlation-based functional connectivity has been investigated in conjunction with fNIRS to derive connectivity maps in different brain networks [97, 107, 108]. One drawback of correlation based connectivity is that it can be sensitive to detection of spurious connection as a result of presence of cross talk between channels, systemic interference or noise [155].

In this section, we have investigated the phase relation between fNIRS channels and have used it as a measure of functional connectivity. Compared to methods based on signal amplitude such as cross correlation, phase is much less sensitive to noise and interferences. It also does not require the assumption of stationarity for the signals. Phase synchronization is not equivalent to coherence or frequency synchronization and is an independent characteristic of the interrelationship between two processes [155]. To evaluate the feasibility of this analysis method for detecting functional connectivity, we applied it to a study of processing of speech vs. non-speech in newborn human infants. This type of comparison is of particular

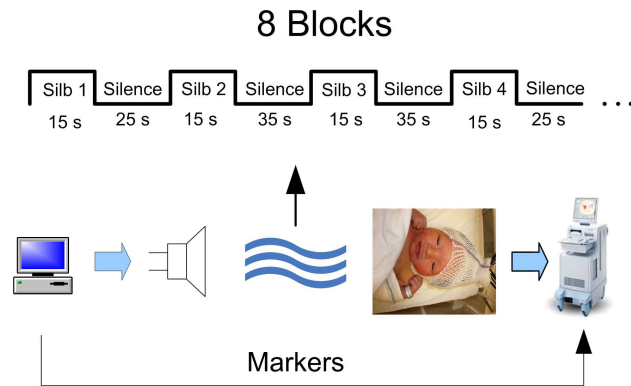


Figure 5.5: fNIRS experiment setup.

value for the question being asked as there is a growing body of evidence on the brain areas involved in language processing in neonates, but less on the underlying connectivity.

5.2.1 Material and Methods

fNIRS Data

The fNIRS data was collected from newborn infants at BC Children’s hospital, Vancouver Canada, during a separate language perception study [156]. Informed consent was obtained from parents when the experiment was being conducted. The study design was approved by the ethics committee of the University of British Columbia. The experiment design and setup are shown in Figure 5.5. A total of 19 subjects were used in the analysis out of which two subjects were excluded due to severe artifacts in the signals and poor data quality resulting from optode displacement during data collection. During the experiment, audio stimulus was administered to subjects while the subjects were in state of quiet rest or sleep. The audio stimuli consisted of blocks of sentences in Spanish and Silbo-Gomero. Silbo-Gomero is a whistled language that is a surrogate language of Spanish. It uses whistles rather than speech, and was developed by shepherds in the Canary Islands to communicate across long distances. Spanish and Silbo-Gomero were selected as both are unfamiliar to the infants, while one is a spoken language and

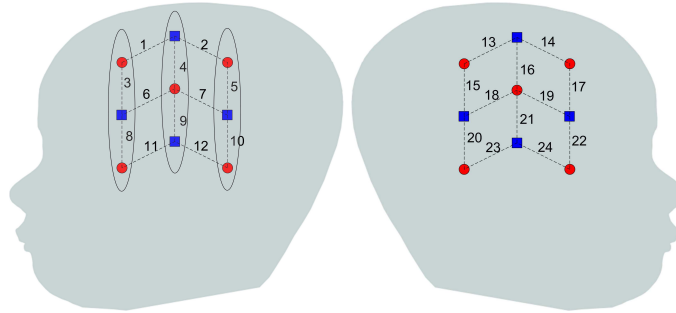


Figure 5.6: Optode placement on the head. Blue squares and red dots indicate detectors and sources, respectively and the numbers indicate the channel number.

the other is not. Each block was 15 seconds long followed by 25-35 seconds of silence. A total of 8 blocks for each stimulus were presented in which each block consisted of continuous speech. The total experiment time was 22-25 minutes.

The subjects' brain hemodynamic response was monitored by a 24 channel fNIRS device (Hitachi ETG-4000 machine with 695 and 830 nm lasers at a power of 0.75 mW, interoptode distance of 3 cm and sampling rate of 10 Hz). Two chevron shaped optode holders secured nine 1 mm fibers to the head. There were a total of 4 detector and 5 source fibers on each holder resulting in 12 recording channels per holder. Figure 5.6 shows the placement of optodes on the subject's head. Surface landmarks (ears or vertex) were used for the placement of the probe holder over the infant's perisylvian area of the scalp. Channels 11 and 12 in the left hemisphere and 23 and 24 in the right hemisphere were ideally placed above the infant's ear. A stretchy cap secured the holders on the infants' head.

Data Analysis

In order to determine the phase relation between channels, we first extracted the phase of the signal in each channel using the Hilbert transform. Hilbert transform converts a real valued signal to a complex one, known as analytic signal, whose real part and phase correspond to the original signal and its derived phase, respectively [157]. The Hilbert transform of signal $x[n]$ in the frequency domain is defined as

[157]:

$$Y(e^{j\omega}) = -j \operatorname{sgn}(\omega) (X(e^{j\omega})) \quad (5.9)$$

where $X(e^{j\omega})$ is the Fourier transform of $x[n]$ and $\operatorname{sgn}(\omega)$ is the sign function having value of 1 for $\omega > 0$ and -1 for $\omega < 0$. The analytic signal can then be written as

$$x_a[n] = x[n] + jy[n] \quad (5.10)$$

where $y[n]$ is the inverse Fourier transform of $Y(e^{j\omega})$.

We use the joint probability distribution of the phases across channels to describe their connectivity. A common model for probability distribution of phase which is the circular analogue of the Gaussian distribution is the Von Mises distribution. The Von Mises probability density function (pdf) is defined as [158]:

$$f(\theta|\mu, \kappa) = \frac{1}{2\pi I_0(\kappa)} e^{\kappa \cos(\theta - \mu)} \quad (5.11)$$

where θ is an angle defined in the interval $[-\pi, \pi)$ and $I_0(\kappa)$ is the modified Bessel function of order 0. The parameter κ is the equivalent of the covariance for the Gaussian distribution and μ is the expected value of the angle. The probability density function of the signal phase in channel m conditioned on that of channel n can therefore be written as:

$$f(\theta_m - \theta_n|\mu, \kappa) = \frac{1}{2\pi I_0(\kappa)} e^{\kappa_{mn} \cos(\theta_m - \theta_n - \mu)} \quad (5.12)$$

κ_{mn} describes the intensity of phase correlation between signals in channels m and n . In other words, it shows how much prior information of θ_n affects distribution of θ_m . The first moment of the distribution given in Equation 5.11 can be calculated as [158]

$$\begin{aligned} m_1 = E[e^{j\theta}] &= \int_{-\pi}^{\pi} e^{j\theta} f(\theta|\mu, \kappa) d\theta \\ &= \frac{I_1(\kappa)}{I_0(\kappa)} e^{j\mu} \end{aligned} \quad (5.13)$$

Using the first moment, one can estimate parameter κ by numerically solving the optimization problem

$$\arg \min_{\kappa} \left(|m_1| - \left| \frac{1}{N} \sum_{i=0}^{N-1} e^{j\phi_i} \right| \right)^2 = \quad (5.14)$$

$$\arg \min_{\kappa} \left(\frac{I_1(\kappa)}{I_0(\kappa)} - \left| \frac{1}{N} \sum_{i=0}^{N-1} e^{j\phi_i} \right| \right)^2 \quad (5.15)$$

where N is the number of samples in the data segment and ϕ_i is the measured phase of the signal at time point i . Parameter μ can then be estimated using

$$\mu = \angle \frac{1}{N} \sum e^{j\phi_i} \quad (5.16)$$

A close relationship exists between parameters of the distribution and the phase locking value (PLV) which is a common measure used in EEG signal processing to detect functional connectivity through synchronization between channels. PLV is related to the distribution through the magnitude of the first circular moment of the phase distribution [159]

$$PLV_{mn} = \left| E \left[e^{j(\theta_m - \theta_n)} \right] \right| = \frac{I_1(\kappa)}{I_0(\kappa)} \quad (5.17)$$

One advantage of using Von Mises distribution over phase locking for connectivity analysis is that once the parameters are estimated, one would have the distribution function and can re-sample from the distribution to determine the significance levels. Also, the preferred phase difference is not available in PLV.

To evaluate fNIRS functional connectivity, we first calculated the phase from all fNIRS channels using the Hilbert transform as described earlier. Ideally, we would be interested in phase relations between channels when subjects are not exposed to any type of stimulation to reveal intrinsic network activities. It was shown in an earlier study, however, that the infant brain produces no significant response in the language network to Silbo-Gomero stimuli [156]. We therefore used the fNIRS data during Silbo-Gomero stimulation as an alternative to resting state. The BOLD spontaneous fluctuations are concentrated at frequencies of less than 0.1 Hz. Therefore, the signals were first filtered with an infinite impulse response bandpass

filter (IIR) between 0.02-0.08 Hz to extract spontaneous hemodynamic activities and reject other interferences. This frequency range is comparable to those used in other studies investigating RSFC using fMRI and fNIRS [101, 108].

fNIRS data in general can be contaminated with motion artifacts as the result of subjects' spontaneous movements. These artifacts create interference in the form of highly correlated phase changes in fNIRS channels, especially in spatially close channels. This interference results in very high phase correlation and can obscure underlying phase connections between channels. Even though filtering of the motion artifacts is possible, in order to minimize possibility of introducing any interdependence between channels, no artifact removal procedure was applied. Instead, the channels for all subjects were inspected visually and artifact contaminated regions within the Silbo-Gomero stimulation window were marked. An artifact free segment of the data in each channel was then selected for the analysis and the phase of the selected signal segments were then derived using the Hilbert transform. Since the brain shows no response to this stimulation type, the stimulation onsets were ignored and the segments were selected independent of the stimulation onsets. The segments contained variable number of stimulation blocks and their length ranged from 50s to 220s.

The channel with the highest activation in the grand average for the Spanish stimulation task during the original study in the left hemisphere was selected as the seed channel for the RSFC analysis. The joint phase distribution of the seed channel and all other channels was then estimated by calculating the phase difference between the seed channel and other channels and then estimating κ_{mn} and μ_{mn} using Equation 5.15 and Equation 5.16. We used a simplex derivative-free method to solve Equation 5.15 and derive κ_{mn} [160]. The analysis was performed in MATLAB (Mathworks MA, USA) and the phase coupling estimation toolbox developed by Cadieu et al. was used for parts of the analysis [161]¹.

The analysis was performed on HbO₂ changes only. Previous studies on the application of fNIRS to detect language network activity and connectivity have shown that HbO₂ is more sensitive to regional cerebral blood flow changes than HHb with the equipment used here [24, 107, 148].

¹<http://redwood.berkeley.edu/klab/pce.html>

To examine the validity and reliability of the connectivity information derived with this method, we divided the subjects randomly into two groups and evaluated the connections for each group, similar to the approach proposed in [106]. We then compared the correlation of the connectivities between the groups.

Other studies have suggested that language network is left lateralized. We verified this in the network derived using our method. The lateralization was quantified using [106, 162]

$$LI = \frac{1}{M/2} \sum_{i=1}^{M/2} \frac{\kappa_L^i - \kappa_R^i}{\kappa_L^i + \kappa_R^i} \quad (5.18)$$

where M is the total number of channels, κ_L^i is the value of κ_{is} in which i is the channel number and s is the seed channel in the left hemisphere. κ_R^i is the value of the same parameter with the channel symmetric to i in the right hemisphere. The significance level of the calculated lateralization index is then evaluated. The lateralization index results in a number between -1 and 1 with more positive numbers indicating higher degrees of left lateralization.

As the final step, we defined 4 ROI, 2 inside the language network and 2 outside the network and evaluated the connection strengths in these areas. In particular, channels 6 and 7 were selected inside the network, based on our prior knowledge that the physical area they cover is in the language network, and channels 1 and 12 outside the network with the optode configuration used in the current study. Channel 1 is over the frontal areas while channel 12 covers the temporal area. The choice of these channels as being outside the language area is justified by the fact that they showed no significant activation in response to native language or Spanish [156].

5.2.2 Results

Figure 5.7 shows the HbO₂ signal from channels 7 and 9, the seed, for a typical subject. Qualitatively, the histogram of the phase at different time points for both channels does not show a clear dominant phase range as shown in Figure 5.7-b and Figure 5.7-c. However, the joint distribution histogram shown in Figure 5.7-d has a sharp peak focused around the mean phase difference. This is also evident in the Von Mises distribution function plot derived from estimated parameters in each

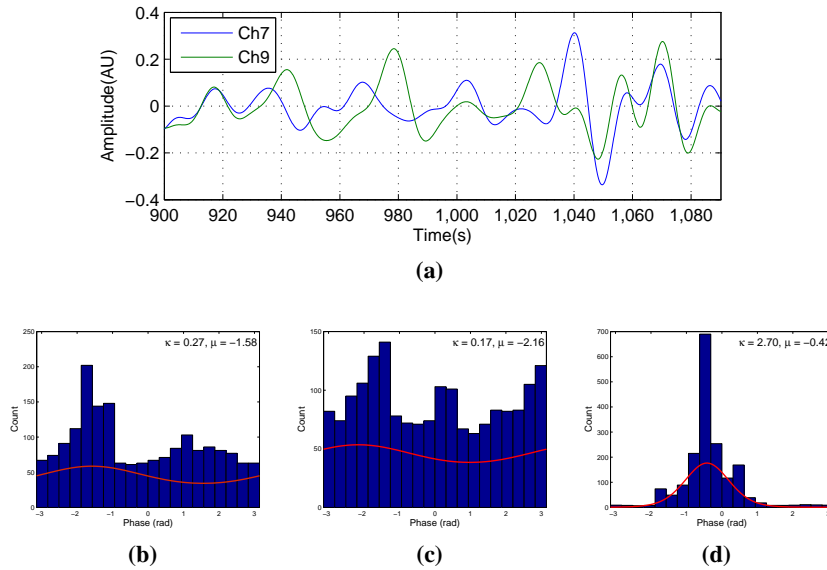


Figure 5.7: Filtered HbO₂ signal recorded from two channels with high degree of connection (a) and the distribution of the phases for each channel (b and c) along with the joint phase distribution (d). The red curve in histograms shows the estimated probability distribution.

case (shown in red). The estimated distribution parameters are also indicated in the figure. In the case of phase histogram for individual channels (Figure 5.7- b and c), the values of estimated κ_{mn} are much smaller than in the conditional distribution (Figure 5.7-d). This indicates a high phase relationship between the two channels and is interpreted as connectivity.

Using the method described earlier, the group level resting state functional connectivity map with channel 9 chosen as the seed channel was derived and is shown in Figure 5.8. The detected network includes the areas known to be associated with language network including the superior temporal gyrus and Broca's area. The maps are also in agreement with those obtained for the language network in adults using correlation based fNIRS connectivity studies [106].

The connectivity maps resulting from the 2 random subgroups are shown in Figure 5.9. The maps for the two subgroup cover similar areas in both hemispheres. The correlation between individual connections in the two subgroups is shown in

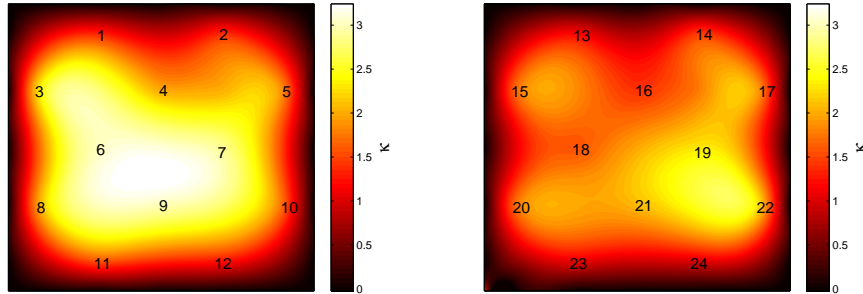


Figure 5.8: Group level RSFC maps with channel 9 in the language area used as the seed channel. Left and right panels correspond to left and right hemispheres.

Table 5.1: Pairwise comparison between selected ROIs inside and outside language network (Tukey’s test).

| Channel Pair | 7-6 | 7-12 | 7-1 | 12-1 |
|---------------------|--------------|-------------|-------------|--------------|
| Mean $\Delta\kappa$ | -0.15 | 1.65 | 1.57 | -0.09 |
| CI (95%) | [-1.43 1.13] | [0.37 2.94] | [0.29 2.85] | [-1.37 1.20] |

Figure 5.10 (Pearson correlation $r=0.6$).

Figure 5.11 shows the results of ROI connectivity analysis where the connection strength between the seed channel and 2 channels in the language area (6 and 7) is compared with that with two channels outside the language system (channels 1 and 12). Analysis of variance indicates significant difference between the connections (ANOVA $p<0.01$) inside and outside the language network. In particular, channels 6 and 7 connections are not different while they are both higher than that of channels 12 and 1 in the temporal and frontal areas, respectively. Results of multiple comparison test are shown in Table 5.1 (Tukey’s test).

The results of the lateralization analysis are shown in Figure 5.12. The average lateralization index is 0.172 and is significantly different from zero (1 sample t-test, $p<0.001$). Here, the lateralization index is also compared for all subjects between the language network and a control case. The control network is created by choosing channel 11 as the seed channel. There is a significant difference in lateralization index between the language and control network (paired t-test $p<0.01$).

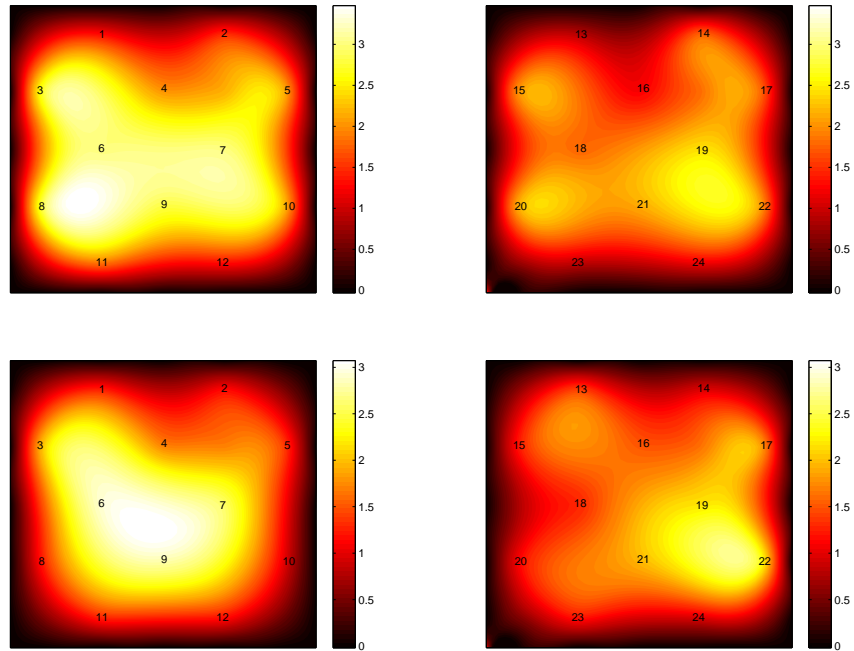


Figure 5.9: The connectivity map for the 2 subgroups with channel 9 used as the seed channel. The top and bottom panels are results of subgroups 1 and 2, respectively. Left and right panels correspond to left and right hemispheres.

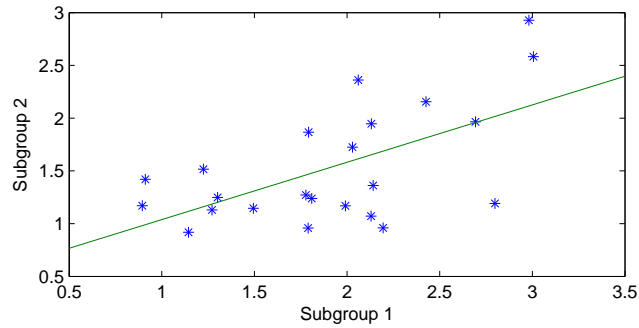


Figure 5.10: Correlation between connection strengths in the two subgroups.

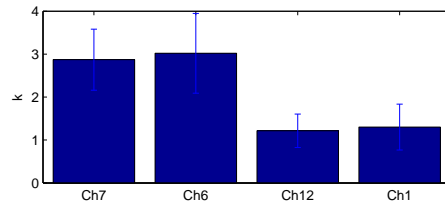


Figure 5.11: ROI connections comparison between language area (represented by channels 7 and 6) and outside language area (represented by channels 1 and 12). The bars indicate the standard error of the mean.

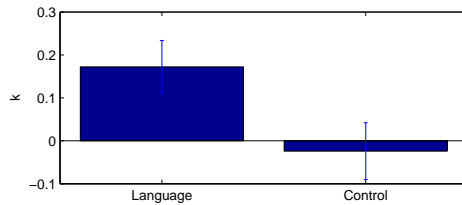


Figure 5.12: Lateralization index for the language network and comparison with control network.

These results suggest left lateralization in the detected language network.

5.3 Discussion and Conclusion

In the first part of this chapter, we used MVAR modeling to identify changes in connection strength in cortical network involved in a speech perception study on neonates. The hemodynamic changes associated with increased neural activity were detected by fNIRS device. The purpose of this pilot study was to detect the changes in functional connectivity in response to exposure to 2 different types of stimuli.

The cortical signals were modeled as a MVAR signal in which AR coefficients represented connection strength at different lags. An overall connection strength measure was defined and was evaluated for every block of the 2 stimulus types. The grand average of blocks in the 3 test subjects indicated strong connections from temporal to frontal areas. Connections were also observed from lower level audio processing areas to higher audio processing levels which in turn mediated the

connection to structural processing regions. It should be noted that this preliminary study has the important limitation of low number of subjects and therefore, the statistical significance of the results could not be verified.

Another observation was the temporal increase in connection strength for one type of stimulus compared to the other across experiment blocks. This is perhaps associated with learning in the time course of experiment. The results of this preliminary study are functionally and neuroanatomically relevant which led us to the next part of this chapter where a different type of connectivity was analyzed on a larger dataset.

We evaluated use of phase synchronization to identify resting state functional connectivity in the language system in infants using fNIRS. We used joint probability distribution of phase between fNIRS channels with a seed channel in the language area to estimate phase relations and identify the language system network. Our results indicate the feasibility of this method in identifying the language system. The connectivity maps are consistent with anatomical cortical connections and are also comparable to those obtained from fMRI functional connectivity studies [163, 164]. The results indicate left hemisphere lateralization of the language network.

Brain networks connectivity reveals information about underlying anatomical areas involved in a particular task. In some disease conditions, changes in cortical connections occurs [149]. Application of connectivity estimating methods to fNIRS enables investigation of such changes in cases where use of fMRI is not possible, such as in infants and extends utilization of fNIRS in wider range of clinical applications.

Use of fNIRS for analysis of functional connectivity offers several advantages over more traditional fMRI based connectivity analysis. Collection of fMRI data from infants and young children under resting condition can be challenging. In contrary, fNIRS is easily applicable to even newborns. Also, in cases where subjects to be tested are immobilized and can not be transferred to an Magnetic Resonance Imaging (MRI) scanner, portable fNIRS systems can replace fMRI for connectivity analysis. One limitation compared to fMRI is the limited penetration depth which means connectivity analysis will be limited to cerebral cortex.

Our results are comparable to similar studies in the literature. In particular

Zhang et al. analyzed RSFC in the language system in adults using fNIRS [106]. Their results indicated significant RSFC between left inferior frontal and superior temporal cortices which are associated with language system [165]. Using fMRI, Fransson et al. studied resting state networks in the infants brain [166]. They observed similar networks in the bilateral temporal/inferior parietal cortex which encompasses primary auditory cortex [166].

The presence of motion artifacts has a significant effect on the connectivity strength results using phase synchrony method presented here. The motion artifact results in in-phase changes across affected channels which may result in stronger phase correlation compared to those resulting from spontaneous neuronal activity. Therefore, care must be taken to ensure segments being processed do not include motion artifacts. Saturated channels or channels that have lost coupling to tissue due to displacement will also have similar effect.

Our fNIRS data was not collected during strict "resting" state. We used continuous blocks of data in which subjects were listening to a non speech audio stimulation. No significant activation compared to baseline was observed on this data and was therefore used as the baseline [156]. Some fMRI studies have followed a similar approach for mapping RSFC. The study by Greicius et al on default mode network in Alzheimer's disease patients for example, was performed during a low demand cognitive task [149, 167]. An alternative approach is to regress out the task evoked response from the data before performing RSFC analysis [168].

The fNIRS signal is known to contain systemic interferences. This includes interference from cardiac pulsation, respiration, cardiovascular autoregulation and heart rate variability. The frequency band for connectivity analysis must be chosen such that it includes the relevant variations caused by the neurovascular coupling while rejecting the frequency bands containing these interferences. The cardiac interference in our study is around 2 Hz and the very low frequency interference (heart rate variability, cardiovascular autoregulation) is around 0.01 Hz. The respiratory fluctuation is around 0.2 Hz. The frequency band we chose for analysis (0.02-0.08 Hz) reduces the effect of these interferences and therefore, connectivity detection as a result of these interferences is less likely.

Bivariate methods in general can result in non existing spurious connections when there is a propagation of information from one channel to others. A pairwise

measure of connectivity will result in detection of connection between all possible connection pairs, ie. direct or indirect. However, since we are only looking to find channels which belong to the same network, use of a bivariate measure of connectivity can be justified. Most methods for functional connectivity mapping in the literature based on fMRI or fNIRS also use seed based methods which is relying on the bivariate concept of finding coherence/correlation between channels with the seed channel [149, 167].

In summary, the results of this work suggest that the proposed method can be used to reveal underlying connectivity patterns of cognitive functions in the resting state through phase relations between hemodynamic changes in different brain regions. The results also indicate a left lateralization in the detected network which suggests the language system may be left-lateralized already in newborns.

Chapter 6

Design and Validation of a Custom fNIRS Device for Monitoring TMS

In this chapter, we describe the design and development of a custom-made continuous wave fNIRS instrument for monitoring the effect of TMS on the brain activation and connectivity.

6.1 Background and Motivation

TMS is a method of stimulating brain using strong magnetic pulses that activate cortical neurons through electromagnetic induction. TMS has been used as an experimental tool for neurophysiological and psychophysiological studies. In order to better understand and investigate the effect of TMS on the brain, neuroimaging techniques have been used concurrently with TMS. This allows studying the changes in hemodynamics and neural activity both in the target brain area as well as the areas closely related to it. However, the strong magnetic pulse produced by the TMS coil introduces serious challenges for common neuroimaging techniques. The optical nature of the NIRS makes it immune to this type of interference and makes it an appropriate tool for monitoring brain hemodynamics during concurrent TMS studies. This type of combined NIRS-TMS study allows one to not only mon-

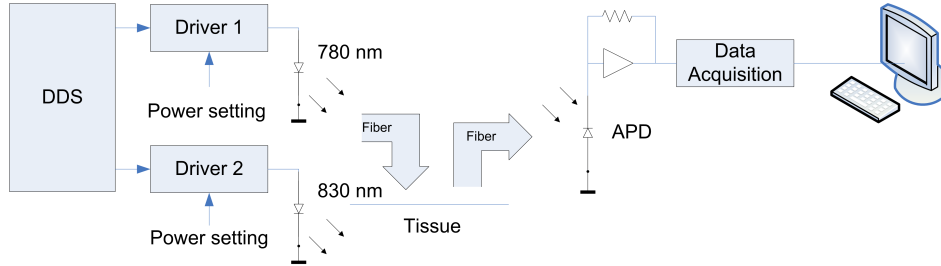


Figure 6.1: Block diagram of the overall fNIRS system.

itor the effect of TMS on the target area, but also to investigate cortical functional connectivity changes in response to stimulation. Such a change in connectivity can occur in a short time scale that does not last long after the stimulation, or in a longer time scale that outlasts the duration of the stimulation.

This chapter describes a custom-made NIRS instrument for monitoring the effect of TMS on brain hemodynamics and neural activity. When combined with the connectivity analysis method described in the previous chapter, the instrument can be used for analyzing the effect of TMS on RSFC with potential application in stroke patients to study both short term and long term effects of TMS on brain networks.

6.2 Instrument Design

Figure 6.1 shows the overall system setup. It consists of two laser sources, delivery fibers, detecting fiber, a photo detector and a Data Acquisition (DAQ) system. Laser sources are amplitude modulated and the modulation signal is driven by a Microcontroller Unit (MCU). The output of the laser sources are launched into two fibers (source optodes). The light is delivered to the target tissue through the source optode. Another fiber collects the light from the tissue and delivers it to a photo detector. The signal from the detector is amplified and sampled by a PC through a DAQ system. A digital lock in amplification scheme is then implemented on the PC to measure attenuation of the diffusively reflected light.

6.2.1 Light Sources

The light source consists of 2 LDs at 780 nm and 830 nm (Sanyo Electric, Japan). LD's emitted light is focused into an angled ferrule of a single mode fiber (5.6 μm core and 125 μm cladding) using an appropriate lens. The diode, lens and fiber ending are enclosed in a housing (Thorlabs Inc., NJ, USA). A standard FC connector is mounted on the free end of fibers for each diode. The connector is attached to a coupler located on the front panel of the device. This allows external access to the laser output. The laser diodes have integrated photodiodes which provide feedback to ensure constant power radiation.

The output power of the LD is controlled by a closed loop control mechanism as shown in Figure 6.2. The maximum LD power is initially set and is then modulated by the input signal. The maximum deliverable current to diodes is also limited by the driver for the overcurrent protection of the LDs.

6.2.2 Source Modulation

Both of the source diodes are amplitude modulated to allow separation of changes in amplitude due to attenuation at the two wavelengths. The sine wave modulating frequencies are chosen as 1 kHz and 1.25 kHz. The frequencies are selected to be high enough to avoid 1/f noise and low enough for the MCU and also for the sampling rate (amount of data that needs to be stored) and also satisfy the conditions for digital lock-in amplification. The higher frequency must not be a multiple of

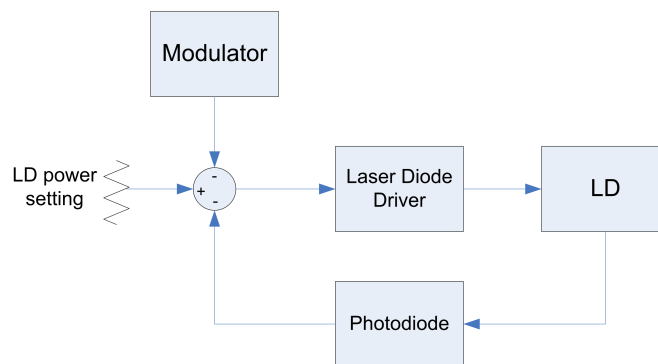


Figure 6.2: Block diagram of the laser diode driver module.

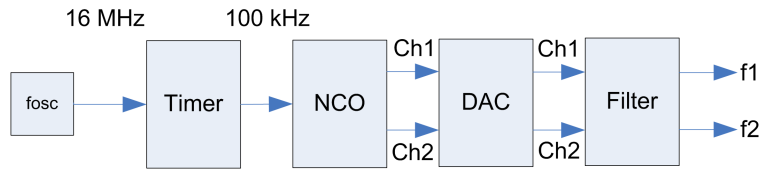


Figure 6.3: Direct digital synthesizer block diagram.

the lower frequency to avoid harmonic interference.

A Direct Digital Synthesis (DDS) scheme is implemented for driving the laser drivers using a 16 bit MCU (MSP430, Texas Instruments, Texas, US). The block diagram of the DDS is shown in figure Figure 6.3. The timer produces an interrupt at 100 kHz rate. The numerically controlled oscillator produces the value of the two sign waves and is triggered by the timer. The values are written to a Digital to Analog Converter (DAC). The output of DAC is filtered to reconstruct the sine waves.

6.2.3 Light Detection

A 1/8" flexible fiber optic light guide collects the light from the tissue and delivers it to the optical detector (Edmund Optics, NJ, USA). The detector is an APD module that includes the APD and the temperature compensated low noise high speed transimpedance amplifier (C5460-01, Hamamatsu Photonics, Japan). The amplifier has an NEP of $0.02 \text{ pW}/\sqrt{\text{Hz}}$ with a gain of 10^8 V/W which provides good sensitivity for the low light levels from the tissue. The analog output of the APD module is sampled at 200 kS/s by a DAQ module (NI USB-6210) controlled by a PC. The results are read by a MATLAB script on a PC and processed in real time.

6.2.4 Digital Lock-in Amplification

A digital lock-in amplification scheme is used to detect the highly attenuated light signal from the tissue and also separate the attenuation of the 780 nm component from that of 830 nm [169]. Digital lock in eliminates the need for high cost lock in amplifiers and provide better stability and ability to measure lower frequencies. A detailed description of the method can be found elsewhere [169]. Here we provide

a brief description of the method and its implementation details.

The modulated signal at the detector can be written as

$$A(n) = A_{dc} + A_{ac} \cos\left(2\pi \frac{f}{f_s} n + \phi\right) \quad (6.1)$$

where A_{dc} is the DC component of the detected signal, A_{ac} is the amplitude of the modulated signal, f , ϕ , f_s are the modulation frequency, signal phase and sampling frequency respectively. To recover the amplitude A_{ac} , a quadrature demodulation scheme as shown in Figure 6.4 can be used. The resulting in-phase (I) and quadrature (Q) components will then be

$$\begin{aligned} I &= A(n) \cos\left(2\pi \frac{f}{f_s} n\right) \\ &= A_{dc} \cos\left(2\pi \frac{f}{f_s} n\right) + \frac{A_{ac}}{2} \cos\left(4\pi \frac{f}{f_s} n + \phi\right) + \frac{A_{ac}}{2} \cos(\phi) \end{aligned} \quad (6.2)$$

and

$$\begin{aligned} Q &= A(n) \sin\left(2\pi \frac{f}{f_s} n\right) \\ &= A_{dc} \sin\left(2\pi \frac{f}{f_s} n\right) + \frac{A_{ac}}{2} \sin\left(4\pi \frac{f}{f_s} n + \phi\right) + \frac{A_{ac}}{2} \sin(\phi) \end{aligned} \quad (6.3)$$

Both operations are performed on an integer number of periods. For 1 cycle,

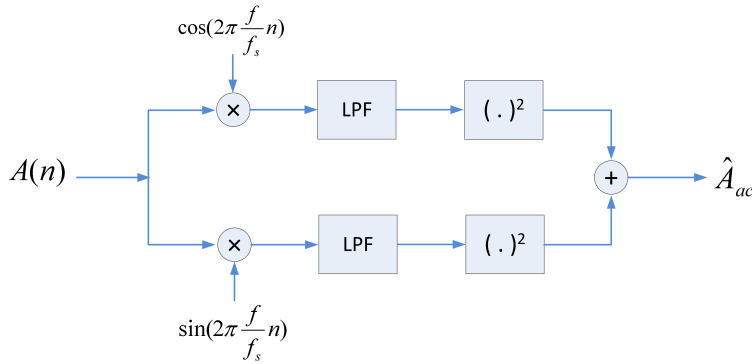


Figure 6.4: In phase-quadrature demodulation scheme.

$N_s = \frac{f_s}{f}$. The amplitude and phase can be recovered from the in-phase and quadrature components by lowpass filtering to eliminate the higher frequency components and using

$$\hat{A}_{ac} = \sqrt{I_{LP}^2 + Q_{LP}^2} \quad (6.4)$$

$$\hat{\phi} = \text{atan} \frac{Q_{LP}}{I_{LP}} \quad (6.5)$$

where I_{LP} and Q_{LP} are the results of lowpass filtering I and Q , \hat{A}_{ac} and $\hat{\phi}$ are the estimated amplitude and phase, respectively.

Since more than 1 modulating frequency is used in our modulation scheme, then due to finite attenuation of filter at higher frequencies, some crosstalk between components will occur. To avoid this, one can choose the modulation frequencies f_m such that they fall on the zeros of the filter [169]. For this purpose, assuming a simple moving average filter we will have

$$h[n] = \frac{1}{N_s} \quad (6.6)$$

where $h[n]$ is the moving average lowpass filter and N_s is the total number of samples collected. This filter has its zeros at $k \frac{f_s}{N_s}$. So by choosing

$$f_m = k \frac{f_s}{N_s} \quad (6.7)$$

the filter response will have zeros at the multiples of modulating frequencies.

With $f_s = 200$ kHz, $f_1 = 1000$ Hz and $f_2 = 1250$ Hz, we have $N_s = 4000$. Given fNIRS overall sampling rate of 10Hz, N_s samples are read from the DAQ every 100 ms and amplitude of the two frequency components are calculated through

$$\begin{bmatrix} I_{f_1} \\ I_{f_2} \end{bmatrix} = \frac{1}{N_s} \begin{bmatrix} \cos \frac{2\pi f_1 0}{f_s} & \cos \frac{2\pi f_1 1}{f_s} & \dots & \cos \frac{2\pi f_1 (N_s-1)}{f_s} \\ \cos \frac{2\pi f_2 0}{f_s} & \cos \frac{2\pi f_2 1}{f_s} & \dots & \cos \frac{2\pi f_2 (N_s-1)}{f_s} \end{bmatrix} \begin{bmatrix} A[1] \\ A[2] \\ \vdots \\ A[N_s] \end{bmatrix} \quad (6.8)$$

and

$$\begin{bmatrix} Q_{f_1} \\ Q_{f_2} \end{bmatrix} = \frac{1}{N_s} \begin{bmatrix} \sin \frac{2\pi f_1 0}{f_s} & \sin \frac{2\pi f_1 1}{f_s} & \dots & \sin \frac{2\pi f_1 (N_s-1)}{f_s} \\ \sin \frac{2\pi f_2 0}{f_s} & \sin \frac{2\pi f_2 1}{f_s} & \dots & \sin \frac{2\pi f_2 (N_s-1)}{f_s} \end{bmatrix} \begin{bmatrix} A[1] \\ A[2] \\ \vdots \\ A[N_s] \end{bmatrix} \quad (6.9)$$

where I_{f_1} , Q_{f_1} , I_{f_2} , Q_{f_2} are the in-phase and quadrature components for f_1 and f_2 , respectively. The amplitude of two wavelength components is derived from

$$\begin{aligned} \hat{A}_{ac}^{f_1} &= 2\sqrt{Q_{f_1}^2 + I_{f_1}^2} \\ \hat{A}_{ac}^{f_2} &= 2\sqrt{Q_{f_2}^2 + I_{f_2}^2} \end{aligned} \quad (6.10)$$

The optical density and concentration changes are calculated from $\hat{A}_{ac}^{f_1}$ and $\hat{A}_{ac}^{f_2}$.

6.2.5 User Interface

The graphical user interface was prepared using MATLAB. The code collects N_s samples from the DAQ card every 100ms. The timing is controlled by a timer object in MATLAB. The samples go through I/Q demodulation according to Equation 6.3 to Equation 6.5. The intensity values are then converted to Optical Density (OD) and then Beer-Lambert law converts OD to concentration changes for HbO₂ and HHb. For functional NIRS studies, the GUI also delivers the stimulations to the subject and adds stimulation markers to the data.

6.3 Performance Evaluation

The system's dark noise was measured by readings obtained by placing the device and receiver optode in a dark room with no light incident on the receiver optode. The RMS value of the noise in this setup was calculated and repeated for a couple of measurements to obtain an estimate of the prototypes noise voltage. This value was calculated to be less than 50 μ V. The NEP was then calculated from dark noise

measurements using

$$P_i = \frac{V_n}{R(\lambda)G} \quad (6.11)$$

where P_i is the incident light equivalent power in W, $R(\lambda)$ is the responsivity of the detector at $\lambda = 780$ and $\lambda = 830$ nm in A/W, G is the amplifier gain and V_n is the noise voltage. With the overall gain ($R(\lambda)G$) of 1.5×10^8 V/W, the NEP is approximately 0.34 pW.

The drift of the measurement was evaluated by continuous recording of data from a phantom using the device for 30 minutes after a warm up period of 1 minute. The aqueous phantom was prepared using the method described in Chapter 4. The phantom scattering and attenuation parameters are chosen to be close to those of the adult head tissue (ie. the scalp and skull with $\mu_a = 0.4 \text{ cm}^{-1}$ and $\mu'_s = 20 \text{ cm}^{-1}$ [170], see Section 6.5 for a discussion). The phantom was made with 20% intra-lipid mixed with ink to obtain desired optical parameters. The difference between the initial and final reading normalized to the initial signal value was recorded as the drift. The device shows 0.1% drift over the period of 30 minutes.

6.4 Validation

We evaluated the performance of the device through in vivo experiments. The experiments included arterial occlusion and isometric contraction of the forearm muscle and the brain response to a motor task test. In all experiments, the collected intensity data was converted to optical density and concentration changes using the MBLL.

6.4.1 Methods

Forearm Muscle Arterial Occlusion Test

In this test, the hemodynamic response to an arterial occlusion in the forearm of a healthy male subject was investigated. This is a common test for validation of custom made NIRS instruments [171, 172]. Arterial occlusion was induced in the forearm by means of a pneumatic pressure cuff. The NIRS optodes were placed on the arm and below the pressure cuff and monitored the oxygenation of the arm

tissue. The cuff was inflated up to 200mm Hg to block any blood in and out flow from the muscle for 1.5 minute. The cuff was then released and the NIRS recording continued for another 2 minutes to monitor tissue oxygenation recovery.

Isometric Contraction

In this test, the Brachioradialis muscle in the forearm was monitored with the NIRS optodes during an isometric contraction experiment. An isometric contraction involves static contraction of a muscle without a change in muscle length. The subject (same as in previous section) forcefully gripped an object for 30 seconds followed by one minute of recovery time.

Motor Task Test

Monitoring brain activation during a motor task is a common method used for evaluating performance of custom made fNIRS instruments [172]. In this test, the fNIRS optodes were placed over the hand area in the left motor cortex near location C3 according to international 10/20 system of a healthy 30 year old right handed male subject [173]. The source and detector fibers were secured using a custom made optode holder consisting of a 3D printed holder (Verowhite polyjet resin) tied with elastic band to the head. The source-detector separation was set to 3 cm. The subject was asked to perform a task of opening and closing his fist at a rate of approximately 3Hz for 30 seconds followed by 30 seconds of rest. The instructions for beginning and ending of the resting/task periods were provided visually through a PC and the timings of the stimulation were recorded along with the fNIRS data.

6.4.2 Results

The result of the arterial occlusion test is shown in Figure 6.5. Black (solid) and magenta (dotted) lines indicate time instants when cuff pressure reached maximum value and when the cuff was released, respectively. As the total occlusion begins, the amount of blood in the tissue remains constant. This is reflected by constant hemoglobin (tHb) detected during the occlusion. However, oxygen is being consumed by the tissue and the HbO_2 is constantly converted to HHb. Therefore, HbO_2 decreases as HHb increases with almost equal changes in the two chromophores'

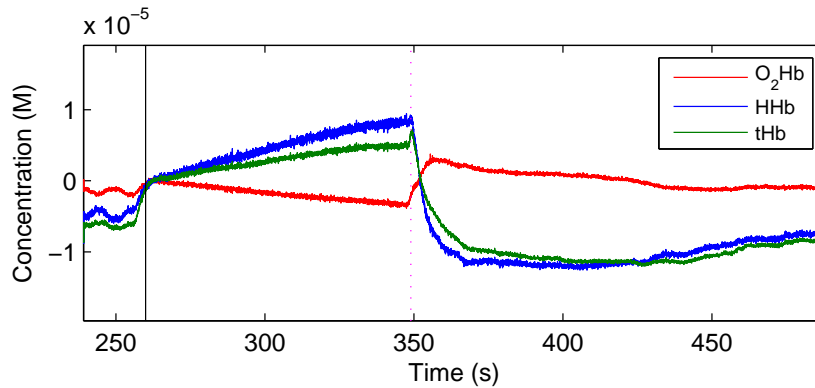


Figure 6.5: Typical HbO₂ and HHb waveforms in the arterial occlusion test. Black (solid) and magenta (dotted) lines indicate time instants when cuff pressure reached maximum value and when the cuff was released, respectively.

concentrations. The gradient of the chromophore changes in this case is proportional to tissue's local oxygen consumption. Once the cuff is released, the changes are reversed. A hyperemic reaction can be observed where due to the auto regulation mechanisms, HbO₂ and HHb overshoot and undershoot beyond their original value once the cuff is released. The two chromophores gradually return to their original values during the recovery period.

Figure 6.6 shows the hemodynamic changes in response to the isometric contraction. Black (solid) and magenta (dotted) lines indicate starting point and the ending point of the contraction, respectively. The contraction results in an increase in blood flow into the muscle along with an increase in muscle oxygen consumption. This can be seen in the figure as an increase in tHb and HHb along with a decrease in HbO₂. Once the object is released and the muscle is relaxed, the changes are reversed (dotted vertical line). The level shifts at the beginning and the end of contraction are the result of the grip motion.

The processing of the motor task fNIRS data was performed using HOMER2 toolbox for MATLAB [174]. Figure 6.7 shows the changes in total hemoglobin concentration in response to the motor task over a period of approximately 5 minutes. The tHb is associated with increased blood flow to the hand area in the brain. The red (solid) lines indicate the beginning of the motor task. In order to measure

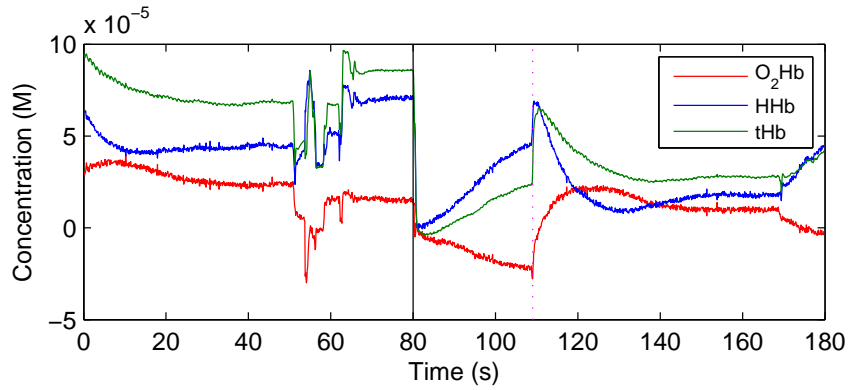


Figure 6.6: Isometric contraction results collected from Brachioradialis muscle in the forearm. Black (solid) line and magenta (dotted) vertical lines indicate beginning and end of contraction, respectively.

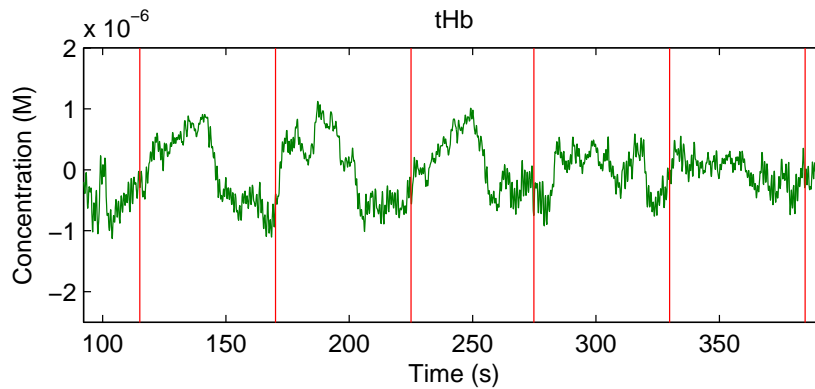


Figure 6.7: Total hemoglobin changes in response to motor activity. The fNIRS optodes were placed over the hand area in the left motor cortex near location C3 according to international 10/20 system of a healthy 30 year old right handed male subject who was asked to perform a task of opening and closing his fist.

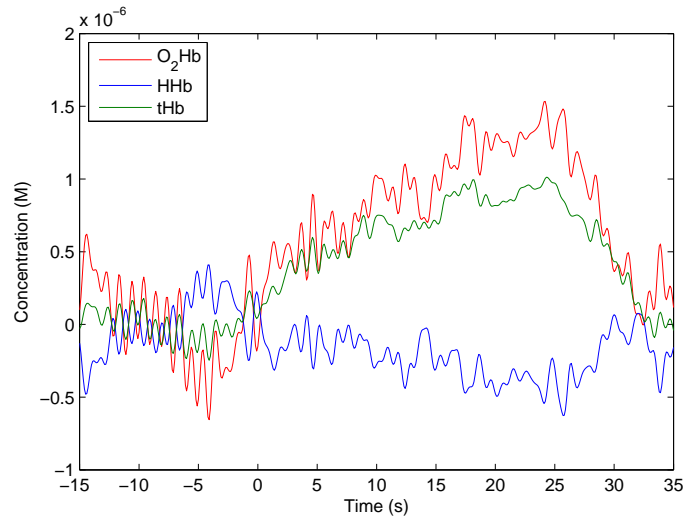


Figure 6.8: Block averaged hemodynamic response.

the hemodynamic response, the signal was block averaged over the stimulation/rest blocks. Figure 6.8 shows the resulting block averaged traces of HbO_2 , HHb and tHb with the stimulation starting time at zero. An increase in the HbO_2 and tHb along with a decrease in HHb is observed which matches the typical hemodynamic response [171, 172].

6.5 Discussion and Conclusion

We described the development of a custom made fNIRS device for future use in TMS experiments to monitor brain tissue hemodynamic changes. The instrument performance was evaluated using in vivo tests commonly used in the literature for evaluation of custom NIRS instruments. The results are comparable to other studies [171, 172] suggesting the instrument is capable of detecting hemodynamic changes in the tissue and in particular, in the brain and can be used for further brain studies involving TMS.

One of the tests we used to evaluate the performance of the custom device was the occlusion test as described in Section 6.4.1. In an occlusion test, it is expected that the blood flow to the tissue is fully blocked resulting in decrease in HbO_2 and

increase in HHb while the tHb stays constant. In our test, however, an increase in tHb is observed as shown in Figure 6.5. This may be due to the fact that the pressure cuff is inflated to 200 mmHg which in this case may have been insufficient to fully block the blood flow. As a result, blood can still reach the tissue and hence the increase in tHb.

The performance of the custom made device was evaluated using a liquid phantom as described in Section 6.3. The optical parameters used in this case may be too high and not a good representation of the overall optical characteristics of an adult head (e.g. compared to [175]). This limitation needs to be addressed in the future for a better characterization of the device performance. Also, as stated in Chapter 4, a solid phantom is preferable and will be considered in the future.

A custom made fNIRS device has multiple advantages for monitoring TMS effect. The sensitivity and custom sampling rate of such a device allows it to potentially measure the fast optical signal [176] which results from small changes in scattering as a result of electrical activity of the neurons. Application of fNIRS systems to monitor fast optical signal during TMS stimulation is new and promising [73]. Additionally, custom devices facilitate temporal and spatial co-registration of NIRS data with TMS stimulations.

Chapter 7

Conclusion and Future Work

Since the first introduction of NIRS by Jobsis, a lot of research has been conducted to apply this promising non-invasive optical method in different clinical applications. Further research and validation in different areas is still required for NIRS to be routinely adopted by clinicians. In this thesis, we attempted to address some of the current issues in NIRS signal processing and applications.

7.1 Motion Artifact Removal from fNIRS

One particular issue of interest in NIRS is the sensitivity of the data to motion artifacts. In Chapter 3, we presented a novel method for removal of motion artifacts from fNIRS data using the discrete wavelet transform. The method relied on the differences between motion-induced patterns and those caused by hemodynamic changes to identify and remove artifacts in the wavelet domain. The method was evaluated using simulated data as well as experimental data in terms of the amount of distortion it introduced in the signal and the reduction in artifact intensity and was shown to be effective in reduction of the motion artifacts. The balance between the amount of artifact reduction and distortion introduction in our method is controlled by the user through a tuning parameter.

Artifact reduction addresses an important issue in fNIRS signal processing. The hemodynamic response is a weak signal whose detection requires averaging over several blocks of stimulation. Often, contamination with motion artifact re-

sults in some of the blocks being excluded from the analysis. In some cases, such as in infant studies for example, it is not possible to collect many data blocks and many subjects do not make it to the end of the experiment as they may become restless and bored. Therefore, it is important to be able to keep as many data blocks as possible for the analysis. Our proposed method can be used as a preprocessing step to reduce the intensity of such contaminations in order to allow keeping more data blocks and improve the contrast to noise ratio in the detected hemodynamic response.

The proposed method of artifact removal can be enhanced further in several ways. One major improvement would be to extend the range of artifact types that can be detected by the method. Our method as described in Chapter 3 targets spike artifacts. However, artifacts resulting in change in baseline are not addressed with this method. Such artifacts could potentially be detected in the wavelet domain using the same principle, but they need to be processed differently.

Also, in some cases, only identification of artifacts or contaminated blocks is required [24]. The method can be further developed to identify such data segments and its performance needs to be evaluated in terms of specificity and sensitivity. Another major potential future direction is to extend the method for real time processing of the data [177]. This can be of significance in wearable NIRS sensors and in particular, can be directly applied to the bladder sensor described in Chapter 4. This requires using methods for estimating the data variance in real time and as the data is being captured.

The performance of this method relies largely on two major factors. One is the capability of the Wavelet transform to map the signal to a space where motion artifacts can be better distinguished from the fNIRS signal. The other is the method used to identify the motion artifact coefficients in the wavelet domain. In our current approach, we assumed a probability distribution for the wavelet coefficients and simply gave the coefficients a score based on their probability of belonging to this distribution. Even though this approach was shown to work satisfactorily, it can be further improved. The problem of identifying the motion induced coefficient can be considered a classification problem and therefore, well known classification methods can be adopted and applied. In particular, one could assume a probability distribution for the motion artifacts coefficients, estimate the parameters of the dis-

tribution and use a Bayesian classifier to classify the coefficient as motion induced or normal. The estimation of the parameters requires use of training data as an added step. This procedure is expected to improve the performance of the method in terms of NMSE introduced in the signal as well as artifact attenuation.

Another alternative approach which is worth comparing to in the future is changing the parameter estimation method for the wavelet coefficients. In our current approach, the main parameter of the probability distribution of wavelet coefficients (i.e. $\hat{\sigma}$) was estimated with MAD using the entire data in each channel which also included the motion artifacts. This was effective as MAD is not sensitive to outliers which in our case, were the motion artifacts. However, if the motion artifacts are frequent and their amplitudes are close to those of fNIRS signal, then they may no longer be considered outliers and the estimate of variance will then be affected. As a result, the performance of the method will decrease. If a long enough artifact-free segment of the data is available, then it can be used to directly estimate the probability distribution of the fNIRS data coefficients and its parameters empirically. This is expected to yield better results as the distribution is no longer affected by motion artifacts. The downside is that a training process with the artifact free data would be involved which adds an extra step to the procedure.

7.2 Wireless NIRS for Monitoring Bladder Contents

We reported design and development of a compact NIRS based wireless wearable sensor for continuous non-invasive monitoring of the bladder with potential application for bladder incontinence patients in Chapter 4. This addresses an important clinical problem in patients with abnormal bladder function. The device was tested in vitro and in vivo as a proof of concept and was shown to be capable of differentiating between empty and full bladder. The results supported the feasibility of this device for the purpose of using it as a warning system that alerts the subjects when their bladder reaches a pre-determined threshold of bladder capacity. Such a device, when fully developed as a wearable warning system, can help patients with urinary retention problem and protect them from renal damage by giving early warning and alarms for voiding their bladder. Currently, there is no alternative method and device for continuous bladder filling detection, a very important clin-

ical issue especially in patients with different types of urinary incontinence and patients with spinal cord injury.

A major limitation of our work on this sensor presented in Chapter 4 is the lack of clinical data for validation. The purpose of our study at this stage was to introduce and verify our method through limited multiple trials to provide evidence of effectiveness of diffuse optics in the form of a wearable sensor for our target application. This method and device need to be further validated in a clinical study with a larger number of subjects as the next step.

Some other technical challenges may limit the applicability of our proposed method. As discussed in Chapter 4, the thickness of the fat layer may affect the effectiveness of our proposed device. The fat layer can cause problems by two mechanisms: 1) by inducing extra attenuation (through both absorption and scattering) and 2) by increasing the distance of the bladder from the tissue surface. One way to overcome the problem of increased distance is increasing the penetration depth by increasing the distance between source and detector. This would require an increase in the power level or using a more sensitive detector. Both of these solutions would also be effective in overcoming the second mechanism which is increased attenuation. Increasing the average power may not be safe and may result in patients' discomfort. However, we can increase the instantaneous power and decrease the sampling rate to keep the average power and SNR the same. Even with this scheme, the maximum practical limitation of the penetration depth for this diffusive method is about 3cm.

Another solution could be a tight fixation which results in mechanically pushing the sensor deeper into the tissue. This can however, cause discomfort for the subject. Changing the wavelength (within the optical wavelengths) does not seem to be effective in improving the penetration depth. Increasing the wavelength decreases scattering, but attenuation due to absorption by water increases significantly. Decreasing the wavelength on the other hand, increases attenuation by absorption by HbO₂ and HHb as well as increased scattering.

The power consumption of the device is another issue that requires further improvement. With the current prototype, the battery life is 45 hours in standby mode, 23 hours when logging onboard without radio transmission and 15 hours with radio transmission. Ideally, a wearable device needs to be recharged as few

times as possible and last at least a day without charging to be practical. The power requirements of the prototype at this stage are not low enough. In particular, since the amplifier and filter are the components consuming most of the standby power, consumption can be significantly reduced by disabling these components in standby mode and only activating them when required. Improving the power consumption during radio transmission is another major future direction to make this device suitable for real life patient monitoring.

The connectivity of this device to a PC has two main advantages. In our proof of principle study, it was necessary for the investigator to be able to visually see the signal as the voiding was happening in order to be able to mark different events (permission to void, start of voiding, end of voiding, potential motion artifacts, etc.). In general, it provides an alternative method for device control as well as data processing and storing. The PC connectivity also serves a further purpose of being used in future developments for clinical remote monitoring. The frequency of bladder filling and voidings which are transferred to the PC can be uploaded to an online database to be accessed by a clinician. These information are meaningful in some pathological conditions. For example in UTI which is a common condition in spinal cord injury patients, the frequency of voiding increases and access to these information collected in normal daily life conditions by the clinician is important in treatment of patients. In such situations, the limited range of connection might limit the usage of wireless link to indoors only. However, the same benefits can be offered by replacing the PC with a smart phone which can provide similar functionalities while being portable and mobile. Development of appropriate applications and database for patient monitoring is a major future improvement for this system.

The actual process of making decisions on bladder fullness and when to trigger the alarm is an important step and the effectiveness of the proposed overall system depends on it. However, this was beyond the scope of our work presented in Chapter 4. The optimal decision making process which requires evaluation of the recordings on a case by case basis by a clinician who factors in parameters such as bladder size, anatomy, level of injury, etc. is part of the future work on this method.

The drift in the output of the device can potentially cause problems in long term patient monitoring as the accumulated drift may be mistaken for bladder fill-

ing. The most important cause of the drift as discussed in Chapter 4 is the slight temperature rise caused by LED operation. This rise leads to slight changes (drift) in the LED output intensity over time. This has been reported to be present in other works on NIRS systems [171, 172]. This limitation needs to be addressed for practical application of our method. The solution suggested in Chapter 4 was to reset the device at voiding times (alarm) to prevent the error from accumulating. A better solution could be to use LEDs with photodetector integrated to control the output power in a closed loop system. Such LEDs could be selected to also include 2 more wavelengths for detection of HbO₂ and HHb in order to estimate changes from these chromophores as well. This could help minimize the contribution of these chromophores to the detected signal and minimize the systemic interferences as discussed in Chapter 4.

Another major limitation of the method presented in Chapter 4 is the large variations in the initial value of optical attenuation which is caused by the sensitivity of the device to unknown changes in attenuation caused by parameters such as sensor geometry, coupling and tissue scattering. These parameters vary from one experiment to another or when the sensor is relocated on the tissue. Therefore, in order to develop a fully practical and reliable system for continuous monitoring of the bladder, it is necessary to address this issue so that a threshold of bladder capacity can be properly established and the measured attenuation can be compared to this threshold. Therefore, a more robust approach such as a multidistance method which is less sensitive to changes in coupling needs to be considered for this method in the future [138, 139].

7.3 fNIRS Connectivity

In Chapter 5 we used fNIRS along with phase analysis to identify resting state functional connectivity patterns in language system. Use of phase relation between hemodynamic changes in fNIRS data in resting state is a novel contribution of this work. The agreement between results presented with those obtained from fNIRS data in similar studies with different methods and different subject population suggests feasibility of the proposed approach.

As stated earlier, the data used in Chapter 5 was not collected in "strict" resting

state, meaning that the subjects were not in the ideal state of rest with no particular cognitive or sensorimotor task. It is not uncommon in the literature to use light cognitive task as a substitute for resting state ([149, 167]). Our data which was collected during stimulation with Silbo-Gomero language to which infants showed no response, can be considered a very low demand task and therefore, the results are still valid. However, investigating the alternative approach of absolute resting state data and comparing the results to those obtained in Chapter 5 would be of interest. This requires collection of fNIRS data from infants without any particular stimulation. The results could confirm the degree of validity of the assumption of resting state for our low cognitive stimulation condition.

An interesting question that can possibly be answered using this approach is how brain networks develop with age. This is a relevant question in developmental neuroscience [178] and fNIRS offers advantages that make it ideal for studies that involve collecting data from young infants over other methods such as fMRI. We have already applied our phase-based fNIRS connectivity analysis for identifying language network in newborn infants. A future study on older subjects to identify the same network and changes in the network during brain development could reveal very valuable information. If fNIRS connectivity is validated as a clinical method for evaluating brain network connectivity patterns, it can potentially be used for example to identify brain network developmental problems in infants long before the symptoms can be observed.

One potential challenge in the use of the proposed method as described in Chapter 5 for monitoring cortical network development is the choice of the seed channel. The seed channel in our method was chosen as the channel inside the language network which showed high activation in language tasks. To ensure changes in the shape and location of the network with age are taken into account, one needs to precede the RSFC analysis with a localizer task to identify a proper seed channel.

Another possible future direction is using NIRS based functional connectivity in a clinical study to validate its capability in discriminating between health and disease in conditions such as stroke, depression or autism.

Using the joint probability distribution function of the phase results in estimation of phase dependence between the two channels along with the preferred phase difference. In the method presented in Chapter 5, only the first parameter was used.

However, the second parameter could contain significant information as well. The phase difference between HbO_2 and HHb has been shown to convey information that discriminates between different states as well as health and disease in particular conditions [179, 180]. Applying similar approach to connectivity with our proposed method in the future can provide further connectivity information.

As discussed in Chapter 5, HbO_2 is more sensitive to regional blood flow changes and was therefore used for the connectivity analysis. However, comparison of the results with those obtained by HHb could be insightful as to whether they detect similar networks and whether this difference is only attributed to higher noise level in HHb.

We discussed the issue of non existing spurious connections as a result of inherent shortcoming of bivariate methods when there is a propagation of information from one channel to others. Even though this does not affect the detection of networks as explained in Chapter 5, applying the same analysis using an equivalent multivariate method could reveal further information. A similar approach has been applied to EEG and could be adopted to fNIRS similar to what was used in Chapter 5.

7.4 Custom-made fNIRS Device for TMS Monitoring

In Chapter 6, we described the development and validation of a custom made fNIRS system for monitoring the effect of the TMS on brain activation and connectivity. Even though commercial NIRS devices are available for different types of studies, developing custom made devices for specific purposes is common [171, 172, 181]. The functionality of the device was verified in Chapter 6 using tests which are well documented in the literature. In order to further validate the device and test the hypothesis that brain activation in the motor and visual cortices can be detected by this device, we will be using it in the practice of a novel unilateral joystick based tracking task [182]. This task has been used by our collaborators for different studies in the past research during fMRI. This past work assures us that significant change in both brain function and behavior occur during the practice of this task [183]. In addition, the availability of fMRI data during task performance makes comparison of the data from the device with those from fMRI easier.

One major future improvement is integrating the TMS 3D stimulation localizing system into fNIRS optodes so that fNIRS monitoring location and TMS stimulation location can both be registered on an anatomical MRI image. Currently, 3D object trackers are used for co-registering TMS stimulation target with an anatomical MRI image of the subject's brain. A similar approach can be used to track fNIRS probe on the head to ensure correct spatial relation between the two.

rTMS has been shown to be effective in improving performance in motor skill practice. Monitoring the accumulating effect of TMS on brain hemodynamics can be beneficial in understanding the mechanism of effect of rTMS involved in this process. Moreover, comparison of neural activation while practicing a motor skill task before and after rTMS stimulation session can help evaluate the effect of rTMS on the brain in a qualitative manner. In particular, the fNIRS data collected in this way can also be used in combination with the connectivity analysis method described in Chapter 5 to evaluate brain connectivity changes following the TMS stimulation.

Investigating the effect of rTMS on the brain using the fast optical signal is a recent subject of interest [73]. This type of optical signal has the advantage of a much higher temporal resolution compared to that of hemodynamic response and is therefore capable of detecting rTMS-induced changes in a much shorter time scale. Even though the capabilities of the device described in Chapter 6 for detecting fast optical signal was not demonstrated in this thesis, this device could potentially be used for this purpose using minimum changes. Validation and application of this device in an rTMS study for detecting fast optical signal is in the scope of our future studies.

Bibliography

- [1] B. Molavi, G. A. Dumont, and B. Shadgan. Motion artifact removal from muscle NIR Spectroscopy measurements. In *CCECE 2010*, pages 1–4, May 2010. → pages iv, v
- [2] B. Molavi and G. A. Dumont. Wavelet based motion artifact removal for Functional Near Infrared Spectroscopy. *Annual International Conference of the IEEE Engineering in Medicine and Biology Society*, pages 5–8, 2010. → pages iv, v, 32
- [3] B. Molavi, G. A. Dumont, B. Shadgan, and A. J. Macnab. Attenuation of motion artifact in near infrared spectroscopy signals using a wavelet based method. In *Proceedings of SPIE 7890*, page 78900M, February 2011. → pages iv, v, 32
- [4] B. Molavi and G. A. Dumont. Wavelet-based motion artifact removal for functional near-infrared spectroscopy. *Physiological measurement*, 33(2):259–70, February 2012. → pages iv, v, 32, 51
- [5] B. Molavi, J. Gervain, and G. A. Dumont. Estimating cortical connectivity in functional near infrared spectroscopy using multivariate autoregressive modeling. In *Annual International Conference of the IEEE Engineering in Medicine and Biology Society*, pages 2334–2337, January 2011. → pages iv, v, 72
- [6] B. Molavi, J. Gervain, G. A. Dumont, and H. A. Noubari. Functional connectivity analysis of cortical networks in Functional Near Infrared Spectroscopy using phase synchronization. In *Annual International Conference of the IEEE Engineering in Medicine and Biology Society*, pages 5182–5185, August 2012. → pages iv, v
- [7] F. F. Jöbsis. Noninvasive, infrared monitoring of cerebral and myocardial oxygen sufficiency and circulatory parameters. *Science*, 198(4323):1264–1267, December 1977. → pages 1

BIBLIOGRAPHY

- [8] B. Shadgan, J. A. Guenette, A. W. Sheel, and W. D. Reid. Sternocleidomastoid muscle deoxygenation in response to incremental inspiratory threshold loading measured by near infrared spectroscopy. *Respiratory physiology & neurobiology*, 178(2):202–209, September 2011. → pages 2
- [9] M. Ferrari, T. Binzoni, and V. Quaresima. Oxidative metabolism in muscle. *Philosophical transactions of the Royal Society of London. Series B, Biological sciences*, 352(1354):677–683, 1997. → pages 2
- [10] P. M. Arenth, J. H. Ricker, and M. T. Schultheis. Applications of functional near-infrared spectroscopy (fnirs) to neurorehabilitation of cognitive disabilities. *The Clinical neuropsychologist*, 21(1):38–57, Jan 2007. → pages 2
- [11] S. Coyle, T. Ward, C. Markham, and G. McDarby. On the suitability of near-infrared (nir) systems for next-generation brain-computer interfaces. *Physiological Measurement*, 25(4):815–822, Aug 2004. → pages 2
- [12] R. Choe, A. Corlu, K. Lee, T. Durduran, S. D. Konecky, M. Grosicka-Koptyra, S. R. Arridge, B. J. Czerniecki, D. L. Fraker, A. DeMichele, B. Chance, M. A. Rosen, and A. G. Yodh. Diffuse optical tomography of breast cancer during neoadjuvant chemotherapy: a case study with comparison to MRI. *Medical physics*, 32:1128–1139, April 2005. → pages 2
- [13] F. Orihuela-Espina, D. R. Leff, D. R. C. James, A. W. Darzi, and G. Z. Yang. Quality control and assurance in functional near infrared spectroscopy (fNIRS) experimentation. *Physics in medicine and biology*, 55(13):3701–3724, July 2010. → pages 3
- [14] S. Huettel, A. W. Song, and G. McCarthy. *Functional magnetic resonance imaging*. Sinauer Associates Publishers, Sunderland Mass., 2004. → pages 3
- [15] G. Strangman, J. P. Culver, J. H. Thompson, and D. A. Boas. A Quantitative Comparison of Simultaneous BOLD fMRI and NIRS Recordings during Functional Brain Activation. *NeuroImage*, 17(2):719–731, October 2002. → pages 3
- [16] D. T. Delpy, M. Cope, P. Van Der Zee, S. Arridge, S. Wray, and J. Wyatt. Estimation of optical pathlength through tissue from direct time of flight

BIBLIOGRAPHY

- measurement. *Physics in medicine and biology*, 33(12):1433–1442, December 1988. → pages 4, 53
- [17] T. Durduran, R. Choe, W. B. Baker, and A. G. Yodh. Diffuse optics for tissue monitoring and tomography. *Reports on Progress in Physics*, 73(7):076701, July 2010. → pages 6, 7, 11, 12
- [18] C. HOCK, K. VILLRINGER, F. MÜLLER-SPAHN, M. HOFMANN, S. SCHUH-HOFER, H. HEEKEREN, R. WENZEL, U. DIRNAGL, and A. VILLRINGER. Near Infrared Spectroscopy in the Diagnosis of Alzheimer’s Disease. *Annals of the New York Academy of Sciences*, 777(1):22–29, January 1996. → pages 8
- [19] C. Hock, K. Villringer, F. Müller-Spahn, R. Wenzel, H. Heekeren, S. Schuh-Hofer, M. Hofmann, S. Minoshima, M. Schwaiger, U. Dirnagl, and A. Villringer. Decrease in parietal cerebral hemoglobin oxygenation during performance of a verbal fluency task in patients with Alzheimer’s disease monitored by means of near-infrared spectroscopy (NIRS) correlation with simultaneous rCBF-PET measurements. *Brain Research*, 755(2):293–303, May 1997. → pages 8
- [20] F. Okada, Y. Tokumitsu, Y. Hoshi, and M. Tamura. Impaired interhemispheric integration in brain oxygenation and hemodynamics in schizophrenia. *European archives of psychiatry and clinical neuroscience*, 244(1):17–25, 1994. → pages 8
- [21] A. J. Fallgatter and W. K. Strik. Reduced frontal functional asymmetry in schizophrenia during a cued continuous performance test assessed with near-infrared spectroscopy. *Schizophrenia bulletin*, 26(4):913–919, 2000. → pages 8
- [22] K. Matsuo, T. Kato, M. Fukuda, and N. Kato. Alteration of hemoglobin oxygenation in the frontal region in elderly depressed patients as measured by near-infrared spectroscopy. *The Journal of neuropsychiatry and clinical neurosciences*, 12(4):465–471, 2000. → pages 8
- [23] A. P. Gibson, J. C. Hebden, and S. R. Arridge. Recent advances in diffuse optical imaging. *Physics in Medicine and Biology*, 50(4):R1–R43, 2005. → pages 8, 9
- [24] J. Gervain, F. Macagno, S. Cogoi, M. Peña, and J. Mehler. The neonate brain detects speech structure. *Proceedings of the National Academy of*

BIBLIOGRAPHY

- Sciences of the United States of America*, 105(37):14222–14227, September 2008. → pages 8, 16, 75, 76, 77, 86, 109
- [25] J. H. Meek, M. Firbank, C. E. Elwell, J. Atkinson, O. Braddick, and J. S. Wyatt. Regional hemodynamic responses to visual stimulation in awake infants. *Pediatric research*, 43(6):840–843, 1998. → pages 8
- [26] P. Zaramella, F. Freato, A. Amigoni, S. Salvadori, P. Marangoni, A. Supppei, B. Schiavo, and L. Chiandetti. Brain auditory activation measured by near-infrared spectroscopy (nirs) in neonates. *Pediatric research*, 49(2):213–219, Feb 2001. → pages 8
- [27] L. Stothers, B. Shadgan, and A. Macnab. Urological applications of near infrared spectroscopy. *The Canadian journal of urology*, 15(6):4399–4409, December 2008. → pages 9, 23, 69
- [28] M. C. van der Sluijs. New and highly sensitive continuous-wave near-infrared spectrophotometer with multiple detectors. In *Proceedings of SPIE*, volume 3194, pages 63–72. SPIE, 1998. → pages 9
- [29] M. Cope and D. T. Delpy. System for long-term measurement of cerebral blood and tissue oxygenation on newborn infants by near infrared transillumination. *Medical & Biological Engineering & Computing*, 26(3):289–294, 1988. → pages 76
- [30] M. A. Franceschini, V. Toronov, M. Filiaci, E. Gratton, and S. Fantini. On-line optical imaging of the human brain with 160-ms temporal resolution. *Optics Express*, 6(3):49–57, 2000. → pages
- [31] C. D. Gomersall, P. L. Leung, T. Gin, G. M. Joynt, R. J. Young, W. S. Poon, and T. E. Oh. A comparison of the hamamatsu niro 500 and the invos 3100 near-infrared spectrophotometers. *Anaesthesia and Intensive Care*, 26(5):548–557, Oct 1998. → pages
- [32] F. Kawaguchi, N. Ichikawa, N. Fujiwara, Y. Yamashita, and S. Kawasaki. Clinically available optical topography system. *Hitachi Reveiw*, 50(1), 2001. → pages
- [33] V. Quaresima, S. Sacco, R. Totaro, and M. Ferrari. Noninvasive measurement of cerebral hemoglobin oxygen saturation using two near infrared spectroscopy approaches. *Journal of biomedical optics*, 5(2):201–205, April 2000. → pages 9

BIBLIOGRAPHY

- [34] D. Grosenick, H. Wabnitz, H. H. Rinneberg, K. T. Moesta, and P. M. Schlag. Development of a Time-Domain Optical Mammograph and First in vivo Applications. *Applied Optics*, 38(13):2927, May 1999. → pages 9
- [35] N. L. Everdell, a. P. Gibson, I. D. C. Tullis, T. Vaithianathan, J. C. Hebden, and D. T. Delpy. A frequency multiplexed near-infrared topography system for imaging functional activation in the brain. *Review of Scientific Instruments*, 76(9):093705, 2005. → pages
- [36] V. Ntziachristos, X. Ma, A. G. Yodh, and B. Chance. Multichannel photon counting instrument for spatially resolved near infrared spectroscopy. *Review of Scientific Instruments*, 70(1):193–201, 1999. → pages
- [37] D. Haensse, P. Szabo, D. Brown, J.-C. Fauchère, P. Niederer, H.-u. Bucher, and M. Wolf. A new multichannel near infrared spectrophotometry system for functional studies of the brain in adults and neonates. *Optics Express*, 13(12):4525, 2005. → pages
- [38] A. Siegel, J. J. Marota, and D. Boas. Design and evaluation of a continuous-wave diffuse optical tomography system. *Optics Express*, 4(8):287–298, 1999. → pages 9
- [39] M. Wolf, M. Ferrari, and V. Quaresima. Progress of near-infrared spectroscopy and topography for brain and muscle clinical applications. *Journal of biomedical optics*, 12(6):062104, 2007. → pages 9, 12
- [40] M. Ferrari, L. Mottola, and V. Quaresima. Principles, techniques, and limitations of near infrared spectroscopy. *Canadian journal of applied physiology*, 29(4):463–487, August 2004. → pages 9, 15
- [41] R. D. Frostig. *In vivo optical imaging of brain function*. CRC Press, Boca Raton, 2002. → pages 9
- [42] M. Fabiani, D. D. Schmorrow, and G. Gratton. Optical imaging of the intact human brain [guest editorial]. *Engineering in Medicine and Biology Magazine, IEEE*, 26(4):14–16, 2007. → pages 10
- [43] G. Gratton, C. R. Brumback, B. A. Gordon, M. A. Pearson, K. A. Low, and M. Fabiani. Effects of measurement method, wavelength, and source-detector distance on the fast optical signal. *NeuroImage*, 32(4):1576–1590, 2006. → pages 10
- [44] E. L. Maclin, G. Gratton, and M. Fabiani. Optimum filtering for eros measurements. *Psychophysiology*, 40(4):542–547, Jul 2003. → pages

BIBLIOGRAPHY

- [45] E. L. Maclin, K. A. Low, J. J. Sable, M. Fabiani, and G. Gratton. The event-related optical signal to electrical stimulation of the median nerve. *NeuroImage*, 21(4):1798–1804, 2004. → pages 10
- [46] S. J. Matcher, P. J. Kirkpatrick, K. Nahid, M. Cope, and D. T. Delpy. Absolute quantification methods in tissue near infrared spectroscopy. In *Proc. SPIE 2389*, pages 486–495, May 1995. → pages 10
- [47] H. Sato, M. Kiguchi, F. Kawaguchi, and A. Maki. Practicality of wavelength selection to improve signal-to-noise ratio in near-infrared spectroscopy. *NeuroImage*, 21(4):1554–1562, 2004. → pages 11
- [48] Y. Yamashita, A. Maki, and H. Koizumi. Wavelength dependence of the precision of noninvasive optical measurement of oxy-, deoxy-, and total-hemoglobin concentration. *Medical Physics*, 28(6):1108–1114, 2001. → pages 11
- [49] G. Strangman. Factors affecting the accuracy of near-infrared spectroscopy concentration calculations for focal changes in oxygenation parameters. *NeuroImage*, 18(4):865–879, 2003. → pages
- [50] D. A. Boas, A. M. Dale, and M. A. Franceschini. Diffuse optical imaging of brain activation: approaches to optimizing image sensitivity, resolution, and accuracy. *NeuroImage*, 23:S275–S288, January 2004. → pages 11
- [51] A. Corlu, R. Choe, T. Durduran, K. Lee, M. Schweiger, S. R. Arridge, E. M. C. Hillman, and A. G. Yodh. Diffuse optical tomography with spectral constraints and wavelength optimization. *Applied optics*, 44(11):2082–2093, April 2005. → pages 11
- [52] A. Corlu, T. Durduran, R. Choe, M. Schweiger, E. M. C. Hillman, S. R. Arridge, and A. G. Yodh. Uniqueness and wavelength optimization in continuous-wave multispectral diffuse optical tomography. *Optics letters*, 28(23):2339–2341, December 2003. → pages 11
- [53] Safety of laser products - Part 1: Equipment classification and requirements. Technical report, International Electrotechnical Commission, 2007. → pages 11
- [54] Photobiological safety of lamps and lamp systems. Technical report, International Electrotechnical Commission, 2006. → pages 11

BIBLIOGRAPHY

- [55] A. Bozkurt and B. Onaral. Safety assessment of near infrared light emitting diodes for diffuse optical measurements. *Biomedical engineering online*, 3(1):9, March 2004. → pages 11
- [56] H. Koizumi, T. Yamamoto, A. Maki, Y. Yamashita, H. Sato, H. Kawaguchi, and N. Ichikawa. Optical topography: practical problems and new applications. *Applied optics*, 42(16):3054–3062, June 2003. → pages 11
- [57] J. Gervain, J. Mehler, J. F. Werker, C. a. Nelson, G. Csibra, S. Lloyd-Fox, M. Shukla, and R. N. Aslin. Near-infrared spectroscopy: a report from the McDonnell infant methodology consortium. *Developmental cognitive neuroscience*, 1(1):22–46, January 2011. → pages 11, 13, 58
- [58] G. Strangman, D. A. Boas, and J. P. Sutton. Non-invasive neuroimaging using near-infrared light. *Biological psychiatry*, 52(7):679–693, October 2002. → pages 12, 13
- [59] A. P. Gibson, J. C. Hebden, and S. R. Arridge. Recent advances in diffuse optical imaging. *Physics in Medicine and Biology*, 50(4):R1–R43, 2005. → pages 12
- [60] M. S. Patterson, S. Andersson-Engels, B. C. Wilson, and E. K. Osei. Absorption spectroscopy in tissue-simulating materials: a theoretical and experimental study of photon paths. *Applied optics*, 34(1):22–30, January 1995. → pages 12
- [61] S. Lloyd-Fox, A. Blasi, and C. E. Elwell. Illuminating the developing brain: the past, present and future of functional near infrared spectroscopy. *Neuroscience and biobehavioral reviews*, 34(3):269–284, March 2010. → pages 12, 13
- [62] V. Toronov, M. A. Franceschini, M. Filiaci, S. Fantini, M. Wolf, A. Michalos, and E. Gratton. Near-infrared study of fluctuations in cerebral hemodynamics during rest and motor stimulation: temporal analysis and spatial mapping. *Medical physics*, 27(4):801–815, April 2000. → pages 14
- [63] F. Robertson, T. Douglas, and E. Meintjes. Motion Artefact Removal for Functional Near Infrared Spectroscopy: a Comparison of Methods. *IEEE Transactions on Biomedical Engineering*, 57(6):1377–1387, 2010. → pages 15, 21, 23, 48, 49
- [64] Y. Zhang, D. H. Brooks, M. A. Franceschini, and D. A. Boas. Eigenvector-based spatial filtering for reduction of physiological

BIBLIOGRAPHY

- interference in diffuse optical imaging. *Journal of biomedical optics*, 10(1):11014, 2005. → pages 22
- [65] M. Izzetoglu, P. Chitrapu, S. Bunce, and B. Onaral. Motion artifact cancellation in NIR spectroscopy using discrete Kalman filtering. *Biomedical engineering online*, 9(1):16, January 2010. → pages 22, 48, 51
- [66] F. Scholkmann, S. Spichtig, T. Muehlemann, and M. Wolf. How to detect and reduce movement artifacts in near-infrared imaging using moving standard deviation and spline interpolation. *Physiological measurement*, 31(5):649–662, May 2010. → pages 22, 51
- [67] X. Cui, S. Bray, and A. L. Reiss. Functional near infrared spectroscopy (NIRS) signal improvement based on negative correlation between oxygenated and deoxygenated hemoglobin dynamics. *NeuroImage*, 49(4):3039–3046, February 2010. → pages 15, 22, 51
- [68] P. Petrican and M. A. Sawan. Design of a miniaturized ultrasonic bladder volume monitor and subsequent preliminary evaluation on 41 enuretic patients. *IEEE transactions on rehabilitation engineering*, 6(1):66–74, March 1998. → pages 16, 25, 54
- [69] J. Gervain and J. F. Werker. Prosody cues word order in 7-month-old bilingual infants. *Nature communications*, 4:1490, January 2013. → pages 16
- [70] L. May, K. Byers-Heinlein, J. Gervain, and J. F. Werker. Language and the newborn brain: does prenatal language experience shape the neonate neural response to speech? *Frontiers in psychology*, 2:222, January 2011. → pages 16
- [71] Pitch perfect. *The Economist*, 2013. → pages 16
- [72] G. Gratton and M. Fabiani. The event-related optical signal (EROS) in visual cortex: replicability, consistency, localization, and resolution. *Psychophysiology*, 40(4):561–71, July 2003. → pages 17
- [73] N. A. Parks, E. L. Maclin, K. A. Low, D. M. Beck, M. Fabiani, and G. Gratton. Examining cortical dynamics and connectivity with simultaneous single-pulse transcranial magnetic stimulation and fast optical imaging. *NeuroImage*, 59(3):2504–2510, February 2012. → pages 17, 30, 31, 107, 116

BIBLIOGRAPHY

- [74] R. J. Cooper, J. Selb, L. Gagnon, D. Phillip, H. W. Schytz, H. K. Iversen, M. Ashina, and D. A. Boas. A systematic comparison of motion artifact correction techniques for functional near-infrared spectroscopy. *Frontiers in neuroscience*, 6(147), January 2012. → pages 18, 22, 23, 32, 51
- [75] S. Brigadoi, L. Ceccherini, S. Cutini, F. Scarpa, P. Scatturin, J. Selb, L. Gagnon, D. A. Boas, and R. J. Cooper. Motion artifacts in functional near-infrared spectroscopy: A comparison of motion correction techniques applied to real cognitive data. *NeuroImage*, April 2013. → pages 18, 23, 32, 49, 50, 51
- [76] M. Izzetoglu, A. Devaraj, S. Bunce, and B. Onaral. Motion artifact cancellation in NIR spectroscopy using wiener filtering. *IEEE Transactions on Biomedical Engineering*, 52(5):934–938, 2005. → pages 21, 22, 47, 48
- [77] J. Virtanen, T. Noponen, K. Kotilahti, J. Virtanen, and R. J. Ilmoniemi. Accelerometer-based method for correcting signal baseline changes caused by motion artifacts in medical near-infrared spectroscopy. *Journal of biomedical optics*, 16(8):087005, August 2011. → pages 21
- [78] A. Blasi, D. Phillips, S. Lloyd-Fox, P. H. Koh, and C. E. Elwell. Automatic detection of motion artifacts in infant functional optical topography studies. *Advances in experimental medicine and biology*, 662:279–284, January 2010. → pages 21
- [79] Q. Zhang, G. E. Strangman, and G. Ganis. Adaptive filtering to reduce global interference in non-invasive NIRS measures of brain activation: how well and when does it work? *NeuroImage*, 45(3):788–794, April 2009. → pages 21
- [80] Y. Zhang, J. Sun, and P. Rolfe. Reduction of global interference in functional multidistance near-infrared spectroscopy using empirical mode decomposition and recursive least squares: a Monte Carlo study. *Journal of the European Optical Society: Rapid Publications*, 6:11033, June 2011. → pages 21
- [81] T. Nakano, H. Watanabe, F. Homae, and G. Taga. Prefrontal cortical involvement in young infants’ analysis of novelty. *Cerebral cortex*, 19(2):455–463, February 2009. → pages 21
- [82] M. Peña, A. Maki, D. Kovacić, G. Dehaene-Lambertz, H. Koizumi, F. Bouquet, and J. Mehler. Sounds and silence: an optical topography study of language recognition at birth. *Proceedings of the National Academy of*

BIBLIOGRAPHY

- Sciences of the United States of America*, 100(20):11702–11705, September 2003. → pages 22, 40
- [83] J. Gervain, F. Macagno, S. Cogoi, M. Peña, and J. Mehler. The neonate brain detects speech structure. *Proceedings of the National Academy of Sciences of the United States of America*, 105(37):14222–14227, September 2008. → pages 22, 40
- [84] B. Lee, J. Han, H. J. Baek, J. H. Shin, K. S. Park, and W. J. Yi. Improved elimination of motion artifacts from a photoplethysmographic signal using a Kalman smoother with simultaneous accelerometry. *Physiological measurement*, 31(12):1585–1603, October 2010. → pages 22, 48
- [85] H. Sato, N. Tanaka, M. Uchida, Y. Hirabayashi, M. Kanai, T. Ashida, I. Konishi, and A. Maki. Wavelet analysis for detecting body-movement artifacts in optical topography signals. *NeuroImage*, 33(2):580–587, November 2006. → pages 23, 47, 49
- [86] K. E. Jang, S. Tak, J. Jung, J. Jang, Y. Jeong, and J. C. Ye. Wavelet minimum description length detrending for near-infrared spectroscopy. *Journal of biomedical optics*, 14(3):034004, 2009. → pages 23
- [87] A. Macnab and B. Shadgan. Biomedical applications of wireless continuous wave near infrared spectroscopy. *Biomedical Spectroscopy and Imaging*, 1(3):205–222, 2012. → pages 23, 54
- [88] A. Macnab, B. Shadgan, K. Afshar, and L. Stothers. Near-Infrared Spectroscopy of the Bladder: New Parameters for Evaluating Voiding Dysfunction. *International Journal of Spectroscopy*, 2011:1–8, 2011. → pages 23
- [89] A. Macnab, B. Friedman, B. Shadgan, and L. Stothers. Bladder anatomy physiology and pathophysiology: Elements that suit near infrared spectroscopic evaluation of voiding dysfunction. *Biomedical Spectroscopy and Imaging*, 1(3):223–235, 2012. → pages 23
- [90] M. Yurt, E. Süer, O. Gülpinar, O. Telli, and N. Arıkan. Diagnosis of bladder outlet obstruction in men with lower urinary tract symptoms: comparison of near infrared spectroscopy algorithm and pressure flow study in a prospective study. *Urology*, 80(1):182–186, July 2012. → pages 24
- [91] A. Amelink, D. J. Kok, H. J. C. M. Sterenborg, and J. R. Scheepe. In vivo measurement of bladder wall oxygen saturation using optical spectroscopy. *Journal of biophotonics*, 4(10):715–720, October 2011. → pages 24

BIBLIOGRAPHY

- [92] G. Vijaya, G. A. Digesu, A. Derpapas, D. C. Panayi, R. Fernando, and V. Khullar. Changes in detrusor muscle oxygenation during detrusor overactivity contractions. *European journal of obstetrics, gynecology, and reproductive biology*, 163(1):104–107, July 2012. → pages 24
- [93] C. H. van der Vaart, J. R. J. de Leeuw, J. P. W. R. Roovers, and A. P. M. Heintz. The effect of urinary incontinence and overactive bladder symptoms on quality of life in young women. *BJU international*, 90(6):544–549, October 2002. → pages 24
- [94] N. K. Kristiansen, J. C. Djurhuus, and H. Nygaard. Design and evaluation of an ultrasound-based bladder volume monitor. *Medical & biological engineering & computing*, 42(6):762–769, November 2004. → pages 25
- [95] S. Leonhardt, A. Cordes, H. Plewa, R. Pikkemaat, I. Soljanik, K. Moehring, H. J. Gerner, and R. Rupp. Electric impedance tomography for monitoring volume and size of the urinary bladder. *Biomedizinische Technik/Biomedical engineering*, 56(6):301–307, December 2011. → pages 25
- [96] K. J. Friston, C. D. Frith, P. F. Liddle, and R. S. Frackowiak. Functional connectivity: the principal-component analysis of large (PET) data sets. *Journal of cerebral blood flow and metabolism*, 13(1):5–14, January 1993. → pages 25
- [97] B. R. White, A. Z. Snyder, A. L. Cohen, S. E. Petersen, M. E. Raichle, B. L. Schlaggar, and J. P. Culver. Resting-state functional connectivity in the human brain revealed with diffuse optical tomography. *NeuroImage*, 47(1):148–156, August 2009. → pages 25, 26, 27, 81
- [98] C. Gerloff, J. Richard, J. Hadley, A. E. Schulman, M. Honda, and M. Hallett. Functional coupling and regional activation of human cortical motor areas during simple, internally paced and externally paced finger movements. *Brain*, 121(8):1513–1531, August 1998. → pages 26
- [99] L. Lee, L. M. Harrison, and A. Mechelli. A report of the functional connectivity workshop, Dusseldorf 2002. *NeuroImage*, 19(2):457–465, June 2003. → pages 26
- [100] A. V. Medvedev, J. M. Kainerstorfer, S. V. Borisov, and J. VanMeter. Functional connectivity in the prefrontal cortex measured by near-infrared spectroscopy during ultrarapid object recognition. *Journal of biomedical optics*, 16(1):016008, 2011. → pages 26

BIBLIOGRAPHY

- [101] B. Biswal, F. Z. Yetkin, V. M. Haughton, and J. S. Hyde. Functional connectivity in the motor cortex of resting human brain using echo-planar MRI. *Magnetic resonance in medicine*, 34(4):537–541, October 1995. → pages 26, 81, 86
- [102] F. T. Sun, L. M. Miller, and M. D’Esposito. Measuring interregional functional connectivity using coherence and partial coherence analyses of fMRI data. *NeuroImage*, 21(2):647–658, February 2004. → pages 26
- [103] S. Schnider, R. Kwong, F. Lenz, and H. Kwan. Detection of feedback in the central nervous system using system identification techniques. *Biological Cybernetics*, 60(3):203–212, January 1989. → pages 26
- [104] L. A. Baccalá and K. Sameshima. Partial directed coherence: a new concept in neural structure determination. *Biological cybernetics*, 84(6):463–474, June 2001. → pages 26
- [105] R. Salvador, A. Martínez, E. Pomarol-Clotet, J. Gomar, F. Vila, S. Sarró, A. Capdevila, and E. Bullmore. A simple view of the brain through a frequency-specific functional connectivity measure. *NeuroImage*, 39(1):279–289, January 2008. → pages 26
- [106] Y. J. Zhang, C. M. Lu, B. B. Biswal, Y. F. Zang, D. L. Peng, and C. Z. Zhu. Detecting resting-state functional connectivity in the language system using functional near-infrared spectroscopy. *Journal of biomedical optics*, 15(4):047003, 2010. → pages 27, 30, 87, 88, 93
- [107] C. M. Lu, Y. J. Zhang, B. B. Biswal, Y. F. Zang, D. L. Peng, and C. Z. Zhu. Use of fNIRS to assess resting state functional connectivity. *Journal of neuroscience methods*, 186(2):242–249, February 2010. → pages 27, 30, 81, 86
- [108] L. Duan, Y. J. Zhang, and C. Z. Zhu. Quantitative comparison of resting-state functional connectivity derived from fNIRS and fMRI: a simultaneous recording study. *NeuroImage*, 60(4):2008–2018, May 2012. → pages 27, 30, 81, 86
- [109] Y. Hada, M. Abo, T. Kaminaga, and M. Mikami. Detection of cerebral blood flow changes during repetitive transcranial magnetic stimulation by recording hemoglobin in the brain cortex, just beneath the stimulation coil, with near-infrared spectroscopy. *NeuroImage*, 32(3):1226–1230, 2006. → pages 28

BIBLIOGRAPHY

- [110] N. Hanaoka, Y. Aoyama, M. Kameyama, M. Fukuda, and M. Mikuni. Deactivation and activation of left frontal lobe during and after low-frequency repetitive transcranial magnetic stimulation over right prefrontal cortex: A near-infrared spectroscopy study. *Neuroscience Letters*, 414(2):99–104, 2007. → pages 28
- [111] H. Mochizuki, T. Furubayashi, R. Hanajima, Y. Terao, Y. Mizuno, S. Okabe, and Y. Ugawa. Hemoglobin concentration changes in the contralateral hemisphere during and after theta burst stimulation of the human sensorimotor cortices. *Experimental Brain Research*, 180(4):667–675, 2007. → pages 28
- [112] H. Mochizuki, Y. Ugawa, Y. Terao, and K. Sakai. Cortical hemoglobin-concentration changes under the coil induced by single-pulse tms in humans: a simultaneous recording with near-infrared spectroscopy. *Experimental Brain Research*, 169(3):302–310, 2006. → pages 29
- [113] G. W. Eschweiler, C. Wegerer, W. Schlotter, C. Spandl, A. Stevens, M. Bartels, and G. Buchkremer. Left prefrontal activation predicts therapeutic effects of repetitive transcranial magnetic stimulation (rtms) in major depression. *Psychiatry Research: Neuroimaging*, 99(3):161–172, 2000. → pages 29
- [114] T.-C. Chiang, T. Vaithianathan, T. Leung, M. Lavidor, V. Walsh, and D. Delpy. Elevated haemoglobin levels in the motor cortex following 1 hz transcranial magnetic stimulation: a preliminary study. *Experimental Brain Research*, 181(4):555–560, 2007. → pages 29
- [115] N. Hanaoka, Y. Aoyama, M. Kameyama, M. Fukuda, and M. Mikuni. Deactivation and activation of left frontal lobe during and after low-frequency repetitive transcranial magnetic stimulation over right prefrontal cortex: a near-infrared spectroscopy study. *Neuroscience letters*, 414(2):99–104, March 2007. → pages 30
- [116] H. Mochizuki, Y. Ugawa, Y. Terao, and K. L. Sakai. Cortical hemoglobin-concentration changes under the coil induced by single-pulse TMS in humans: a simultaneous recording with near-infrared spectroscopy. *Experimental brain research. Experimentelle Hirnforschung. Expérimentation cérébrale*, 169(3):302–10, March 2006. → pages 30
- [117] R. J. Ilmoniemi and D. Kicić. Methodology for combined TMS and EEG. *Brain topography*, 22(4):233–248, January 2010. → pages 30

BIBLIOGRAPHY

- [118] S. Bestmann, C. C. Ruff, F. Blankenburg, N. Weiskopf, J. Driver, and J. C. Rothwell. Mapping causal interregional influences with concurrent TMS-fMRI. *Experimental brain research*, 191(4):383–402, December 2008. → pages 30
- [119] G. Strang and T. Nguyen. *Wavelets and filter banks*. Wellesley-Cambridge Press, Wellesley, MA, 1997. → pages 33
- [120] S. Mallat. A theory for multiresolution signal decomposition: the wavelet representation. *IEEE Transactions on Pattern Analysis and Machine Intelligence*, 11(7):674–693, July 1989. → pages 33
- [121] D. B. Percival and A. T. Walden. *Wavelet methods for time series analysis*. Cambridge University Press, Cambridge ; New York, 2000. → pages 34
- [122] A. Antoniadis, J. Bigot, and T. Sapatinas. Wavelet Estimators in Nonparametric Regression: A Comparative Simulation Study. *Statistical software*, 83(6):1–83, 2001. → pages 34
- [123] H. A. Chipman, E. D. Kolaczyk, and R. E. McCulloch. Adaptive Bayesian Wavelet Shrinkage. *Journal of the American Statistical Association*, 92(440):1413, December 1997. → pages 34
- [124] D. C. Hoaglin, F. Mosteller, and J. W. Tukey. *Understanding robust and exploratory data analysis*. Wiley, NY, 1983. → pages 35
- [125] R. R. Coifman and D. L. Donoho. Translation-invariant de-noising. In *Wavelets and Statistics*, pages 125–150, 1995. → pages 36
- [126] X.-P. Zhang and M. D. Desai. Adaptive denoising based on sure risk. *IEEE Signal Processing Letters*, 5(10):265–267, 1998. → pages 37, 45
- [127] H. Obrig and A. Villringer. Beyond the visible—imaging the human brain with light. *Journal of cerebral blood flow and metabolism*, 23(1):1–18, January 2003. → pages 40
- [128] S. R. Hintz, D. A. Benaron, A. M. Siegel, A. Zourabian, D. K. Stevenson, and D. A. Boas. Bedside functional imaging of the premature infant brain during passive motor activation. *Journal of perinatal medicine*, 29(4):335–343, January 2001. → pages 40
- [129] M. E. Al-Mualla. *Video coding for mobile communications: efficiency, complexity, and resilience*. Academic Press, San Diego, CA, 2002. → pages 41

BIBLIOGRAPHY

- [130] T. T. Georgiou. An Intrinsic Metric for Power Spectral Density Functions. *IEEE Signal Processing Letters*, 14(8):561–563, 2007. → pages 45
- [131] Y. Zhang, D. H. Brooks, M. A. Franceschini, and D. A. Boas. Eigenvector-based spatial filtering for reduction of physiological interference in diffuse optical imaging. *Journal of biomedical optics*, 10(1):11014, 2005. → pages 51
- [132] D. F. Putnam. Composition and concentrative properties of human urine. Technical Report July, National Aeronautics and Space Administration Report CR-1802, Washington DC, 1971. → pages 53
- [133] L. Stothers, B. Shadgan, and A. Macnab. Near-infrared spectroscopy of the detrusor during urodynamics with simultaneous ultrasound measurements of bladder dimensions and position. *Biomedical Spectroscopy and Imaging*, 1(2):137–145, 2012. → pages 54
- [134] J. K. Choi, M. G. Choi, J. M. Kim, and H. M. Bae. Efficient Data Extraction Method for Near-Infrared Spectroscopy (NIRS) Systems With High Spatial and Temporal Resolution. *IEEE Transactions on Biomedical Circuits and Systems*, 7(2):169–177, April 2013. → pages 58
- [135] R. Choe. *Diffuse optical tomography and spectroscopy of breast cancer and fetal brain*. Doctoral dissertation, University of Pennsylvania, 2005. → pages 62
- [136] G. J. Müller and A. Roggan, editors. *Laser-induced Interstitial Thermotherapy*. SPIE Optical Engineering Press, Bellingham, Wash., 1995. → pages 62, 70
- [137] M. C. van Beekvelt, M. S. Borghuis, B. G. van Engelen, R. A. Wevers, and W. N. Colier. Adipose tissue thickness affects in vivo quantitative near-IR spectroscopy in human skeletal muscle. *Clinical science*, 101(1):21–28, July 2001. → pages 68
- [138] M. Wolf, P. Evans, H. U. Bucher, V. Dietz, M. Keel, R. Strebler, and K. von Siebenthal. Measurement of absolute cerebral haemoglobin concentration in adults and neonates. *Advances in experimental medicine and biology*, 428:219–227, January 1997. → pages 69, 113
- [139] M. Wolf, K. von Siebenthal, M. Keel, V. Dietz, O. Baenziger, and H. U. Bucher. Comparison of three methods to measure absolute cerebral hemoglobin concentration in neonates by near-infrared spectrophotometry. *Journal of biomedical optics*, 7(2):221–227, April 2002. → pages 69, 113

BIBLIOGRAPHY

- [140] D. A. Boas. *Diffuse photon probes of structural and dynamical properties of turbid media: Theory and biomedical applications*. Phd dissertation, University of Pennsylvania, 1996. → pages 70
- [141] N. K. Kristiansen, S. Ringgaard, H. Nygaard, and J. C. Djurhuus. MRI assessment of the influence of body position on the shape and position of the urinary bladder. *Scandinavian journal of urology and nephrology*, 38(1):53–61, January 2004. → pages 71
- [142] L. Harrison, W. Penny, and K. Friston. Multivariate autoregressive modeling of fMRI time series. *NeuroImage*, 19(4):1477–1491, 2003. → pages 73
- [143] B. L. P. Cheung, B. A. Riedner, G. Tononi, and B. D. Van Veen. Estimation of cortical connectivity from EEG using state-space models. *IEEE transactions on bio-medical engineering*, 57(9):2122–2134, September 2010. → pages 73
- [144] S. Weisberg. *Applied linear regression*. Wiley, 2005. → pages 73, 74
- [145] M. Kaminski, M. Ding, W. A. Truccolo, and S. L. Bressler. Evaluating causal relations in neural systems: Granger causality, directed transfer function and statistical assessment of significance. *Biological Cybernetics*, 85(2):145–157, August 2001. → pages 75
- [146] G. Dehaene-Lambertz, S. Dehaene, and L. Hertz-Pannier. Functional neuroimaging of speech perception in infants. *Science*, 298(5600):2013–2015, December 2002. → pages 76
- [147] J. P. Szaflarski, S. K. Holland, V. J. Schmithorst, and A. W. Byars. fMRI study of language lateralization in children and adults. *Human brain mapping*, 27(3):202–212, March 2006. → pages 77
- [148] Y. Hoshi. Functional near-infrared spectroscopy: current status and future prospects. *Journal of biomedical optics*, 12(6):062106, 2007. → pages 77, 86
- [149] D. Zhang and M. E. Raichle. Disease and the brain’s dark energy. *Nature reviews. Neurology*, 6(1):15–28, January 2010. → pages 81, 92, 93, 94, 114
- [150] C. F. Beckmann, M. DeLuca, J. T. Devlin, and S. M. Smith. Investigations into resting-state connectivity using independent component analysis. *Philosophical transactions of the Royal Society of London. Series B, Biological sciences*, 360(1457):1001–1013, May 2005. → pages 81

BIBLIOGRAPHY

- [151] V. L. Cherkassky, R. K. Kana, T. A. Keller, and M. A. Just. Functional connectivity in a baseline resting-state network in autism. *Neuroreport*, 17(16):1687–1690, November 2006. → pages 81
- [152] A. Anand, Y. Li, Y. Wang, J. Wu, S. Gao, L. Bukhari, V. P. Mathews, A. Kalnin, and M. J. Lowe. Activity and connectivity of brain mood regulating circuit in depression: a functional magnetic resonance study. *Biological psychiatry*, 57(10):1079–1088, May 2005. → pages 81
- [153] S. J. Li, Z. Li, G. Wu, M. J. Zhang, M. Franczak, and P. G. Antuono. Alzheimer Disease: evaluation of a functional MR imaging index as a marker. *Radiology*, 225(1):253–259, October 2002. → pages 81
- [154] L. Tian, T. Jiang, Y. Wang, Y. Zang, Y. He, M. Liang, M. Sui, Q. Cao, S. Hu, M. Peng, and Y. Zhuo. Altered resting-state functional connectivity patterns of anterior cingulate cortex in adolescents with attention deficit hyperactivity disorder. *Neuroscience letters*, 400(1-2):39–43, May 2006. → pages 81
- [155] P. Tass, M. G. Rosenblum, J. Weule, J. Kurths, a. Pikovsky, J. Volkmann, A. Schnitzler, and H. J. Freund. Detection of n:m Phase Locking from Noisy Data: Application to Magnetoencephalography. *Physical Review Letters*, 81(15):3291–3294, October 1998. → pages 81
- [156] L. May, J. Gervain, M. Carreiras, and J. F. Werker. The specificity of the neural response to language at birth. In *fNIRS Meeting*, London, UK, 2012. → pages 82, 85, 87, 93
- [157] A. V. Oppenheim, R. W. Schaffer, and J. R. Buck. *Discrete-time signal processing*. Prentice Hall, Englewood Cliffs, N.J., 1989. → pages 83, 84
- [158] K. V. Mardia and P. E. Jupp. *Directional Statistics*. John Wiley, Chichester, NY, 2000. → pages 84
- [159] R. T. Canolty, C. F. Cadieu, K. Koepsell, K. Ganguly, R. T. Knight, and J. M. Carmena. Detecting event-related changes of multivariate phase coupling in dynamic brain networks. *Journal of neurophysiology*, 107(7):2020–2031, April 2012. → pages 85
- [160] J. C. Lagarias, J. A. Reeds, M. H. Wright, and P. E. Wright. Convergence Properties of the Nelder–Mead Simplex Method in Low Dimensions. *SIAM Journal on Optimization*, 9(1):112–147, January 1998. → pages 86

BIBLIOGRAPHY

- [161] C. F. Cadieu and K. Koepsell. Phase Coupling Estimation from Multivariate Phase Statistics. *Neural Computation*, 22(12):3107–3126, December 2010. → pages 86
- [162] J. R. Binder, S. J. Swanson, T. A. Hammeke, G. L. Morris, W. M. Mueller, M. Fischer, S. Benbadis, J. Frost, S. M. Rao, and V. M. Haughton. Determination of language dominance using functional MRI: A comparison with the Wada test. *Neurology*, 46(4):978–984, April 1996. → pages 87
- [163] D. Perani, M. C. Saccuman, P. Scifo, A. Anwender, A. Awander, D. Spada, C. Baldoli, A. Poloniato, G. Lohmann, and A. D. Friederici. Neural language networks at birth. *Proceedings of the National Academy of Sciences of the United States of America*, 108(38):16056–16061, September 2011. → pages 92
- [164] M. Mahmoudzadeh, G. Dehaene-Lambertz, M. Fournier, G. Kongolo, S. Goudjil, J. Dubois, R. Grebe, and F. Wallois. Syllabic discrimination in premature human infants prior to complete formation of cortical layers. In *Proceedings of the National Academy of Sciences of the United States of America*, pages 1–6, February 2013. → pages 92
- [165] Q. Zhang, E. N. Brown, and G. E. Strangman. Adaptive filtering for global interference cancellation and real-time recovery of evoked brain activity: a Monte Carlo simulation study. *Journal of biomedical optics*, 12(4):044014, 2010. → pages 93
- [166] P. Fransson, B. Skiöld, S. Horsch, A. Nordell, M. Blennow, H. Lagercrantz, and U. Aden. Resting-state networks in the infant brain. In *Proceedings of the National Academy of Sciences of the United States of America*, volume 104, pages 15531–15536, September 2007. → pages 93
- [167] M. D. Greicius, G. Srivastava, A. L. Reiss, and V. Menon. Default-mode network activity distinguishes Alzheimer’s disease from healthy aging: evidence from functional MRI. *Proceedings of the National Academy of Sciences of the United States of America*, 101(13):4637–4642, March 2004. → pages 93, 94, 114
- [168] B. J. He, A. Z. Snyder, J. L. Vincent, A. Epstein, G. L. Shulman, and M. Corbetta. Breakdown of functional connectivity in frontoparietal networks underlies behavioral deficits in spatial neglect. *Neuron*, 53(6):905–918, March 2007. → pages 93

BIBLIOGRAPHY

- [169] J. M. Masciotti, J. M. Lasker, and A. H. Hielscher. Digital Lock-In Detection for Discriminating Multiple Modulation Frequencies With High Accuracy and Computational Efficiency. *IEEE Transactions on Instrumentation and Measurement*, 57(1):182–189, January 2008. → pages 98, 100
- [170] V. Tuchin. *Tissue optics: light scattering methods and instruments for medical diagnosis*. SPIE Optical Engineering Press, Bellingham, Washington, 2000. → pages 102
- [171] Z. Zhang, B. Sun, H. Gong, L. Zhang, J. Sun, B. Wang, and Q. Luo. A fast neuronal signal-sensitive continuous-wave near-infrared imaging system. *The Review of scientific instruments*, 83(9):094301, September 2012. → pages 102, 106, 113, 115
- [172] T. Muehlemann, D. Haensse, and M. Wolf. Wireless miniaturized in-vivo near infrared imaging. *Optics express*, 16(14):10323–10330, July 2008. → pages 102, 103, 106, 113, 115
- [173] V. Jurcak, D. Tsuzuki, and I. Dan. 10/20, 10/10, and 10/5 Systems Revisited: Their Validity As Relative Head-Surface-Based Positioning Systems. *NeuroImage*, 34(4):1600–1611, February 2007. → pages 103
- [174] T. J. Huppert, S. G. Diamond, M. A. Franceschini, and D. A. Boas. HomER: a review of time-series analysis methods for near-infrared spectroscopy of the brain. *Applied optics*, 48(10):D280–D298, April 2009. → pages 104
- [175] E. Gratton, S. Fantini, M. A. Franceschini, G. Gratton, and M. Fabiani. Measurements of scattering and absorption changes in muscle and brain. *Philosophical transactions of the Royal Society of London. Series B, Biological sciences*, 352(1354):727–735, June 1997. → pages 107
- [176] G. Gratton. Fast optical imaging of human brain function. *Frontiers in Human Neuroscience*, 4(June):1–9, 2010. → pages 107
- [177] C. K. Kim, S. Lee, D. Koh, and B. M. Kim. Development of wireless NIRS system with dynamic removal of motion artifacts. *Biomedical Engineering Letters*, 1(4):254–259, December 2011. → pages 109
- [178] M. C. Stevens. The developmental cognitive neuroscience of functional connectivity. *Brain and Cognition*, 70(1):1–12, June 2009. → pages 114

BIBLIOGRAPHY

- [179] M. L. Pierro, A. Sassaroli, P. R. Bergethon, B. L. Ehrenberg, and S. Fantini. Phase-amplitude investigation of spontaneous low-frequency oscillations of cerebral hemodynamics with near-infrared spectroscopy: a sleep study in human subjects. *NeuroImage*, 63(3):1571–1584, November 2012. → pages 115
- [180] M. Reinhard, E. Wehrle-Wieland, D. Grabiak, M. Roth, B. Guschlbauer, J. Timmer, C. Weiller, and A. Hetzel. Oscillatory cerebral hemodynamics—the macro- vs. microvascular level. *Journal of the neurological sciences*, 250(1-2):103–9, December 2006. → pages 115
- [181] M. Diop, J. T. Elliott, K. M. Tichauer, T. Y. Lee, and K. St Lawrence. A broadband continuous-wave multichannel near-infrared system for measuring regional cerebral blood flow and oxygen consumption in newborn piglets. *The Review of scientific instruments*, 80(5):054302, May 2009. → pages 115
- [182] L. A. Boyd and C. J. Winstein. Cerebellar stroke impairs temporal but not spatial accuracy during implicit motor learning. *Neurorehabilitation and neural repair*, 18(3):134–143, September 2004. → pages 115
- [183] S. K. Meehan, B. Randhawa, B. Wessel, and L. A. Boyd. Implicit sequence-specific motor learning after subcortical stroke is associated with increased prefrontal brain activations: an fMRI study. *Human brain mapping*, 32(2):290–303, February 2011. → pages 115